Raman Spectroscopy Enhanced by On-Chip Dielectric and Metal Waveguides

Ramanspectroscopie versterkt door geïntegreerde diëlektrische en metalen golfgeleiders

Ali Raza

Promotoren: prof. dr. ir. R. Baets, prof. dr. S. Clemmen
Proefschrift ingediend tot het behalen van de graad van
Doctor in de ingenieurswetenschappen: fotonica

UNIVERSITEIT
GENT

Vakgroep Informatietechnologie
Voorzitter: prof. dr. ir. B. Dhoedt
Faculteit Ingenieurswetenschappen en Architectuur
Academiejaar 2019 - 2020

ISBN 978-94-6355-308-7
NUR 959
Wettelijk depot: D/2019/10.500/116

Universiteit Gent
Faculteit Ingenieurswetenschappen
Vakgroep Informatietechnologie

Ramanspectroscopie versterkt door geïntegreerde diëlektrische en metalen golfgeleiders

Raman spectroscopy enhanced by on-chip dielectric and metal waveguides

---

Ali Raza

Proefschrift ingediend tot het behalen van de graad van
Doctor in de Ingenieurswetenschappen: fotonica
Academiejaar 2019-2020

Universiteit Gent
Faculteit Ingenieurswetenschappen en Architectuur
Vakgroep Informatietechnologie
Photonics Research Group

Promotoren: Prof. Dr. Ir. Roel Baets
Prof. Dr. Ir. Stéphane Clemmen

Jury:		
	Em. Prof. Dr. Ir. Daniël De Zutter (chair)	Ghent University
	Prof. Dr. Ir. Nicolas Le Thomas (secretary)	Ghent University
	Prof. Dr. Ir. Dries Van Thourhout	Ghent University
	Prof. Dr. Jolien Dendooven	Ghent University
	Prof. Dr. Kevin Braeckmans	Ghent University
	Prof. Dr. Seppo Honkanen	Microsoft corporation
	Prof. Dr. Ir. Bjorn Maes	University of Mons
	Prof. Dr. Ir. Pol Van Dorpe	imec, KU Leuven

Universiteit Gent
Faculteit Ingenieurswetenschappen en Architectuur

Vakgroep Informatietechnologie
Technologiepark-Zwijnaarde 126 9052 Gent, België

Tel.: +32-9-331.49.21
Fax.: +32-9-331.48.99

Proefschrift ingediend tot het behalen van de graad van
Doctor in de Ingenieurswetenschappen: fotonica
Academiejaar 2019-2020

Acknowledgement

Behind this doctoral dissertation, there is an immense contribution of many people. First of all, I would like to thanks my supervisor Roel to give me this wonderful opportunity. His continuous support through out my PhD is inimitable. I still remember my first year of PhD, when I was bit lost and had no clear idea which way to proceed. But thanks to Roel for keeping me on a right track. I would also like to thanks my second supervisor Stephane (Mr. Perfectionist). His search for the perfect scientific results has greatly raised the impact of this work. Also, his non-ending questions especially "what if" and "what next" helped me to always look forward and to bring novelty to this work. I am also very grateful to all jury members for their useful comments and interesting questions. Indeed, this has improved the quality of PhD dissertation.

Special thanks to Raman team members (Nina, Kristof, Haolan, Zuyang, Yang and Xiaomin). Our long (sometimes very long) but useful discussions during the Raman meeting, helped me a lot through out this four years journey. I hope you guys enjoy the Raman group meeting as much as I do. I also wish you guys a very good luck in your future research. I also appreciate Nicolas for the fruitful discussion during the Raman meeting. Also, I am very thankful to ex-members of Raman group (Ashim, Frederic and Pieter). It is my pleasure to build my research on the foundation made by all of you during your PhD projects.

I acknowledge the support of all collaborators especially the COCOON group members (Michiel, Jolien and Christophe). Thanks Michiel, for doing plenty of ALD coatings for me. I also appreciate the help of PRG technical staff (Liesbet, Muhammad, Steven, Jasper, Kristien and both Ilse). This work would have not be realized without your support. I also acknowledge the financial support from the funding agency FWO.

Along with the technical support, one always need a friendly working environment. I feel blessed to be a part of PRG. I really appreciate all PRG

group members in this regard to build such a friendly working environment. Thank you, Sooren and Alejandro for all the ”good lucks”. I also like to thanks my office mates, it was pleasure to share an office with you.

I also express my gratitude to my Pakistani friends (Bahawal, Abdul, Shahid, Muneeb, Umar, Adnan, Arslan, Nouman and Kashif). Talking to you guys just make me feel like sitting in my home street with my old college friends. Ofcourse, I cannot forget our Pakistani meal parties.

In the end, I would like to thanks my family back home (Ama, Abu G, Ana, Neelo, Sharay, Nooraa, Fawa , Kashmala, Bheemo and Guriya). Indeed, this all could have not been achieved without your prayers and good wishes.

Helsinki, 20^{th}November 2019
Ali Raza

Table of Contents

List of Figures

List of Tables

List of Acronyms

A

ALD	Atomic layer deposition

C

CCD	Charge coupled devices
CHCF	Cylindrical hollow core fiber
CMOS	Complementary metal oxide semiconductor

E

EM	Electromagnetism
EBL	Electron beam lithography

F

FOM	Figure of merit
FEM	Finite element method
FWHM	Full width half maximum
FDTD	Finite-difference time-domain

L

LSP	Localized surface plasmon

M

MMI	Multimode interference

N

NIR	Near infrared wavelength range
NTP	4-thionitrophenol
NWERS	Nanophotonic waveguide enhanced Raman spectroscopy

P

PECVD	Plasma enhanced chemical vapour deposition

Q

QED	Quantum electrodynamics (theory)

S

SERS	Surface enhanced Raman spectroscopy

SPP	Surface plasmon polaritons

T

TE	Transverse electric
TM	Transverse magnetic

Nederlandse samenvatting –Summary in Dutch–

Ramanspectroscopie is een niet-destructieve chemische analysetechniek die gedetailleerde informatie geeft over de chemische structuur, fase en kristallijnheid. De techniek, genoemd naar de Indiase natuurkundige (Sir C.V. Raman), wordt typisch gebruikt om de vibratie van moleculen te bepalen. De lineariteit van het Raman-proces laat een overvloed aan toepassingen toe waarbij een nauwkeurige en gevoelige kwantificering een rol speelt. In de afgelopen 25 jaar hebben de Raman-instrumenten verbluffende vooruitgang geboekt. Echter, omvangrijke en dure Raman-apparaten en zwakke Raman-doorsneden van analieten, heeft het gebruik ervan beperkt tot toepassingen in labo's.

Recentelijk is er een immense vraag geweest naar vuistgrote, draagbare, geminiaturiseerde spectroscopische Raman-systemen die in het veld kunnen worden gebruikt om verschillende analieten te onderscheiden en te kwantificeren. In een conventionele Raman opstelling zijn vier belangrijke componenten: lichtbron, sensor, filter en detector. Silicium fotonica belooft de integratie van een complete Ramanspectroscoop op chip waar de lichtbron, detector, sensor en andere passieve fotonica functionaliteiten allen geïntegreerd kunnen worden in een millimetergrote chip. Eerder in onze groep hebben Dhakal et al. voor het eerst nanofotonische golfgeleiderspectroscopie (NWERS) gedemonstreerd met behulp van een single mode PECVD siliciumnitride golfgeleider. In NWERS, worden moleculen geëxciteerd door een in de ruimte sterk beperkte golfgeleidermode en het resulterend verstrooid signaal wordt terug in dezelfde golfgeleider verzameld. Onlangs zijn vele andere fotonische platforms, zoals titania en tantla, gebruikt voor een efficiënte NWERS.

Daarom is het noodzakelijk om deze verschillende fotonische platformen op de chip te benchmarken. In dit werk wordt de vergelijking genaakt tussen Al_2O_3, Si_3N_4, Ta_2O_5 en TiO_2 golfgeleiders. De belangrijkste parameters die de waarde van een NWERS-sensor bepalen zijn onder

andere de mogelijkheid om het Raman-signaal van een analiet te verzamelen, d.w.z. "de Raman-omzettingsrendementenën de hoeveelheid "Raman-achtergrond"die wordt gegenereerd door het begeleidend materiaal. De resultaten tonen aan dat TiO_2 golfgeleiders een hoge Raman conversie efficiënte vertonen. De signaal-achtergrondverhouding neemt echter af door de hogere Raman-achtergrond. Aan de andere kant vertonen Al_2O_3 golfgeleiders een zwakke Raman-achtergrond, maar de signaalverzamelingsefficintie lijdt onder het lage indexcontrast. Si_3N_4 en Ta_2O_5 golfgeleiders lijken bijna even goede platformen te zijn voor Ramanspectroscopie gezien hun Raman-achtergrond vrij laag zijn, maar hun vermogen om het Raman-signaal van de analiet te verzamelen sterk is.

NWERS geniet een breed scala aan toepassingen voor analieten van vloeibare tot gasvormige toestanden. Echter, analieten zoals monolagen vereisen verdere signaalverbetering. Bovendien vereisen de relatief lage pompvermogens van de beschikbare geïntegreerde lichtbronnen een hoge gevoeligheid van geïntegreerde Raman-sensoren voor bepaalde chemische en biologische toepassingen. Een manier om het Raman-signaal te verbeteren is het gebruik van plasmonische nanostructuren. De mogelijkheid van plasmonica om het licht onder de diffractielimiet te manipuleren maakt het een uitstekend platform voor veel sensortoepassingen. Onlangs is een stap voorwaarts gezet om deze plasmonische structuren te integreren aan de hand van mature fotonica technologieën die uiteindelijk kan leiden tot een goedkope en geminiaturiseerde gentegreerde Raman-sensor. In onze groep demonstreerden Peyskens et al, oppervlakte-versterkte Ramanspectroscopie (SERS) met behulp van plasmonische vlinderdasantennes gentegreerd op een siliciumnitride golfgeleider. In dit proefschrift hebben we het effect van PECVD Si_3N_4 golfgeleider Raman achtergrond op het SERS signaal geanalyseerd. Door het sterke terugverstrooide Stokes-signaal te verzamelen en gebruik te maken van een kleine toegangsgolfgeleiderlengte (het gedeelte voor de plasmonische mode), wordt een gentegreerd SERS met één enkele gentegreerde antenne bereikt.

De nanoantenne op een golfgeleider is gefabriceerd met behulp van e-beam lithografie. Lithografie met elektronenstraal biedt een hoge resolutie, maar de punt per punt blootstelling maakt het proces traag. Daarom belemmert het de massaschaalbaarheid. In het laatste deel van het proefschrift introduceerden we een andere geïntegreerde SERS sensorgeometrie die een hoger SERS-signaal levert dan de nanoantenne en tegelijkertijd kan worden gefabriceerd met behulp van een e-beam-vrije lithografie techniek. De sensor bestaat uit een metalen sleufvormige golfgeleider die gefabriceerd

werd met behulp van ALD geassisteerde DUV lithografie. We hebben zowel experimentele en numerieke karakterisering van onze sensor vermeld, met eigenschappen die tot nu toe moeilijk te combineren waren in een enkele sensor: 1) een grote Raman conversie efficintie, dankzij het gelijktijdig hebben van een lange interactie lengte, hoge veld opsluiting en plasmonische versterking (SMEF = 1.5×10^7), 2) een lage achtergrond als gevolg van de verminderde overlap van het veld met de kern van de golfgeleider 3) een goede reproduceerbaarheid van de Raman spectra (RSD $< 5\%$) over verschillende chips dankzij de nanometer fabricageprecisie van atoomlaagdepositie, 4) een goede tolerantie voor een vrij groot ingangsvermogen door een matige lokale veldversterking en 5) een breedbandige versterking dankzij het gebruik van propagerende, in plaats van gelokaliseerde, plasmons (nanoantennes). Al deze eigenschappen maken dit soort sensoren ideaal voor de toekomstige integratie met lasers, spectrometers, spectrale filters en detectoren, die een volledig gentegreerde Raman-spectrometerchip zal bevatten.

Verder hebben we ook een SERS-sensor gerapporteerd voor Ramanspectroscopie op een chip met behulp van een nieuw ALD-proces voor goud. De vorming van 10 nm brede nanosloten over de hele breedte en lengte van de Si_3N_4 sleufvormige golfgeleiders leidt tot een grote pomp naar Stokes conversie efficiënte. De voorlopige resultaten tonen een grote SERS signaalversterking, maar een verder experimenteel onderzoek is nodig om het volledige potentieel van deze fabricage-vrije plasmonische nanosloten, direct gegroeid op Si_3N_4 sleufvormige golfgeleiders, te analyseren.

Tot slot bespraken we verschillende types van on-chip Ramanspectroscopie, d.w.z. nanofotonische golfgeleider versterkte Ramanspectroscopie, SERS op een chip en metalen golfgeleider versterkte Ramanspectroscopie. Het resultaat suggereert dat de NWERS een betere techniek voor de vloeibare analieten is. Aan de andere kant presteert metalen golfgeleider versterkte Ramanspectroscopie het best voor de monolaag geadsorbeerd aan het oppervlak van de sensor. De voordelen van deze technieken gaat verder dan enkel de prestatie van het apparaat. De integratie met andere fotonische componenten zoals lasers, filters, detectoren enz. zal de weg openen naar geminiaturiseerde, goedkope en efficiënte Raman sensoren. Gezien de compactheid van onze geïntegreerde sensoren, is het gemakkelijk om een chip in je denken die tientallen of honderden sensoren bevat voor het uitvoeren van gemultiplexte Raman-sensoren.

English summary

Raman Spectroscopy is a non-destructive chemical analysis technique which provides detailed information about the chemical structure, phase and crystallinity. The technique named after Indian physicist (Sir C. V. Raman) is typically used to determine vibrational modes of molecules. The linearity of the Raman process, opens a plethora of applications involving precise and sensitive quantification. Over the past 25 years, Raman instruments have undergone stunning advancements. However, the size and high cost of Raman devices have limited its use mainly to in-lab applications.

Recently, there has been an immense demand for hand held and miniaturized spectroscopic Raman systems that can be employed in the field to distinguish and quantify different analytes. In a conventional Raman setup, the four important components are : a light source, sensor, spectral filter and detector. Silicon photonics promises the integration of a complete on chip Raman spectroscope where the light source, detector, sensor and other passive photonics functionalities can be integrated in a millimeter sized chip. Previously in our group, Dhakal et al. for the first time demonstrated nanophotonic waveguide enhanced Raman spectroscopy (NWERS) using a single mode PECVD silicon nitride waveguide. In NWERS, molecules are excited by a confined waveguide mode and resulting scattered signal is collected back in the same waveguide. Recently, many other photonic platforms e.g. titania and tantala, have been employed for efficient NWERS. Therefore, there is a need to benchmark these various on-chip photonic platforms. In this work, a comparison is performed using Al_2O_3, Si_3N_4, Ta_2O_5 and TiO_2 waveguides. The most important parameters defining the figure of merit of an NWERS sensor include its ability to collect the Raman signal from an analyte, i.e. "the Raman conversion efficiency" and the amount of "Raman background" generated from the guiding material. Results show that TiO_2 waveguides exhibit high Raman conversion efficiency. However, the signal-to-background ratio decreases due to the higher Raman background. On the other hand, Al_2O_3 waveguides exhibit weak Raman background, but the signal collection efficiency suffers due to the low in-

dex contrast. Si_3N_4 and Ta_2O_5 waveguides seem to be nearly equally good platforms for Raman spectroscopy as their Raman background is rather low but their capability to collect the Raman signal from the analyte is strong.

NWERS enjoys a wide range of applications for the analytes from liquid to gaseous states. However, the analytes like monolayers demands further signal enhancement. Moreover, relatively low pump powers of available on-chip light sources demand the high sensitivity of on-chip Raman sensors to target certain chemical and biological applications. One way to enhance the Raman signal is by using plasmonic nanostructures. The ability of plasmonics to manipulate the light below the diffraction limit makes it an excellent platform for many sensing applications. Recently, an advance step has been taken to integrate these plasmonic structures with mature photonics technology that can eventually leads to a cheap and miniaturized integrated Raman sensor. In our group, Peyskens et al, demonstrated the surface enhanced Raman spectroscopy (SERS) using plasmonic bowtie antennas integrated on a silicon nitride waveguide. In this thesis, we have analyzed the effect of the PECVD Si_3N_4 waveguide Raman background on the SERS signal. By collecting the strong back-scattered Stokes signal and using small access waveguide length, on-chip SERS using a single integrated antenna is presented.

The nanoantenna on a waveguide was fabricated using e-beam lithography. Electron beam lithography offers high resolution but point to point exposure makes the process slow. Therefore, it hinders mass scalability. In the last section of thesis, we introduced another integrated SERS sensor geometry that provides higher SERS signal as compared to the nanoantenna and at the same time can be fabricated using an e-beam free lithography technique. The sensor consists of a metal slot waveguide that is fabricated using ALD assisted DUV lithography. We have reported both experimental and numerical characterization of our sensor demonstrating capabilities that have so far been difficult to combine in a single sensor: 1) a large Raman conversion efficiency thanks to simultaneous long interaction length, high field confinement and plasmonic enhancement (SMEF = 1.5×10^7), 2) a low background due to the reduced overlap of the field with the core of the waveguide 3) a good reproducibility of the Raman spectra (RSD $< 5\%$) across different chips thanks to the nanometer fabrication accuracy provided by atomic layer deposition, 4) a good tolerance to rather large input power due to a moderate local field enhancement and 5) a broadband enhancement thanks to the use of propagating plasmons rather than localized plasmon (nanoantennae). All these features make this kind of sensor

ideal for its future integration with lasers, spectrometers, spectral filters and detectors that will constitute a fully integrated Raman spectrometer chip.

Furthermore, we have also reported a SERS sensor for an on-chip Raman spectroscopy using a novel ALD process of gold. The formation of 10 nm wide nanotrenches continuously along the width and the length of Si_3N_4 slot waveguide leads to a large pump to Stokes conversion efficiency. The preliminary results show a large SERS signal enhancement, however, a further experimental investigation is needed to analyze the full potential of these fabrication-less plasmonic nanotrenches directly grown on Si_3N_4 slot waveguide.

To conclude, we discussed different modalities of on-chip Raman spectroscopy i.e. nanophotonic waveguide enhanced Raman spectroscopy, SERS on a chip and metal waveguide enhanced Raman spectroscopy. The results suggest that the NWERS is the best technique for the liquid analytes. On the other hand, metal waveguide enhanced Raman spectroscopy performs best for the monolayer adsorbed to the sensor's surface. The asset of these techniques is beyond the performance of the device. The integration with other photonic components i.e. lasers, filters, detectors etc, will open the way towards miniaturized, cheap and efficient Raman sensors. Given the compactness of our on-chip sensors, it is easy to foresee a chip containing dozens or hundreds of sensors for performing multiplexed Raman sensing.

1 Introduction

1.1 Introduction

Raman spectroscopy is a spectroscopic technique based on the inelastic scattering of the monochromatic light beam. The inelastic scattering means that the frequency of photons changes upon interaction with a sample. Depending on the initial state of an atom(analyte), the difference of this energy can be either transferred to the system or the system transfers the energy back to the scattered photon. The theory about the Raman scattering was developed by Adolf Smekal in 1923 [1]. In 1930, C. V. Raman demonstrated the Raman spectroscopy using a mercury arc lamp, a simple prism and a photographic plate [2]. Raman spectroscopy is a widely known technique that finds applications from geophysics, archaeology [3] to the life science [4]. Due to the unique fingerprints of every molecule, Raman spectroscopy is used to distinguish different specimens in a complex chemical environment. Similarly, the linearity of the Raman process opens a plethora of applications involving precise and sensitive quantification. Also, the option to do Raman spectroscopy at NIR region makes it suitable for chemical solutions containing water. In spite of all these advantages, Raman spectroscopy has not been yet employed to its full potential mainly due to the following reasons: 1) extremely weak Raman signal and 2) bulky and expensive optical instrumentation. These two bottlenecks have limited its use mainly to in-lab applications.

Recently, there has been an immense demand for the handheld and miniaturized spectroscopic Raman systems [5] that can be deployed in the field to distinguish and quantify different analytes. Thanks to silicon photonics that promises the integration of a complete on chip Raman spectroscope where the light source, detector, sensor and other passive functionalities like line filters can be integrated in a millimeter size chip. Silicon photonics technology not only offers miniaturization but also reduces the cost of the sensor. Besides all these advancements, low power on-chip sources and less sensitive detectors demand the optimization of sensors geometry. Previously in our group, Dhakal et al [6] for the first time demonstrated the nanophotonic waveguide enhanced Raman spectroscopy (NWERS) using a single mode PECVD silicon nitride waveguide. In 2016, Evans et al [7], reported the use of titania waveguides for enhanced Raman spectroscopy. In this work, a high pump to Stokes conversion efficiency was achieved using high-Q ring resonators. Wang et al [8, 9]. analyzed the total power budget associated with the on-chip Raman spectroscopy using tantalum oxide waveguides. In the presence of these different on-chip Raman substrates, there is a need for a systematic comparison. In this work, a comparison is performed using Al_2O_3, Si_3N_4, Ta_2O_5 and TiO_2 waveguides. The most important parameters defining the figure of merit of an NWERS sensor include its ability to collect the Raman signal from an analyte, i.e. "the Raman conversion efficiency" and the amount of "Raman background" generated from the guiding material. Here, we compare different photonic integrated circuit (PIC) platforms capable of on-chip Raman sensing in terms of the aforementioned parameters. Moreover, we also perform the optimization of strip and slot waveguides of all four materials.

NWERS has shown a wide range of applications for analytes that are in liquid [10] or gaseous states [11]. However, ultra-small volume analytes such as monolayers demand further signal enhancement. One way to enhance the Raman signal is by using plasmonics nanostructures. The ability of plasmonics to manipulate the light at a level below the diffraction limit makes it an excellent platform for many sensing applications. Two different types of enhancement together boost the Raman signal i.e. the chemical enhancement that boosts the molecule's Raman cross section and electromagnetic enhancement that enhances the excitation and scattering efficiency. The plasmonics assisted enhancement phenomena is known as surface enhanced Raman scattering. Recently an advanced step has been taken to integrate these plasmonic structures with mature photonics technology. This co-integration can lead to a cheap and miniaturized integrated Raman sensor. In our group, Peyskens et al demonstrated surface enhanced Raman spectroscopy (SERS) using an array of plasmonic bowtie

antennae integrated on a silicon nitride waveguide [12]. In this work, we have proposed an arch dipole geometry that can enhance the SERS signal. Also, we have analyzed the effect of Raman background originating from PECVD Si_3N_4 waveguide on the SERS signal. By collecting the strong back-scattered Stokes signal and using short access waveguide length, we demonstrate on-chip SERS using a single integrated antenna. Also, we demonstrate SERS using an embedded antenna and compare it with SERS using an evanescently excited nanobowtie. The device is fabricated using two e-beam lithography steps. Electron beam lithography offers high resolution but point to point exposure makes the process slow. Therefore, it hinders the mass scalability. We introduce another integrated SERS sensor geometry that provides higher SERS signal as compared to the nanoantenna and at the same time can be fabricated using an e-beam free lithography technique. The sensor consists of a metal slot waveguide that is fabricated using ALD assisted DUV lithography. We have reported both experimental and numerical characterization of our sensor demonstrating capabilities that have so far been difficult to combine in a single sensor. Given the compactness of our plasmonic sensor, it is easy to foresee a chip capable of containing dozens or hundreds of sensors for performing Raman sensing of multiple analytes, simultaneously.

In the end, we have reported a SERS sensor for an on-chip Raman spectroscopy using a novel ALD process of gold. The formation of 10 nm wide nanotrenches continuously along the width and length of the Si_3N_4 slot waveguide leads to a large pump to Stokes conversion efficiency. The prelimnary results show a large SER signal enhancement, however, a further experimental investigation is needed to analyze the full potential of these fabrication-less plasmonic nanotrenches directly grown on Si_3N_4 slot waveguide. Similarly, reproducibility of SERS signal is also needed to be characterized at the chip to chip as well run to run level.

A brief overview of each chapter is given in next section.

1.2 Outline

In chapter 2, we introduce the vibrational spectroscopy and outline the rationale for spontaneous Raman spectroscopy over IR absorption and fluorescence spectroscopy. Moreover, we discuss that the spontaneous emission rate of dipole can be enhanced using a dielectric or metal structures. In the end, we briefly discuss the rationale of nanophotonic waveguide enhanced Raman spectroscopy (NWERS) over a conventional Raman microscope.

In chapter 3, we present the nanophotonic waveguide enhanced Raman spectroscopy where the dielectric waveguide acts as a Raman sensor. The

analytical formalism to quantify the Stokes to pump conversion efficiency of a waveguide is presented. Next, we compare the performance of four different photonic integration platforms (Al_2O_3, Si_3N_4, Ta_2O_5 and TiO_2) as on-chip Raman spectroscopy substrates. The performance is compared in terms of the pump to Stokes conversion efficiency and the Raman background of the waveguide material. A first comparison is made accounting for the current technological fabrication capability and resulting propagation loss. A more general comparison is made that factors out the loss therefore looking forward at technological improvements. We also present the optimization of strip and slot waveguide for each material. In the end, the Raman performance of ALD layer coated Si_3N_4 slot waveguides is analyzed.

Chapter 4 is an introductory chapter in which we discuss the plasmon physics. The physical mechanisms underlying the field enhancement at the localized plasmon modes are presented.

In chapter 5, we present a novel approach in which nanoplasmonic antennas are integrated on a dielectric waveguide for an efficient on chip Raman sensing. The effect of the Raman background generated by the access waveguide is analyzed. By collecting the back-scattered Stokes signal and small access waveguide length, SERS using a single antenna integrated on dielectric waveguide is presented. In the end, a comparison of two different antenna configurations is made. In the first configuration, a bowtie antenna on top of the waveguide is considered where the antenna is excited and SERS signal is collected evanescently to the waveguide mode. In the second configuration, a bowtie antenna is embedded into the dielectric waveguide, where the antenna is now excited directly using the waveguide mode. The comparison is made in terms of SERS signal strength.

In chapter 6, we have reported a novel SERS sensor suitable for on-chip integrated Raman spectroscopy, fabricated using ALD assisted DUV lithography. We have reported both experimental and numerical characterization of our sensor demonstrating capabilities that have so far been difficult to combine in as single sensor. Furthermore, we have also reported a SERS sensor for an on-chip Raman spectroscopy using a novel ALD process of gold. The formation of 10 nm wide nanotrenches continuously along the width and length of PECVD Si_3N_4 slot waveguide leads to a large pump to Stokes conversion efficiency.

In chapter 7, we conclude the thesis by summarizing all the results obtained during this work and give an outlook that highlights many research directions that came out as the result of this thesis work.

1.3 Publications

1.3.1 Publications in international journal

1. **Ali Raza**, Stephane Clemmen and Roel Baets. ALD gold integrated plasmonics waveguides on silicon nitride photonics platfome. APL Photonics., 2020 (to be published).

2. Haolan Zhao, **Ali Raza**, and Roel Baets. Multiplex Volatile Organic Compound (VOC) Raman Sensing With Nanophotonic Slot Waveguides Functionalized With A Mesoporous Enrichment Layer. Optics Letter., 2020 (to be published).

3. Yang Li, Haolan Zhao, **Ali Raza**, and Roel Baets. Surface-enhanced Raman spectroscopy based on plasmonic slot waveguides with free-space oblique illumination. IEEE J. Quantum Electron., 2019.

4. Nina Turk, **Ali Raza**, Pieter Wuytens, Hans Demol, Michiel Van Daele, Christophe Detavernier, Andre Skirtach, Kris Gevaert and Roel Baets. Comparison of free-space and waveguide-based SERS platforms. Nanomaterials, 9(10):1401, 2019.

5. Michiel Van Daele, Matthew Griffiths, **Ali Raza**, Solano Matthias, Feng Eduardo, Ji-Yu Feng, Ranjith Ramachandran, Stéphane Clemmen, Roel Baets, Séan Barry, Christophe Detavernier and Jolien Dendooven, Plasma-enhanced atomic layer deposition of nanostructured gold near room temperature. ACS Applied Materials & Interfaces, 40(11):37229-37238, 2019.

6. **Ali Raza**, Stéphane Clemmen, Pieter Wuytens, Michiel de Goede, Amy S. K. Tong, Nicolas Le Thomas, Chengyu Liu, Jin Suntivich, Andre G. Skirtach, Sonia M. Garcia Blanco, Daniel J. Blumenthal, James S. Wilkinson, and Roel Baets. High index contrast photonic platforms for on-chip Raman spectroscopy .Opt. Express, 27(16) : 23067 23079, 2019.

7. Javier Losada*, **Ali Raza***, Stéphane Clemmen, Aina Serrano, Amadeu Griol, Roel Baets and Alejandro Martínez. SERS detection via individual bowtie nanoantennas integrated in Si_3 N_4 waveguides. IEEE journal of selected topics in quantum electronics, 25(3):16, 2019 (* equal contribution)

8. **Ali Raza**, Stéphane Clemmen, Pieter Wuytens, Muhammad Muneeb, Michiel Van Daele, Jolien Dendooven, Christophe Detavernier, An-

dre Skirtach, and Roel Baets. ALD assisted nanoplasmonic slot waveguide for on-chip enhanced Raman spectroscopy. APL Photonics, 3(11): 116105, 2018.

9. Frédéric Peyskens, Pieter Wuytens, **Ali Raza**, Pol Van Dorpe, and Roel Baets. Waveguide excitation and collection of surface enhanced Raman scattering from a single plasmonic antenna. Nanophotonics,7(7):12991306, 2018.

10. Nicolas Le Thomas, Ashim Dhakal, **Ali Raza**, Frédéric Peyskens, andRoel Baets. Impact of fundamental thermodynamic fluctuations onlight propagating in photonic waveguides made of amorphous materials. Optica, 5(4):328336, 2018.

11. Haolan Zhao, Stéphane Clemmen, **Ali Raza**, and Roel Baets. Stimulated Raman spectroscopy of analytes evanescently probed by a silicon nitride photonic integrated waveguide. Optics letters,43(6):1403 - 1406, 2018.

12. Abdul Rahim, Eva Ryckeboer, Ananth Z Subramanian, Stéphane Clemmen, Bart Kuyken, Ashim Dhakal, **Ali Raza**, Artur Hermans, Muhammad Muneeb, Sooren Dhoore, et al. Expanding the silicon-photonics portfolio with silicon nitride photonic integrated circuits. Journal of lightwave technology, 35(4):639649, 2017.

13. Ashim Dhakal, Pieter Wuytens, **Ali Raza**, Nicolas Le Thomas, and Roel Baets. Silicon nitride background in nanophotonic waveguide enhanced Raman spectroscopy. Materials, 10(2):140, 2017

14. Ashim Dhakal, Frédéric Peyskens, Stéphane Clemmen, **Ali Raza**, Pieter Wuytens, Haolan Zhao, Nicolas Le Thomas, and Roel Baets. Single mode waveguide platform for spontaneous and surface enhanced on-chip Raman spectroscopy. Interface focus, 6(4): 20160015, 2016.

15. Ashim Dhakal, **Ali Raza**, Frédéric Peyskens, Ananth Z. Subramanian, Stéphane Clemmen, Nicolas Le Thomas, and Roel Baets. Efficiency of evanescent excitation and collection of spontaneous Raman scattering near high index contrast channel waveguides. Opt. Express,23(21):27391 27404, Oct 2015.

1.3.2 Publications in international conferences

1. Michiel Van Daele, Matthew B. E. Griffiths, **Ali Raza**, Matthias M. Minjauw, , Sen T. Barry, Roel Baets, Christophe Detavernier, Jolien Dendooven, Near room temperature plasma enhanced atomic layer deposition of gold metal , EuroCVD 22 - Baltic ALD, 2019.

2. Haolan Zhao, **Ali Raza**, Bettina Baumgartner, Stéphane Clemmen, Bernhard Lendl, Andre Skirtach, Roel Baets, Waveguide-Enhanced Raman Spectroscopy Using a Mesoporous Silica Sorbent Layer for Volatile Organic Compound (VOC) Sensing , Conference on Lasers and Electro-Optics, United States, 2019.

3. **Ali Raza**, Stéphane Clemmen, Michiel Van Daele, Jolien Dendooven, Matthew B. E. Griffiths, Sean T. Barry, Andre Skirtach, Christophe Detavernier, Roel Baets, On-chip surface enhanced Raman spectroscopy using ALD grown plasmonic nanotrenches integrated with a silicon nitride slot waveguide , European Conference on Integrated Optics (ECIO 2019), 21, Belgium, pp. paper T.B1.3, 2019.

4. Zuyang Liu, Haolan Zhao, **Ali Raza**, Nicolas. Le Thomas, Roel Baets, On the Performance of Tantalum Pentoxide and Silicon Nitride Slot Waveguides for On-Chip Raman Spectroscopy , European Conference on Integrated Optics, Belgium, 2019.

5. Nina Turk, **Ali Raza**, Pieter. C. Wuytens, H. Demol, Andere Skirtach, K. Gevaert, Roel Baets, Towards SERS-based on-chip detection of protease activity using nanoplasmonic slot waveguides , Proceedings of the 23rd Annual Symposium of the IEEE Photonics Benelux Chapter, Belgium, 2018.

6. **Ali Raza**, Stéphane Clemmen, Michiel. V. Daele, Pieter. C. Wuytens, Jolien. Dendooven, Christophe Detavernier, Roel Baets, The comparison of on-chip SERS substrates: Nanoplasmonic bowtie antenna vs metal slot waveguide , Proceedings of the 23rd Annual Symposium of the IEEE Photonics Benelux Chapter, Belgium, 2018.

7. **Ali Raza**, Stéphane Clemmen, Michiel de Goede, Ali Rizwan, P. Hua, Sonia. M. Garcia-Blanco, Seppo. Honkanen, James. S. Wilkinson, Roel Baets, The performance of High-Index-Contrast Photonics Platforms for On-Chip Raman Spectroscopy , European Conference on Integrated Optics (ECIO, Spain, pp. 35-37, 2018.

8. **Ali Raza**, Javier Losada, Stéphane Clemmen, Roel Baets, Amadeu Griol, Alejandro Martnez, Surface enhanced Raman spectroscopy via isolated plasmonic nanoantennas integrated on silicon nitride waveguides , European Conference on Integrated Optics (ECIO, Spain, pp. 104-106, 2018.

9. Haolan Zhao, Stéphane Clemmen, **Ali Raza**, Roel Baets, Demonstration of Stimulated Raman Scattering on a Silicon Nitride Photonic Integrated Waveguide , Conference on Lasers and Electro-Optics (CLEO), United States, 2018.

10. Nicolas. Le Thomas, **Ali Raza**, Roel Baets, Thermo-refractive noise at high frequency: beyond the conventional model , CLEO 2018, United States, pp. paper SW3L.5, 2018.

11. **Ali Raza**, Michiel. Van Daele, Pieter. C. Wuytens, Jolien Dendooven, Christophe Detavernier, Stéphane Clemmen, Roel Baets, E-beam-lithography free plasmonic slot waveguides for on-chip Raman spectroscopy , CLEO 2018, United States, pp. paper SW3L.6, 2018.

12. Nina Turk, Pieter. C. Wuytens, **Ali Raza**, Andere Skirtach, Roel Baets, Organic Adhesion Layer for an Increased Waveguide-Excited Surface-Enhanced Raman Signal , Frontiers in Optics, United States, pp. paper JW3A.82, 2017.

13. **Ali Raza**, Frédéric Peyskens, Pieter. C. Wuytens, Stéphane Clemmen, Pol. V. Dorpe, Roel Baets, Detection of Surface-enhanced Raman Signals from a single nanoplasmonic antenna integrated on a single mode waveguide , CLEO: Science and Innovations,, United States, pp. paper SM.4D.6, 2017.

14. **Ali Raza**, Pieter. C. Wuytens, Frédéric Peyskens, Stéphane Clemmen, Pol. V. Dorpe, Roel Baets, On-chip Enhanced Raman spectroscopy using metal slot waveguide , European Conference on Integrated Optics (ECIO), 19(T7.4), Netherlands, 2017.

15. Stéphane Clemmen, **Ali Raza**, Ashim Dhakal, Frédéric Peyskens, Ananth Subramanian, Pol. Van Dorpe, P.C. Wuytens, Haolan Zhao, E.M.P. Ryckeboer, S. Severi, Nicholas. Le Thomas, Roel Baets, Spectroscopic sensing with silicon nitride photonic integrated circuits , Photonics West 2017, Proc. SPIE 10106, Integrated Optics: Devices, Materials, and Technologies XXI, United States, pp. 101060T, 2017.

16. **Ali Raza**, Frédéric Peyskens, Stéphane Clemmen, Roel Baets, Towards Single Antenna On-Chip Surface Enhanced Raman Spectroscopy: Arch Dipole Antenna , The 7th International Conference on Metamaterials, Photonic Cyrstals and Plasmonics (META'16), 7, Spain, pp. 1196-1197, 2016.

17. Ashim Dhakal, **Ali Raza**, Pieter. C. Wuytens, Frédéric Peyskens, Andere Skirtach, Roel Baets, Lab-on-a-chip Raman sensors outperforming Raman microscopes , CLEO, United States, pp. paper SM2O.3, 2016.

1.3.3 Publications in national conferences

1. **Ali Raza**, Stéphane Clemmen, Michiel Van Daele, Jolien Dendooven, Christophe Detavernier and Roel Baets. Comparison of on-chip Surface Enhanced Raman Spectroscopy substrates: Nanoplasmonic bowtie antenna vs metal slot waveguide, NB photonics seminar, Belgium, 2018.

2. Pieter. C. Wuytens, **Ali Raza**, Haolan Zhao, Nina Turk, Frédéric Peyskens, Xiaomin Nie, Ashim Dhakal, Eva. M. P. Ryckeboer, Stéphane Clemmen, Nicolas Le Thomas and Roel Baets. On-chip Raman Spectroscopy, FEA Research Syposium 2017, Belgium, 2017.

3. **Ali Raza**, Stéphane Clemmen, and Roel Baets. Enhanced Raman spectroscopy using nanoplasmonic slot waveguides, NB photonics seminar, Belgium, 2016.

References

[1] Adolf Smekal. *Zur quantentheorie der dispersion*. Naturwissenschaften, 11(43):873–875, 1923.

[2] Chandrasekhara Venkata Raman and Kariamanikkam Srinivasa Krishnan. *A new type of secondary radiation*. Nature, 121(3048):501, 1928.

[3] Peter Vandenabeele. *Raman spectroscopy in art and archaeology*. Journal of Raman spectroscopy, 35(8-9):607–609, 2004.

[4] Dustin W Shipp, Faris Sinjab, and Ioan Notingher. *Raman spectroscopy: techniques and applications in the life sciences*. Advances in Optics and Photonics, 9(2):315–428, 2017.

[5] Bryan H Ray and Keith T Carron. *From portable Raman to mobile Raman: the progression of Raman spectroscopy*. In Next-Generation Spectroscopic Technologies XI, volume 10657, page 1065704. International Society for Optics and Photonics, 2018.

[6] Ashim Dhakal, Ananth Z. Subramanian, Pieter Wuytens, Frédéric Peyskens, Nicolas Le Thomas, and Roel Baets. *Evanescent excitation and collection of spontaneous Raman spectra using silicon nitride nanophotonic waveguides*. Opt. Lett., 39(13):4025–4028, Jul 2014.

[7] Christopher C. Evans, Chengyu Liu, and Jin Suntivich. *TiO2 Nanophotonic Sensors for Efficient Integrated Evanescent Raman Spectroscopy*. ACS Photonics, 3(9):1662–1669, 2016.

[8] Nathan F Tyndall, Todd H Stievater, Dmitry A Kozak, Kee Koo, R Andrew McGill, Marcel W Pruessner, William S Rabinovich, and Scott A Holmstrom. *Waveguide-enhanced Raman spectroscopy of trace chemical warfare agent simulants*. Optics letters, 43(19):4803–4806, 2018.

[9] Zilong Wang, Stuart J Pearce, Yung-Chun Lin, Michalis N Zervas, Philip N Bartlett, and James S Wilkinson. *Power budget analysis for waveguide-enhanced Raman spectroscopy*. Applied spectroscopy, 70(8):1384–1391, 2016.

[10] Ashim Dhakal, Ali Raza, Frédéric Peyskens, Ananth Z. Subramanian, Stéphane Clemmen, Nicolas Le Thomas, and Roel Baets. *Efficiency*

of evanescent excitation and collection of spontaneous Raman scattering near high index contrast channel waveguides. Opt. Express, 23(21):27391–27404, Oct 2015.

[11] Scott A. Holmstrom, Todd H. Stievater, Dmitry A. Kozak, Marcel W. Pruessner, Nathan Tyndall, William S. Rabinovich, R. Andrew McGill, and Jacob B. Khurgin. *Trace gas Raman spectroscopy using functionalized waveguides*. Optica, 3(8):891–896, Aug 2016.

[12] Frederic Peyskens, Ashim Dhakal, Pol Van Dorpe, Nicolas Le Thomas, and Roel Baets. *Surface Enhanced Raman Spectroscopy Using a Single Mode Nanophotonic-Plasmonic Platform*. ACS Photonics, 3(1):102–108, 2016.

2

Raman spectroscopy

2.1 Introduction

Spectroscopy is the analysis of the interaction between matter and electromagnetic wave at various frequencies. Spectroscopy looks at how analyte molecules respond to the incident radiation. Emitted and absorbed spectra can be used to gain information about the material. A molecule can be approximated as a dipole oscillating at a specific frequency. When this dipole interacts with the EM radiation, a transition from its initial state to another state occurs. That transition can be a rotational, vibrational or electronic. All these transitions from an initial to final state lead to different kind of spectroscopic techniques i.e fluorescence (due to electronic transitions), rotational spectroscopy (due to transitions between quantized rotational states) and Raman or infrared absorption spectroscopy (due to a transition in vibrational state). In this chapter, we will mainly discuss the vibrational spectroscopy i.e. infrared absorption and Raman spectroscopy where the main emphasis will be given on Raman spectroscopy, which is the major topic of this dissertation. In the end, we will also analyze how Raman scattering can be enhanced when a molecule is exposed to a non-homogeneous medium.

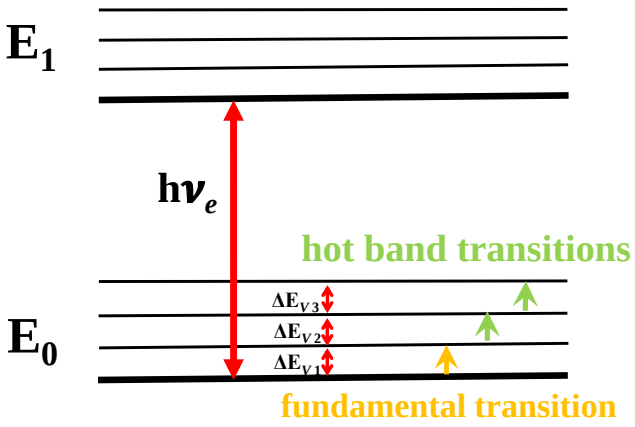

Figure 2.1: The energy diagram of a molecule. The spacing between two electronic states is $\Delta E = h\nu_e$. Each electronic state is split into a band of vibrational states with an energy spacing of ΔE_ν. Depending on the initial energy state, transition can be fundamental or a hot band transition.

2.2 Infrared absorption spectroscopy

A molecule consists of many electronics states just like an atom. But unlike atoms, molecules display many vibrational states. These vibrational states can be approximated by a harmonic oscillators where each vibration state is separated by a fixed energy gap i.e $\Delta E_{\nu 1} = \Delta E_{\nu 2} = \Delta E_{\nu 3} ..... \Delta E_{\nu N} = \hbar\omega$. A quantum mechanical description of such a molecule is shown in Fig. 2.1. The vibrational frequency $f_\nu = \frac{\omega_\nu}{2\pi}$, depends on a specific chemical bond corresponding to a molecule. For the diatomic gases f_ν lies between 10-100 THz. The absorption bands of some trace gases are depicted in Fig. 2.2. When a photon of energy $\hbar\omega$ hits a molecule, it can be absorbed and excites a molecular vibration if its energy matches the transition energy between two different vibrational levels, $\Delta E_{\nu 1}$. In the case of thermal equilibrium at a temperature T, the relative populations of all energy levels is determined by a Boltzmann distribution

$$\frac{N_\nu}{N_0} = exp\left(- \left(\frac{E_\nu - E_0}{kT} \right) \right) \tag{2.1}$$

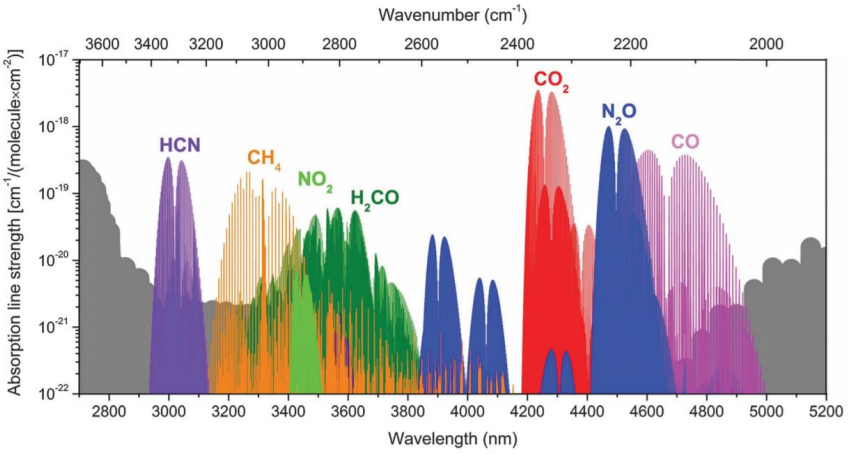

Figure 2.2: Absorption spectra of some important trace gases in the wavelength region between 3 and 5 μm. The solid grey background shows the water vapour absorption. This image is taken from [1].

where N_ν and N_0 are the populations at ν and ground state. As $E_\nu > E_0$ for ν= 1,2,3....., therefore, most of the molecules always reside in the ground state at thermal equilibrium. Hence, $\nu = 0 \rightarrow 1$, transition will dominate an absorption transition. This is called a fundamental transition as shown in Fig. 2.1. Other transitions i.e. $\nu = 1 \rightarrow 2$ or $\nu = 2 \rightarrow 3$, will be possible at higher temperatures but their intensity will be low due to the low population of higher order states. These transitions are termed as hot band transitions.

The absorption frequency is determined by the vibrational mode of the molecule. The strength of the absorption reflects how effectively the energy transfers to a specific vibrational mode. The energy transfer rate depends on the change of the dipole moment of a molecule [2]. The molecule's vibration mode that undergoes a change of dipole moment are known as as IR active while the modes where dipole moment does not change are know as IR inactive. Later we will see that IR inactive modes can still be probed using Raman spectroscopy. A simpler example to understand this phenomena is by assuming a tri-atomic molecule e.g. carbon dioxide CO_2 as shown in Fig. 2.3. CO_2 has four vibrational modes: symmetric C-O stretch, asymmetric C-O stretch and two bending modes along two axis (one is depicted in Fig. 2.3). In the case of symmetric C-O, there is no net change in dipole moment during the complete vibration. Therefore, this is an IR inactive mode. On the other hand, for the bending and asymmetric mode, dipole moment changes as the vibration starts from its zero position. Therefore, these modes are IR active. All the diatomic molecules (AB)

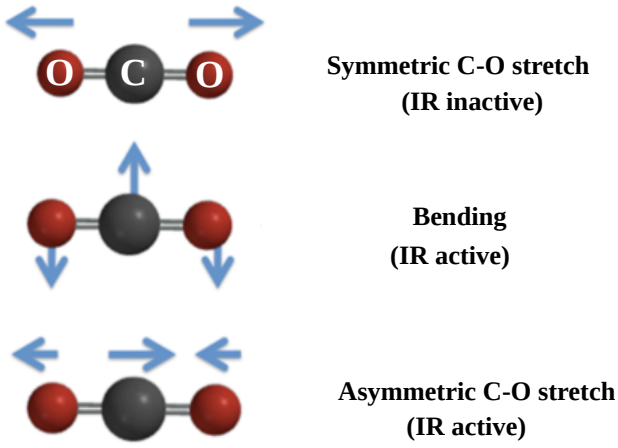

Figure 2.3: Three vibrational modes of carbon dioxide (CO_2). Due to the change in dipole moment, bending and asymmetric C-O stretch is IR active. On the other hand, symmetric stretch is IR inactive.

have an IR active bending mode if the molecular structure is hetero-nuclear i.e. A≠B.

Absorption spectroscopy is a nondestructive technique that biologists and biochemists use to quantify the cellular components and characteristic parameters of functional molecules [3]. Absorption spectroscopy also enjoys a wide range of applications in other disciplines i.e. trace gas sensing [1] and in mineralogical investigations [4]. Also, there exists a wide range of data bases i.e. Spectrabase ($https://spectrabase.com/$) or NIST Chemistry WebBook ($https://webbook.nist.gov/chemistry/$) that provide assistance to researchers working with complex analytes. Despite of large number of applications, there are still some disadvantages that are associated to absorption spectroscopy. Due to the high absorption of water in mid IR and longer wavelength bands, the low concentration analytes contained in aqueous solutions cannot be probed using IR spectroscopy. Also, most relevant fundamental absorption bands are in the mid-IR region, which requires the use of expensive sources and detectors. Also considering an IR spectroscope on a chip requires an on chip broad-band source and low loss waveguide (to mimic a gas-cell). These on chip functionalities are still not up to the mark to meet the requirements of a good IR spectroscope.

As compared to the MID IR region, water has much lower absorption in

the 400-1000 nm wavelength region. Another optical technique that works well in this region is fluorescence spectroscopy in which a molecule undergoes a high energy electronic transition. Fluorophores, i.e. components that cause a molecule to absorb energy of a specific wavelength and then reremit energy at a different but equally specific wavelength, permit sensitive detection of many biological molecules. Fluorescence is a two steps phenomenon: in the first step a high energy photon excites a molecule from a ground electronic state to a high energy electronic state. Then the molecule relaxes to a lower vibrational state of higher electronic state in a time scale of pico-seconds. In the end, the molecule relaxes back to a higher vibrational state of ground electronic state in a time scale of nanosecond steps. Since the first step occurs much faster than the second one, this leads to the non radiative decay [5]. Fluorescence spectroscopy enjoys a range of applications from clinical chemistry [6], DNA sequencing [7] to biomedical imaging [8]. In most of the fluorescence sensing applications, targets (analytes) demand a labelling with a strong external fluorophores [5]. The binding with an external fluorophore changes the chemical properties of the target analyte. Also, fluorophores get photo-bleached that leads to an irreversible change to the absorption and emission properties hence limits the applicability.

Therefore considering all these challenges, it would be interesting to have a technique, unlike IR absorption, that gives a freedom to choose the wavelength of operation and at the same time, unlike fluorescence spectroscopy, does not demand any sample preparation (label free technique). In the next session, we introduce such a technique called "Raman spectroscopy" that is a well established technique in this regard.

2.3 Raman spectroscopy

Raman spectroscopy named after Indian physicist (Sir C. V. Raman) is a spectroscopic technique typically used to determine vibrational modes of molecules. Unlike an IR absorption spectroscopy, in Raman scattering molecule is excited to a virtual state E_{vir} instead of a real vibrational state. The molecule relaxes almost instantaneously to a vibrational level of the electronic ground state. Later on, we will see that the Raman signal is very weak compared to the light coming from fluorescence and therefore we only consider the virtual states with an energy below the first excited electronic state. When considering virtual states above the first electronic level, apart from Raman scattering, fluorescence would occur that acts as a background in the measurements.

A virtual state is an intermediary state in a scattering process and is

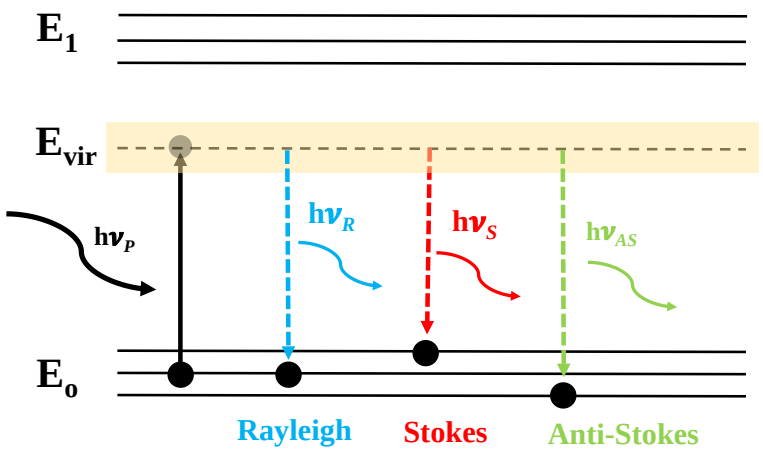

Figure 2.4: The energy diagram of a Raman scattering phenomenon. The molecule is pumped to a virtual state E_{vir} and instantaneously relaxes to one of the vibrational levels of the electronic ground state.

not an eigenstate of the molecule. From the existence of such intermediary states, it follows that the energy of the pump photons does not have to be exactly the same as the transition energy. The relaxation of this virtual state gives rise to the emission of photons with different frequencies depending on the energy levels of the molecule. A transition to such a virtual state has a much lower probability than an infrared transition and that is why Raman cross-sections are small and the signal from Raman scattered light is very weak.

The energy diagram of a Raman scattering phenomenon is shown in Fig. 2.4. When a photon excites the molecule to a virtual state E_{vir}, the molecule relaxes to a vibrational state. In most cases, Rayleigh scattering occurs, which means that the molecule relaxes directly to the initial state of the molecule (which is most often the ground state). This results in the emission of a photon with equal wavelength as the incident photon. In this process, there is no net energy transfer. When inelastic scattering occurs, there is an energy transfer. This inelastic scattering results in scattered light of different wavelengths and is also called the Raman spectrum. As can be seen from figure 2.4, depending on the initial and final state of a molecule, the scattered signal can be blue shifted called anti-Stokes or red shifted also known as Stokes Raman scattering. There is a net transfer of energy to the molecule and from the energy conservation principle, it fol-

lows that the emitted photon has a higher wavelength, (lower energy) than the incident photon. As shown before in Eq. 2.1, at thermal equilibrium, the population of ground state is larger than the excited state therefore, probability of Stokes signal is higher than the anti-Stokes signal. The ratio of the Stokes and anti-Stokes intensities depends on the number of molecules in the ground and excited vibrational states and can be calculated using the Boltzmann distribution : X=exp($\frac{\hbar\omega_\nu}{KT}$). At room temperature and for typical vibrational frequencies ($10 - 100$ THz), X$>>$1. However, sometimes anti-Stokes scattering is preferred in order to mitigate fluorescence background since fluorescence is always red-shifted with respect to the excitation while anti-Stokes emission is at the blue-shifted side.

Contrary to IR absorption spectroscopy, where a change in dipole moment was necessary for a vibration mode to be IR active, Raman active modes are associated to a change in the polarizability. From this classical approximation, we also get an estimation of the Raman signal strength originating from a single molecule. Density functional theory is normally used to simulate the vibration modes of a specific molecular configuration [9].

When a molecule is placed into an oscillating electromagnetic field, the dipole moment can change periodically. This dipole moment change is due to the fact that the incident field is changing the charge distribution. The change of the dipole moment p is linked with the electric field E through a polarizability tensor α i.e.

$$\vec{p} = \alpha\vec{E} \tag{2.2}$$

An oscillating dipole moment radiates electromagnetic waves. The radiating frequency components correspond to the frequency components of the oscillating dipole. From this, it is rather intuitive that when a wave with frequency ω_0 is incident on a dipole moment, the majority of light emitted by the oscillations from the molecules and atoms is at same frequency ω_0. Nevertheless, from the classical analysis (explained in the section below) it can be seen that other frequency components are present. For a plane wave with frequency ω_0, the electric field vector at one place can be described as

$$\vec{E} = \vec{E_0}cos(\omega_0 t) \tag{2.3}$$

The vibration of a molecule can be described by normal coordinates of the atoms of the molecule. Since the ability to perturb the electron distribution depends on the relative position of atoms within the molecule, it is clear that the polarizability is dependent on the normal coordinates. One vibration mode can be described by one normal coordinate. Therefore the analysis is done for one vibration mode. Since the displacement of the nor-

mal coordinate compared to its equilibrium position is relatively small, the polarizability can be approximated by a first order Taylor series [10]

$$\alpha = \alpha_0 + \frac{\partial \alpha}{\partial Q} dQ \tag{2.4}$$

If we assume that the molecule presents a vibrational frequency ω_{vib} and individual atoms are moving in an approximately harmonic way around their equilibrium position. The normal coordinates displacement around the equilibrium can be described as follows.

$$dQ = Q_0 \cos \omega_{vib} t \tag{2.5}$$

Equation 2.5 can be used to rewrite Eq. 2.4 for the polarizability. The oscillating electric field and the periodic change of the polarizability due to the molecular vibrations lead to a new expression for the induced dipole moment. Using a trigonometric identity, this yields

$$\vec{p} = \underbrace{\alpha_0 \vec{E_0} \cos(\omega_0 t)}_{Rayleigh} + \frac{\partial \alpha}{\partial Q_k} \frac{Q_0 \vec{E_0}}{2} \left(\underbrace{\cos((\omega_0 - \omega_{vib})t)}_{Stokes} + \underbrace{\cos((\omega_0 + \omega_{vib})t)}_{Anti-Stokes} \right) \tag{2.6}$$

From this expression of the dipole moment, it is clear that the oscillation of the dipole moment can be seen as a superposition of three dipole moments oscillating at different frequencies. The first dipole is oscillating at the frequency of the incident wave and the light emitted due to this dipole is called Rayleigh scattered light. The next two terms describe dipoles that are not oscillating at the same frequency of the electric field but at frequencies $\omega_0 - \omega_{vib}$ and $\omega_0 + \omega_{vib}$ respectively.

The Raman scattered light consists of Stokes and anti-Stokes light. The radiating dipoles of these terms can be distinguished as noted in the equation above. In the expression, there is a common factor for both 'Raman' dipoles. If this factor is zero, the vibration mode is not Raman active and thus will not lead to any Raman scattered light. The average radiated power by an oscillating electric dipole, induced in a molecule by an electric field of frequency ω_d, is given by

$$P_d = \frac{|p_d|^2 \omega_d^4}{12\pi\epsilon_0 c^3} \tag{2.7}$$

in which p_d can be obtained through equation 2.6. For Stokes and anti-Stokes power, $|p_d|$ can be written as

$$|p_d| = \frac{\partial \alpha}{\partial Q_k} \frac{Q_0 E_0}{2} \tag{2.8}$$

therefore,

$$\frac{\partial \alpha}{\partial Q_k} = 0 \Rightarrow mode_k \text{ is Raman inactive} \tag{2.9}$$

Raman active modes thus have to be modes for which a change in the normal coordinate leads to a change in polarizability. Returning to Fig. 2.3, the IR inactive mode (symmetric C-O stretch of CO_2 molecule) will be a Raman active as the vibration will change the polarizability.

2.3.1 Strength of a Raman scattered signal

Hereafter, we will analyze the strength of a Raman power scattered by a Raman active mode. We will use the formula for the power radiation of a general dipole to estimate the Raman scattering power emitted by a Raman active mode. The scattered Raman intensity I_S can be expressed in the term of the irradiance (J) of an incident field E using,

$$I_s = J\sigma \tag{2.10}$$

where σ is the Raman cross section having unit of m^2per steradian per molecule. σ is a molecular property and its strength resides in the order of 10^{-33} to 10^{-35} m^2per steradian per molecule. The irradiance of an incident field E can be written as J=$\frac{1}{2}c\epsilon_O|E|^2$. The intensity of the scattered radiations equals

$$\begin{aligned} I_s &= \frac{\pi^2 c}{2\epsilon_0 \lambda_d^4} |p_d|^2 \\ &= \frac{\pi^2 c}{2\epsilon_0 \lambda_d^4} \alpha_{tr}^2 |E|^2 \\ &= \frac{\pi^2 c}{2\epsilon_0 \lambda_d^4} \alpha_{tr}^2 \frac{2}{c\epsilon_O} J \\ &= \frac{\pi^2 \alpha_{tr}^2}{\epsilon_0^2 \lambda_d^4} J = \sigma J \end{aligned} \tag{2.11}$$

where α_{tr} is a general transition polarizability and $\sigma = \frac{\pi^2 \alpha^2}{\epsilon_0^2 \lambda_d^4}$ is Raman cross section. The definition of Raman cross section i.e. $\sigma = \frac{\pi^2 \alpha^2}{\epsilon_0^2 \lambda_d^4}$ suggests that in order to enhance the Raman signal, shorter pump wavelength is desirable. However, a great care needs to be taken while choosing the pump

wavelength. Three important properties influence the choice of pump wavelength: 1) Raman cross section, 2) fluorescence background and 3) heat absorption. The pump wavelength of 532 nm provides low heat absorption and high Raman cross section. However, it leads to large florescence background that sometimes masks the weak Raman signal. On the other hand, 1064 nm excitation wavelength provides low florescence background but weakens the Raman signal. On the other hand, a good trade off occurs for 785 nm wavelength. A 785 nm wavelength provides a moderate Raman signal and at the same time does not suffer from the large florescence background. Therefore, red or near infrared region (660−830 nm) are good choice for Raman spectroscopy.

If ϕ is the number of photons scattered per unit of time hitting a detector in a solid angle $d\Omega$ at a wavelength λ_D, then the total scattered intensity I_s is given by

$$I_s = \frac{\phi hc}{\lambda_d d\Omega} \tag{2.12}$$

using Eq. 2.11, the photon rate is the given by

$$\phi = \sigma d\Omega \frac{J\lambda_d}{hc} \tag{2.13}$$

To give some relevant orders of magnitude, let us consider the case of 4-nitrothiophenol NTP molecules (σ=1.8 $\times 10^{-29}$ cm^2/steradian) excited by 10 mW power in the spot size of 1 μm at λ_d = 877 nm, the photon rate will be ϕ = 7.9 $\times 10^{-6}$ photons/sec. So in order to generate one Raman scattered photon, 1.2 $\times 10^5$ molecules are needed. A 10 mW pump power in this case will produce 2.35$\times 10^{-3}$ fW Stokes power. Due to an ultra weak Raman scattering signal, it is desirable to enhance the scattering cross section. In the next section, we will see how the spontaneous emission rate hence Raman scattering of a an oscillating dipole can be enhanced by introducing a perturbation in the surrounding media.

2.3.2 Enhanced spontaneous emission rate

A molecule oscillating in a media on a first instance can be approximated as a dipole emitter. Lets assume a dipole oscillating at a frequency ω in a homogeneous an isotropic medium of index n_i as shown in Fig. 2.5. The spontaneous decay rate of a dipole is given by

$$\gamma_o = \frac{n_i \omega^3 |\mu|^2}{3\pi\epsilon_o \hbar c^3} \tag{2.14}$$

where the factor 3 in the denominator appears due to the averaging over three orthogonal modes. μ is the dipole moment of the oscillating emitter. For the complete derivation of γ_o, readers are suggested to follow [11]. The spontaneous emission rate (and thus the lifetime of the excited level) is determined both by the properties of the emitter and also by the mode structure of the surrounding medium. Also, the refractive index of the surrounding medium perturbs the spontaneous emission rate. In practice, the scattering media (analyte) is rather dense, therefore, the analysis needs to be done on a closely packed cluster of emitters. We will discuss the effect of the surrounding media in more detail in the next section.

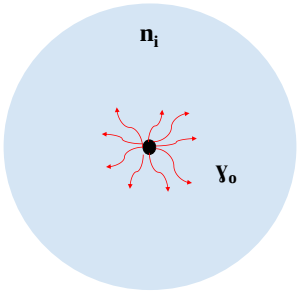

Figure 2.5: Scattering of the dipole oscillating in a homogeneous media of refractive index n_i. γ_o is the spontaneous decay rate.

2.3.2.1 Scattering in an inhomogeneous media

The environment surrounding the emitter can be designed in a way that enhances the spontaneous emission rate γ. This enhancement was first reported by Purcell in 1946 in the magnetic dipoles when subjected to an electronic device [12]. This enhancement phenomena was named as Purcell's enhancement. Later on many demonstrations were reported in different complex environments e.g. dipole near a planar interfaces [13] or an atom in a high Q cavity [14, 15].

For the atom lying in an inhomogeneous media, atom-field interaction is categorized into two distinct regimes based on atom-field coupling constant κ i.e. strong and weak coupling regimes. For a strong coupling regime ($\kappa \gg \gamma$), the interaction between the emitter and the field become dominant over all other decay rates i.e. incoherent field damping in a cavity. Also in the case of multiple emitters system, the interaction between the emitters themselves also becomes important. Therefore, only quantum electrodynamics (QED) can give an accurate description for the strong coupling regime. On the other hand, for the weak coupling regime ($\kappa \ll \gamma$), both

QED and classical theory lead to identical results for the modification of the spontaneous emission decay rate. Classically, one can calculate the γ_c of a dipole emitter oscillating at a frequency ω at a position r, in the weak coupling regime, using Fermi golden rule: [16]

$$\gamma_{\mathbf{c}}(\mathbf{r},\omega) = \frac{\mathbf{2}\pi}{\hbar^{\mathbf{2}}}|\mathbf{\Gamma}(\mathbf{r},\omega)|^{\mathbf{2}}\mathbf{N}(\omega) \tag{2.15}$$

where $\Gamma(\mathbf{r},\omega)$ is the coupling strength between the dipole and the electromagnetic field (E(r,ω), H(r,ω)). N(ω) is the density of the states at an energy level hω. N(ω) is also defined as the number of states per unit volume and energy. $\Gamma(r,\omega)$ is given by

$$|\mathbf{\Gamma}(\mathbf{r},\omega)|^{\mathbf{2}} = \xi^{\mathbf{2}}|\mu.\mathbf{E}(\mathbf{r},\omega)|^{\mathbf{2}} \tag{2.16}$$

where ξ is an energy normalization constant that relates the radiation energy ($\hbar\omega$) with the total electromagnetic energy density $\langle W_{EM}\rangle$ of the waveguide [17]. $\langle W_{EM}\rangle$ for a narrow band signal with a frequency centered around ω can be written as [18]

$$\langle W_{EM}\rangle = \frac{\epsilon_o}{4}\frac{\partial(\omega\epsilon(\mathbf{r},\omega))}{\partial\omega}|\mathbf{E}(\mathbf{r},\omega)|^{\mathbf{2}} + \frac{\mu_{\mathbf{o}}}{\mathbf{4}}|\mathbf{H}(\mathbf{r},\omega)|^{\mathbf{2}} \tag{2.17}$$

where ϵ_o and μ_o are the vacuum permittivity and permeability. By integrating the $\langle W_{EM}\rangle$ over a waveguide dimension, the total energy $\hbar\omega$ carried by a waveguide mode can be computed using

$$\hbar\omega = L\xi^2 \iint \left(\epsilon_o\frac{\partial(\omega\epsilon(\mathbf{r},\omega))}{\partial\omega}|\mathbf{E}(\mathbf{r},\omega)|^{\mathbf{2}} + \mu_{\mathbf{o}}|\mathbf{H}(\mathbf{r},\omega)|^{\mathbf{2}}\right)\mathrm{d}\mathbf{r} \tag{2.18}$$

where the double integral runs over the whole waveguide cross section. L is an arbitrary quantization length that we will use latter to calculate the total density of states (N(ω)). The normalization factor ξ^2 is then given by

$$\xi^2 = \frac{\hbar\omega}{L\iint \left(\epsilon_o\frac{\partial(\omega\epsilon(\mathbf{r},\omega))}{\partial\omega}|\mathbf{E}(\mathbf{r},\omega)|^{\mathbf{2}} + \mu_{\mathbf{o}}|\mathbf{H}(\mathbf{r},\omega)|^{\mathbf{2}}\right)\mathrm{d}\mathbf{r}} \tag{2.19}$$

By putting the Eq.2.15 in Eq.2.16 and Eq.2.19 the modified decay rate $\gamma_c(r,\omega)$ is given as

$$|\gamma_{\mathbf{c}}(\mathbf{r},\omega)|^{\mathbf{2}} = \frac{\mathbf{2}\pi\omega|\mu|^{\mathbf{2}}|\mathbf{E}(\mathbf{r},\omega)|^{\mathbf{2}}\mathbf{N}(\mathbf{r},\omega)}{\hbar\mathbf{L}\iint \left(\epsilon_{\mathbf{o}}\frac{\partial(\omega\epsilon(\mathbf{r},\omega))}{\partial\omega}|\mathbf{E}(\mathbf{r},\omega)|^{\mathbf{2}} + \mu_{\mathbf{o}}|\mathbf{H}(\mathbf{r},\omega)|^{\mathbf{2}}\right)\mathrm{d}\mathbf{r}} \tag{2.20}$$

Eventually, using Eq.2.14, Eq.2.20 and average dipole enhancement approximation [19], the enhanced spontaneous emission rate can be written as

$$\frac{\gamma_{\mathbf{c}}(\mathbf{r},\omega)}{\gamma_{\mathbf{o}}(\mathbf{r},\omega)} = \frac{3c\lambda_o^2}{2n_i^3}\frac{1}{LA_{eff}}N(\mathbf{r},\omega) \tag{2.21}$$

where

$$A_{eff} = \frac{\iint\left(\epsilon_o\frac{\partial(\omega\epsilon(\mathbf{r},\omega))}{\partial\omega}|\mathbf{E}(\mathbf{r},\omega)|^{\mathbf{2}} + \mu_{\mathbf{o}}|\mathbf{H}(\mathbf{r},\omega)|^{\mathbf{2}}\right)\mathrm{d}\mathbf{r}}{\epsilon_o\epsilon(\mathbf{r},\omega)|\mathbf{E}(\mathbf{r},\omega)|^{\mathbf{2}}} \tag{2.22}$$

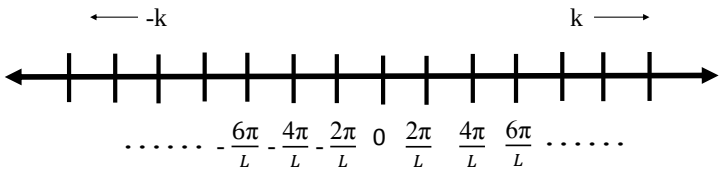

Figure 2.6: The number of modes in a 1-D k space.

Next we will calculate the total density of the states N(r,ω) for a 1-D variant structures i.e. a channel waveguide. The density of the states in a waveguide mode can be computed by counting the number of modes in 1D k space. The numbers of modes in 1-D space are depicted in Fig. 2.6. Analogous to a photon in a waveguide, a particle confined in a quantum well of a length L can be represented as the following wave function $\Psi \propto e^{ikx}$. Owing to high potential barrier, at the boundaries of the quantum well, Ψ must approach to zero that implies

$$k = m\frac{\pi}{L}, \quad m = 1, 2, 3..... \tag{2.23}$$

which shows that in a K-space, various states are equally distributed with a partition length π/L. The line volume for each state is then given by

$$V_k = \frac{\pi}{L} \tag{2.24}$$

Similarly for an infinitesimally small length of dk in range of [k, k+dk], the total density of states are given by

$$N(k)dk = \frac{L}{\pi}dk \tag{2.25}$$

using the photon dispersion relation $E = \hbar\omega(k)$, Eq.2.25 can be converted from k to E space i.e.

$$N(E)dE = N(k)\frac{\partial k}{\partial \omega}d\omega = \frac{L}{\pi}\left(\frac{\partial \omega}{\partial K}\right)^{-1}d\omega \tag{2.26}$$

Eventually, using the group velocity expression $v_g = \partial k/\partial\omega$, the density of the states at a frequency ω can be given as

$$N(\omega) = \frac{L}{\pi v_g} \tag{2.27}$$

Equation.2.27 shows that the lower group velocity leads to higher density of the states thus increases the probability of radiative decay. This leads to an enhanced spontaneous dipole emission [20]. By plugging Eq.2.27 into Eq.2.21, the enhanced radiative decay can be written as

$$\frac{\gamma_{\mathbf{c}}(\mathbf{r},\omega)}{\gamma_{\mathbf{o}}(\mathbf{r},\omega)} = \frac{3}{2\pi}\frac{c}{v_g n_i^3}\frac{\lambda_o^2}{A_{eff}} \tag{2.28}$$

Equation.2.28 is a key result which shows that to enhance the spontaneous emission rate, a structure that supports a waveguide mode of small effective modal area and small group velocity is essential. For the purpose of forthcoming chapters, we will calculate the enhanced spontaneous emission rate of a dipole sitting in three different kind of structures

- Emitter sitting in a dielectric slot waveguide
- Emitter sitting in a gold slot waveguide
- Emitter sitting inside a plasmonic antenna integrated on a dielectric waveguide

The semi-analytical model derived in Eq.2.28 is used to calculate the enhanced spontaneous emission. For a dispersionless medium i.e. $\frac{\partial \epsilon}{\partial \omega} \approx 0$, the effective modal area can be written in a rather simpler form

$$A_{eff} = \frac{\iint \left(2\epsilon_o \epsilon(\mathbf{r},\omega)\mathbf{E}(\mathbf{r},\omega)|^{\mathbf{2}}\right)\mathrm{d}\mathbf{r}}{\epsilon_o \epsilon(\mathbf{r},\omega)|\mathbf{E}(\mathbf{r},\omega)|^{\mathbf{2}}} \tag{2.29}$$

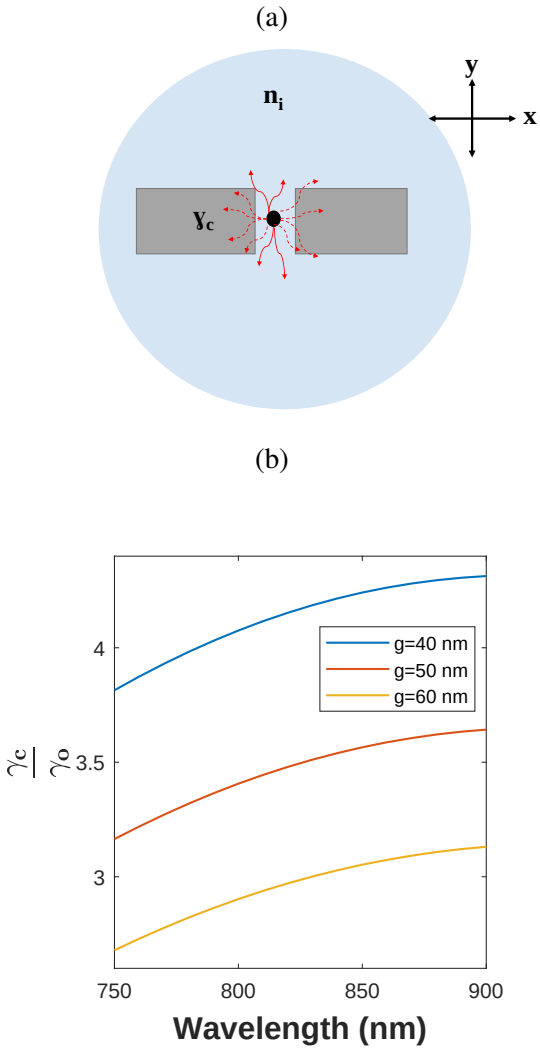

Figure 2.7: a) The schematic of a dipole sitting in a dielectric slot waveguide. γ_c is an enhanced spontaneous emission rate. n_i is the refractive index of surrounding medium. b) The enhanced emission rate of a dipole oscillating in the waveguide of gap width g.

To calculate γ_c, we need to calculate the effective modal area A_{eff} and group velocity v_g of the guided mode. COMSOL finite element mode solver is used to calculate the A_{eff} and v_g. A_{eff} is calculated by assuming a dipole located in the middle of the waveguide slot [17] (represented by black dot in Fig. 2.7.(a). Note that the A_{eff} is slightly different than the A_{eff} used in a QED theory where the dipole is always assumed at a maximum E-field point. In simulations, the refractive index of the dielectric waveguide n_d is assumed as 1.9 (similar to Si_3N_4) [21, 22]. Air is assumed as the surrounding medium i.e. $n_i = 1$. The enhanced spontaneous emission γ_c in the wavelength range from $750-900$ nm is shown in the Fig. 2.7.(b). This wavelength span is chosen as the wavelength of interest. As shown in Fig. 2.7.(b), the normalized γ_c increases with the wavelength. Here not to get confused with the general definition of γ where $\gamma \propto 1/\lambda^4$. Similarly, γ_c also increases by decreasing the waveguide slot gap g. In Chapter 3, we will see that the total pump to Stokes conversion efficiency also increases if width of the slot decreases. That is attributed to high field confinement in the narrow gaps that leads to an efficient excitation and collection of the scattered signal.

An identical analysis is done by replacing the dielectric waveguide with a metal slot waveguide. In COMSOL, a built-in Johnson and Christy refractive index model is used for gold. The structure is depicted in Fig. 2.8.(a). As shown in Fig. 2.8.(b), $\frac{\gamma_c}{\gamma_o}$ is about two orders of magnitude stronger than a dielectric waveguide of a same gap width. This is attributed to the small effective modal area and large group index of the gap plasmonic mode. Similar analysis has been done in [17], where a dipole is assumed inside a silver slot waveguide.

Similarly, $\frac{\gamma_c}{\gamma_o}$ is calculated assuming a dipole plasmonic nanoantenna on a dielectric waveguide of refractive index 1.9. The schematic is depicted in Fig. 2.9.(a). The waveguide height H and width w are set to 220 nm and 700 nm. Air is assumed as the surrounding medium i.e. $n_i = 1$. A fixed antenna gap of 50 nm is assumed. As shown in Fig. 2.9.(b), for each antenna height h, $\frac{\gamma_c}{\gamma_o}$ shows a maximum value at a certain wavelength. This wavelength is called localized surface plasmon wavelength (λ_{LSP}). The hybrid plasmonic mode at λ_{LSP}, shows high field confinement due to the small A_{eff}, therefore, it leads to a large $\frac{\gamma_c}{\gamma_o}$. Figure. 2.9.(b) also shows that λ_{LSP} can be tuned by changing the geometry of a plasmonic nanoantenna. In chapter 4 and 5, we will explain this phenomena in more detail.

In the end, it is worth mentioning that $\frac{\gamma_c}{\gamma_o}$ presented in this section is based on a single dipole oscillating in a inhomogeneous medium. In reality, a cluster of oscillating dipoles needs to be considered. For example, in the case of a liquid analyte on a waveguide, a surface integral needs to be

taken over Eq.2.28. In later chapters, we will define an overall Raman conversion efficiency that not only considers this modal enhancement but also the long light-matter interaction length that is the essence of the waveguide enhanced Raman spectroscopy.

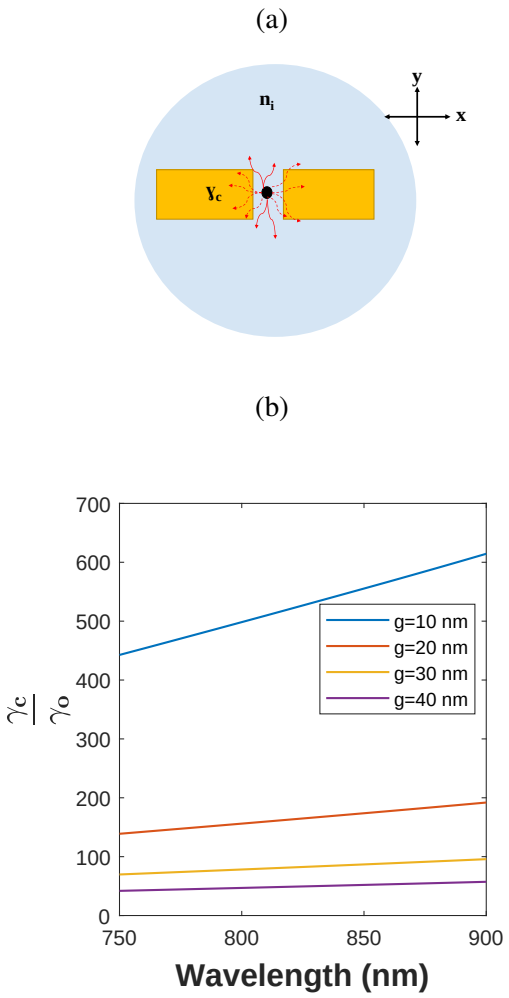

Figure 2.8: a) The schematic of a dipole sitting in a gold slot waveguide. γ_c is an enhanced spontaneous emission rate. n_i is the refractive index of the surrounding medium. b) The enhanced emission rate of a dipole oscillating in the waveguide of gap width g.

(a)

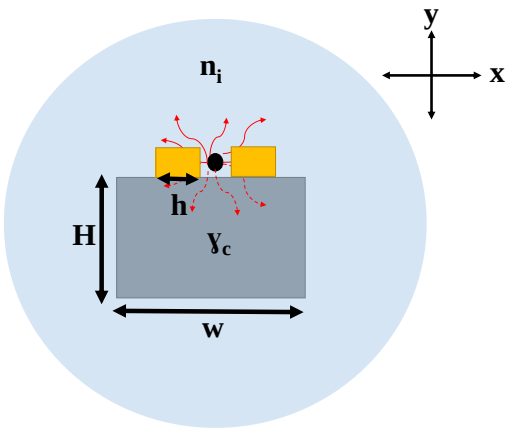

(b)

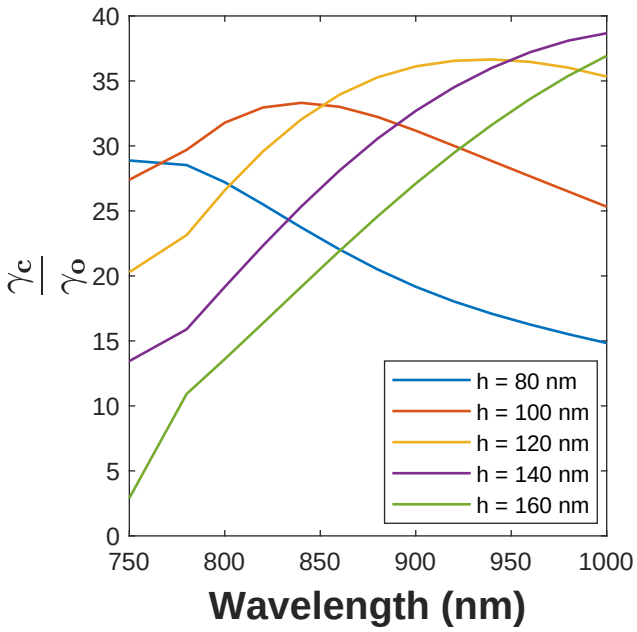

Figure 2.9: a) The schematic of a dipole sitting in a dipole antenna integrated on a dielectric waveguide. γ_c is an enhanced spontaneous emission rate. n_i is the refractive index of the surrounding medium. b) The enhanced emission rate as a functional of wavelength. A fixed gap of 50 nm width is assumed. The maximum value of $\frac{\gamma_c}{\gamma_o}$ changes with changing h of plasmonic antenna.

2.3.3 Pump to stokes conversion efficiency of free conventional Raman microscope

Before we discuss on-chip Raman spectroscopy techniques, it is wise to analyze the performance of a conventional Raman microscope. Pump to Stokes conversion efficiency of a diffraction limited Raman microscope (η_M) is given by [23]

$$\eta_M = \frac{P_S}{P_p} = \Omega \rho \sigma D \tag{2.30}$$

where P_S and P_p are the Stokes and pump power. ρ and σ are the molecular density and Raman cross section, respectively. D is the depth of focus and Ω is the solid angle subtended by the optics. Ω can be expressed in term of numerical aperture NA using

$$\Omega = 2\pi(1 - cos\theta) = 2\pi\left(1 - \sqrt{(1 - (\frac{NA}{n})^2}\right) \approx \pi\left(\frac{NA}{n}\right)^2 \tag{2.31}$$

where n is the refractive index of the immersion medium. D and NA for Gaussian beam can be written as

$$D = \frac{2\pi n \omega^2}{\lambda_e} \tag{2.32}$$

and

$$NA = \frac{\lambda_e}{\pi \omega} \tag{2.33}$$

using Eq. (2.30), (2.31), (2.32) and (2.33), Pump to Stokes conversion efficiency η_M is given by

$$\eta_M = 2\rho\sigma\left(\frac{\lambda_e}{n}\right) \tag{2.34}$$

Equation. 2.34 implies that for a diffraction limited system, pump to Stokes conversion efficiency solely depends on the excitation wavelength and analyte properties i.e. Raman cross section and molecular density. In the next chapter, we will see that for nanophotonic waveguide enhanced spectroscopy, pump to Stokes conversion scales with the length of the waveguide (L_{wg}). This provides many fold enhancement over the conventional Raman microscope i.e. $\eta \propto L_{wg}/\lambda_e >> 1$. [23]

2.4 Conclusion

In this chapter, we introduced the vibrational spectroscopy and outlined the rationale for spontaneous Raman spectroscopy. Moreover, we discussed that the spontaneous emission rate of a dipole can be enhanced using a dielectric or metal structures. Three structures are considered in this regards i.e. a dielectric waveguide, metal slot waveguide and a metal nanoantenna on a dielectric waveguide. In the end, we briefly discussed the rationale of nanophotonic waveguide enhanced Raman spectroscopy over the conventional Raman microscope. In the next chapter, we will present a detailed analysis of nanophotonic waveguide enhanced Raman spectroscopy.

References

[1] Markku Vainio and Lauri Halonen. *Mid-infrared optical parametric oscillators and frequency combs for molecular spectroscopy*. Physical Chemistry Chemical Physics, 18(6):4266–4294, 2016.

[2] Norman Colthup. *Introduction to infrared and Raman spectroscopy*. Elsevier, 2012.

[3] Sanjay M. Nilapwar, Maria Nardelli, Hans V. Westerhoff, and Malkhey Verma. *Absorption Spectroscopy*. In Daniel Jameson, Malkhey Verma, and Hans V. Westerhoff, editors, Methods in Systems Biology, volume 500 of *Methods in Enzymology*, pages 59 – 75. Academic Press, 2011.

[4] Nikita V Chukanov and Alexandr D Chervonnyi. *Infrared spectroscopy of minerals and related compounds*. Springer, 2016.

[5] Joseph R Lakowicz. *Principles of fluorescence spectroscopy*. Springer Science & Business Media, 2013.

[6] TO Tiffany, MB Watsky, CA Burtis, and LH Thacker. *Fluorometric fast analyzer: some applications to fluorescence measurements in clinical chemistry*. Clinical chemistry, 19(8):871–882, 1973.

[7] Lloyd M Smith, Jane Z Sanders, Robert J Kaiser, Peter Hughes, Chris Dodd, Charles R Connell, Cheryl Heiner, Stephen BH Kent, and Leroy E Hood. *Fluorescence detection in automated DNA sequence analysis*. Nature, 321(6071):674, 1986.

[8] Guosong Hong, Alexander L Antaris, and Hongjie Dai. *Near-infrared fluorophores for biomedical imaging*. Nature Biomedical Engineering, 1(1):0010, 2017.

[9] David Chatfield. *Essentials of Computational Chemistry: Theories and Models*. Theoretical Chemistry Accounts, 108(6):367–368, Dec 2002.

[10] D. A. Long. *Classical Theory of Rayleigh and Raman Scattering*. pages 31–48, 2002.

[11] Lukas Novotny and Bert Hecht. *Principles of Nano-Optics*. . Cambridge University Press, page 558, 2006.

[12] Edward Mills Purcell. *Spontaneous Emission Probabilities at Radio Frequencies*. Phys. Rev, 69:681, 1946.

[13] Hans Kuhn. *Classical Aspects of Energy Transfer in Molecular Systems*. The Journal of Chemical Physics, 53(1):101–108, 1970.

[14] P. Goy, J. M. Raimond, M. Gross, and S. Haroche. *Observation of Cavity-Enhanced Single-Atom Spontaneous Emission*. Phys. Rev. Lett., 50:1903–1906, Jun 1983.

[15] Daniel Kleppner. *Inhibited Spontaneous Emission*. Phys. Rev. Lett., 47:233–236, Jul 1981.

[16] Enrico Fermi. *High energy nuclear events*. Progress of theoretical physics, 5(4):570–583, 1950.

[17] Young Chul Jun, Ryan M Briggs, Harry A Atwater, and Mark L Brongersma. *Broadband enhancement of light emission in silicon slot waveguides*. Optics Express, 17(9):7479–7490, 2009.

[18] Jin Au Kong. *Theory of electromagnetic waves*. New York, Wiley-Interscience, 1975. 348 p., 1975.

[19] WL Barnes. *Fluorescence near interfaces: the role of photonic mode density*. journal of modern optics, 45(4):661–699, 1998.

[20] Thang Ba Hoang, Johannes Beetz, Leonardo Midolo, Matthias Skacel, Matthias Lermer, Martin Kamp, Sven Höfling, Laurent Balet, Nicolas Chauvin, and Andrea Fiore. *Enhanced spontaneous emission from quantum dots in short photonic crystal waveguides*. Applied Physics Letters, 100(6):061122, 2012.

[21] Rene M De Ridder, K Warhoff, Alfred Driessen, Paul V Lambeck, and Hans Albers. *Silicon oxynitride planar waveguiding structures for application in optical communication*. IEEE Journal of selected topics in quantum electronics, 4(6):930–937, 1998.

[22] Abdul Rahim, Eva Ryckeboer, Ananth Z Subramanian, Stéphane Clemmen, Bart Kuyken, Ashim Dhakal, Ali Raza, Artur Hermans, Muhammad Muneeb, Sören Dhoore, et al. *Expanding the silicon photonics portfolio with silicon nitride photonic integrated circuits*. Journal of lightwave technology, 35(4):639–649, 2017.

[23] Ashim Dhakal, Pieter Wuytens, Frederic Peyskens, Ananth Subramanian, Andre Skirtach, Nicolas Le Thomas, and Roel Baets. *Nanophotonic Lab-On-A-Chip Raman sensors: a sensitivity comparison with confocal Raman microscope*. In 2015 International Conference on BioPhotonics (BioPhotonics), pages 1–4. IEEE, 2015.

3

Nanophotonic Waveguide enhanced Raman spectroscopy (NWERS)

In the previous chapter we analyzed the enhanced spontaneous emission rate of a dipole when it is subjected to different waveguide structures. In this chapter, we derive an analytical model to access the Raman performance of different dielectric waveguide structures i.e. strip and slots waveguides. We also define a figure of merit (FOM) to analyze different dielectric materials for on-chip Raman spectroscopy. In the end, we analyze the Raman performance of ALD assisted ultra-narrow slot waveguides. We also compare the Raman background of four different ALD materials.

3.1 Introduction to NWERS

Nanophotonic waveguide enhanced Raman spectroscopy (NWERS) is a sensing technique that uses a confined waveguide mode to excite and collect the Raman scattered signal from molecules in a close vicinity of the waveguide. In 1974, Levy et al [1], for the first time, reported the NWERS using micron-sized thin films of methyl-metacrylate coated on a glass substrate. In the past, NWERS was mainly used for mono- and micro-layers [2–6] where free space Raman technique is inefficient due to the minimal modal overlap [7] and the substrate background [8]. All these demonstrations were based on slab-like structures that offer a limited modal overlap and

cannot be integrated with other photonic functionalities. In the last decade, the evolution of better fabrication techniques ensured low loss and compact waveguide structures like strip, slot and sub-wavelength designs. In 2014, Dhakal et al [9], demonstrated NWERS for a bulk analyte using low loss silicon nitride strip waveguides that were integrated with mode transition structures. In 2016, Evans et al [10], reported titania waveguides for an enhanced Raman spectroscopy. In this work, high pump to Stokes conversion efficiency was achieved using a high-Q ring resonator. Same year, Holmstrom et al [11] demonstrated NWERS using an adsorbent layer coated waveguide for the analytes in a vapour phase. An adsorbent layer with a high partition coefficient was used to enhanced the vapour concentration. Recently, NWERS has attracted huge attention for the detection of more complex analytes like DNA [12], haemoglobin [13] that directly binds using surface functionalization recipes. Also, through out these years, there has been an ongoing campaign to improve and understand different performance parameters of NWERS. For example, Dhakal et al. and Kita et al. presented the optimization of dielectric waveguide geometry to enhance the Raman signal [14, 15]. Dhakal et al also discussed the origin of different spectral features of PECVD Si_3N_4 Raman background [16]. Wang et al. analyzed total power budget associated with the on-chip Raman spectroscopy [17, 18]. Similarly, Le Thomas et al, analyzed the origin of Raman background associated with NWERS [19].

As the history of NWERS in Photonics Research Group, Ghent University: Nanophotonic Waveguide enhanced Raman spectroscopy (NWERS) is the core result of Dr. Dhakal's PhD dissertation (graduated, 2016). He established NWERS sensors based on PECVD Si_3N_4 strip and slot waveguides. Different analytes e.g. liquid organic solvents (Isopropyl alcohol) and monolayers (rhodamine, DNA etc) were detected using NWERS sensors.

As a follow up, we have expanded the NWERS scope to other photonic platforms. A benchmarking study comparing four different photonic platforms is presented. We also present the optimization of strip and slot waveguides for an efficient on chip Raman spectroscopy. In the end, an ALD assisted waveguide design is proposed to narrow slot waveguide widths that leads to a mass scalable on-chip sensor.

3.2 Analytical Formalism

In this section, we present an analytical formalism for the pump to Stokes conversion efficiency. We also analyzed the effect of the waveguide loss on the total collected Stokes power. Similarly, we have compared forward and

backward scattered Stokes signal.

3.2.1 Signal conversion efficiency

In the last chapter, we analyzed the enhanced spontaneous emission rate of an emitter sitting in a non-homogeneous media. We now investigate the total conversion efficiency by calculating the total Stokes power generated by the emitting molecules sitting on the top of a waveguide. The normalized decay rate (Eq.2.28) derived in the last chapter also equals to the ratio of the total power coupled to a waveguide mode to the total power radiated in a homogeneous medium

$$\frac{\gamma_{\mathbf{c}}}{\gamma_{\mathbf{o}}} = \frac{P_{wg}}{P_o} \tag{3.1}$$

We assume a dipole is radiating at a frequency $c/\lambda_{\mathbf{s}}$ in a lossless surrounding medium of refractive index n=$\sqrt{\epsilon}$, at position $\mathbf{r_o}$ in a close vicinity of a waveguide of width w and height h. The strength of a dipole d(r,λ_s) excited by a waveguide mode $\mathbf{E}(\mathbf{r}, \lambda_{\mathbf{p}})$ of total guided power P_o can be written as [14, 20]

$$|\mathbf{d}(\mathbf{r}, \lambda_{\mathbf{s}})|^{\mathbf{2}} = \alpha^{\mathbf{2}} \mathbf{n_g} \mathbf{P_o} \frac{\epsilon |\mathbf{E}(\mathbf{r}, \lambda_{\mathbf{p}})|^{\mathbf{2}}}{\iint \epsilon |\mathbf{E}(\mathbf{r}, \lambda_{\mathbf{p}})|^{\mathbf{2}} \mathrm{d}\mathbf{r}} \tag{3.2}$$

where α and n_g are the molecular Raman polarizability and group index of the guided mode, respectively. Let's assume a cluster of closely packed emitters with a molecular density ρ and a scattering cross section σ in an infinitesimal length dL on a waveguide. The cross section of the waveguide is w $\times$ h. The schematic of this configuration is depicted in Fig. 3.1. Using Eq. 3.1, 3.2 and Raman cross section $\sigma = \frac{\pi^2 \alpha^2}{\epsilon_o^2 \lambda^4}$, the total Stokes power dP(λ_s) that couples to a waveguide mode can be written as

$$\frac{dP(\lambda_s)}{P_o} = \rho \times \sigma \times \eta(\mathrm{w}, \mathrm{h}, \lambda_p, \lambda_s) \mathrm{dz} \tag{3.3}$$

where η is the Raman conversion efficiency and is given as

$$\eta(\mathrm{w}, \mathrm{h}, \lambda_p, \lambda_s) = \frac{n_g^2 \lambda_s^2}{n} \iint \frac{\epsilon |\mathbf{E}(\mathbf{r}, \lambda_{\mathbf{p}})|^{\mathbf{2}}}{\iint \epsilon |\mathbf{E}(\mathbf{r}, \lambda_{\mathbf{p}})|^{\mathbf{2}} \mathrm{d}\mathbf{r}} \frac{1}{\mathbf{A_{eff}}(\mathbf{r}, \lambda_{\mathbf{s}})} \mathrm{d}\mathbf{r} \tag{3.4}$$

Equation 3.4 suggests that the η for a given waveguide geometry depends on the modal profile. In Eq. 3.4, the outer integral runs over the area of interest. For example, to estimate the signal strength from an analyte

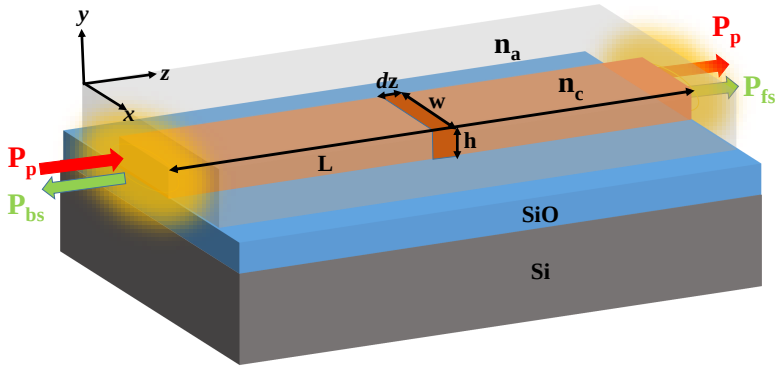

Figure 3.1: The schematic of a HIC waveguide patterned on SiO/Si stack. n_c and n_a are the refractive indices of core and analyte (top cladding) respectively. P_p, P_bs and P_bs represent pump power, back-scattered and forward scattered Stokes signal, respectively.

lying over a waveguide, the integral runs over the top cladding i.e. η=η_A. Likewise, to estimate the waveguide background strength, the integral runs over the waveguide core i.e. η=η_{BG}. Later, we will calculate η_A and η_{BG} for different waveguide geometries and EM polarization.

3.2.2 Length factor: accounting for the waveguide losses

Due to the isotropic nature of the dipole emission, an equal amount of the Stokes signal couples to the waveguide in the backward as well as in forward direction. The surface roughness and material absorption induce a waveguide loss α that results in the decay of the pump as well as the Stokes signal. Consequently, the total collected power on both waveguide ends is different. The evolution of the pump signal inside the waveguide is given as $P_p(z) = P_p(z = 0)e^{-\alpha_p z}$. At every successive point along the waveguide propagation, the Stokes signal is generated. For the forward propagation direction, total Stokes power P_{fs} collected at the output facet is

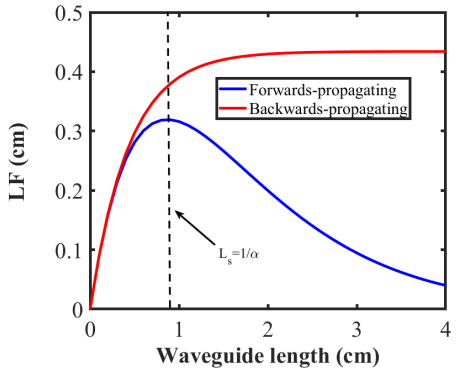

Figure 3.2: The length factor (L.F) comparison for a forward (blue) and a backward (red) propagating Raman signal assuming a fixed waveguide loss of α = 5 dB/cm.

$$\begin{aligned}\frac{P_{fs}}{P(\lambda_p)} &= \frac{1}{2}\times\rho\times\sigma\times\eta_A(\mathrm{w},\mathrm{h},\lambda_p,\lambda_s)\int_0^L e^{-\alpha_p z}e^{-\alpha_s(L-z)}\mathrm{dz}\\ &= \frac{1}{2}\times\rho\times\sigma\times\eta_A(\mathrm{w},\mathrm{h},\lambda_p,\lambda_s)\times\overbrace{e^{-\alpha_p L}\left(\frac{e^{(\alpha_p-\alpha_s)L}-1}{\alpha_p-\alpha_s}\right)}^{\text{Length Factor(LF)}}\end{aligned} \tag{3.5}$$

α_p and α_s are the waveguide losses at pump and Stokes wavelength. For a small difference between α_p and α_s, the term in the brackets approaches to L.

Similarly, for the backward propagating Stokes signal, the total Stokes power P_{bs} collected at the input facet is

$$\begin{aligned}\frac{P_{bs}}{P(\lambda_p)} &= \frac{1}{2}\times\rho\times\sigma\times\eta_A(\mathrm{w},\mathrm{h},\lambda_p,\lambda_s)\int_0^{L_o} e^{-\alpha_s L}e^{-\alpha_p L}\mathrm{dz}\\ &= \frac{1}{2}\times\rho\times\sigma\times\eta_A(\mathrm{w},\mathrm{h},\lambda_p,\lambda_s)\times\overbrace{\left(\frac{1-e^{-(\alpha_p+\alpha_s)L}}{\alpha_\mathrm{p}+\alpha_\mathrm{s}}\right)}^{\text{LF}}\end{aligned} \tag{3.6}$$

The length factor (LF) derived in Eq.3.5 and Eq.3.6 is plotted in Fig. 3.2 for a fixed waveguide loss of α=α_p=α_s = 5 dB/cm. Unlike $\mathrm{LF}_{forward}$, $\mathrm{LF}_{backward}$ saturates after a certain waveguide length L_s=1/α. Also, owing

to the fact that the strongest Raman signal collected soon after the generation, L.F$_{backward}$ is approximately 1.3 times stronger than L.F$_{forward}$. In the latter case, the Raman signal generated at the beginning of the waveguide has to propagate the whole waveguide length before it is collected.

It is worth mentioning that the formalism presented in this section has been used in many previous demonstrations [9, 10]. They have shown that the analytical formula for Stokes to pump conversion efficiency shows remarkably well correspondence with the experimentally obtained results. In the next section, we will use the Raman conversion efficiency to optimized the waveguide design for an efficient NWERS.

3.3 Design optimization of HIC waveguide

The definition of Raman conversion efficiency (Eq. 3.4) suggests that η_A for a given waveguide geometry depends on its modal properties. Therefore, the waveguide design can be engineered to maximize η_A. In this section, the optimization of strip and slot waveguides is presented.

3.3.1 Strip waveguide

Strip and rib structures are the most widely used photonic waveguides mainly due to their low propagation losses, fabrication tolerance and efficient mode coupling. Raman conversion efficiency η_A for a Si_3N_4 strip waveguide is calculated for fundamental TE and TM modes. COMSOL multphysics mode solver is used to compute the waveguide modes. Both TE and TM modes of Si_3N_4 waveguide are shown in Fig. 3.3. The waveguide mode is excited at 785 nm pump wavelength. We use ethanol (n$_a$=1.37) as an analyte at the Raman detuning of the 880 cm^{-1} line. The height of the waveguide is kept constant i.e. h = 220 nm. As shown in Fig. 3.4, η_A for a TM mode is higher than the TE polarized mode. This is due to the higher modal overlap with the analyte. Therefore, strip waveguides with TM polarization mode perform better than TE polarization mode. However, in case of TM mode the characterization of the waveguide Raman background can be challenging due to the considerable modal overlap with the buried oxide (BOX).

Next, we optimize waveguide structures for four different materials materials. Considering the high transparency in the near infrared wavelength region and ability to withstand large optical intensities, four photonic platforms i.e. Alumina (Al_2O_3), Silicon Nitride (Si_3N_4), Tantalum Oxide (Ta_2O_5) and Titania (TiO_2) are investigated. Besides the aforementioned material properties, these photonic platforms also hold the promise

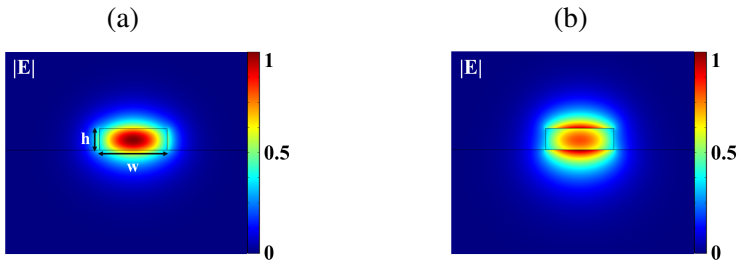

Figure 3.3: TE (a) and TM (b) polarized mode profile (normalized electric field $|E|$) of an ethanol cladded Si_3N_4 strip waveguide. The height and width of the waveguide is 220 nm and 700 nm respectively.

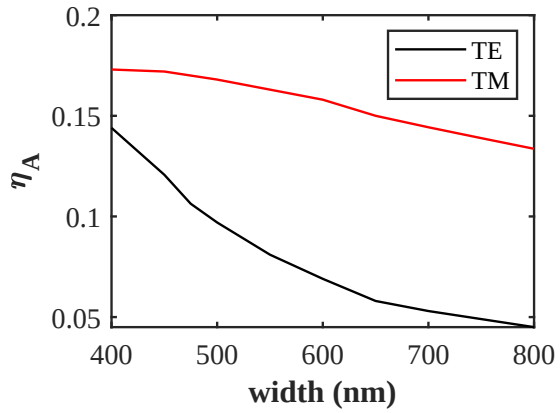

Figure 3.4: The Raman conversion efficiency η at 880 cm^{-1} Stokes shift calculated for Si_3N_4 strip waveguide for TE (black) and TM (red) mode.

of integration of more functionalities such as spectral filtering of the pump beam [21], spectrometers [22, 23], possibly lasers [24, 25] and detectors [26] that can lead to a complete on-chip Raman spectroscope. The optimization is done for different waveguide heights and widths. The range of width and height is chosen in such a way that the waveguide supports only one fundamental TE mode in the wavelength span $785 - 900$ nm. Results are shown in Fig. 3.5. For a fixed height, η increases to a maximum value as the width increases. This corresponds to an optimal confinement in the cladding. Further increase in the width leads to a reduction of η_A. Also, the signal strength is stronger for high aspect ratio waveguide cross sections as

expected from TE excitation. This is due to the higher modal overlap with the analyte. Also, η_A for an optimized geometry improves with increasing refractive index of the core material. It is estimated that the Raman signal strength varies by nearly an order of magnitude between the optimal geometry of an Al_2O_3 waveguide ($\eta_A = 0.039$) and an optimal TiO_2 waveguide ($\eta_A = 0.375$). This is due to an enhanced spontaneous emission of an oscillating dipole and more efficient collection when such a dipole is placed near a high index medium. Also, owing to the stronger optical confinement, the optimal waveguide cross section scales to smaller dimensions for increasing refractive index e.g. $w_o \times h_o$ of Al_2O_3 and TiO_2 are 525 nm $\times$ 1125 nm and 250 nm $\times$ 350 nm respectively.

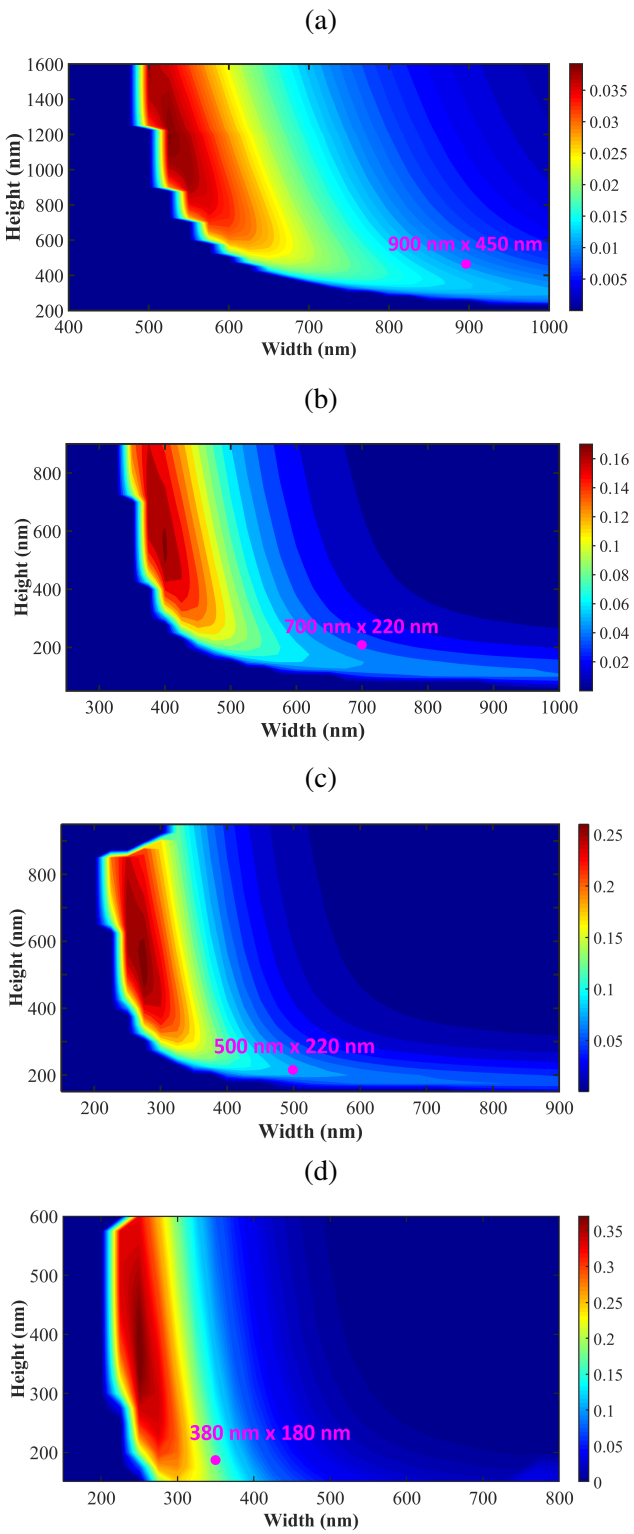

Figure 3.5: The Raman conversion efficiency η_A at 880 cm^{-1} Stokes shift calculated for a) Al_2O_3 (n=1.6), b) Si_3N_4 (n=1.89), c) Ta_2O_5 (n=2.11) and TiO_2 (n=2.33). The circle with magenta face color represents the dimensions of the fabricated waveguides.

3.3.2 Slot waveguides

The gap structures such as the sub-wavelength grating (SWG) [27] and the narrow slot waveguide [28, 29] offer many folds Raman signal enhancement as compared to the strip or rib waveguide [14, 15]. A slot waveguide geometry offers higher Raman conversion efficiency compared to strip waveguides when using TE polarization polarization. The TE and TM polarized mode of a Si_3N_4 at 785 nm wavelength are shown in Fig. 3.6. TE polarization yields the best result because the electric field in the slot is enhanced due to the discontinuity of the refractive index at the interface. This tight confinement of the mode in the slot enhances the light-matter interaction and allows for efficient collection of the generated stokes light. For a fixed gap (g = 150 nm) and height (h = 220 nm), η_A is computed for different waveguide widths. The results are shown in Fig. 3.7. For a TE polarized mode, the light is confined into the gap hence provides a larger modal overlap with the analyte. This leads to a higher η_A as compared to a TM polarized mode.

Next, we have optimized the slot waveguide geometry of silicon nitride (Si_3N_4), tantalum oxide (Ta_2O_5) and titania (TiO_2). As depicted in Fig. 3.8, for a fixed waveguide height (h = 300 nm) and width (w = 500 nm), η_A is computed for different gaps (g). Narrowing the gaps increases the η_A that is attributed to the high field confinement in the waveguide slot [30]. Also, for a fixed gap (g = 40 nm), η_{A,TiO_2} = 1.8 $\times$ η_{A,Ta_2O_5} and η_{A,TiO_2} = 2.5 $\times$ η_{A,Si_3N_4}. Therefore, a HIC waveguide with a higher refractive index (n_c) and a smaller waveguide gap (g) is desirable for the higher Raman conversion efficiency η_A.

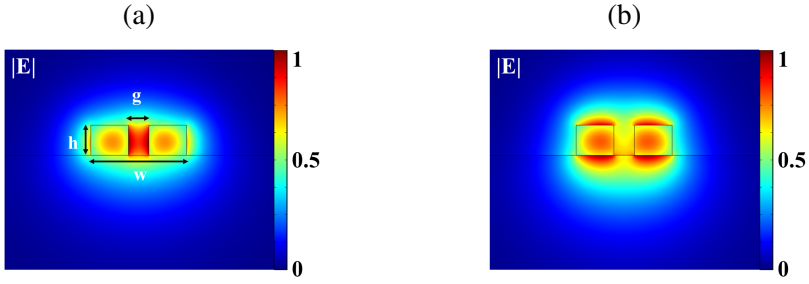

Figure 3.6: TE (a) and TM (b) polarized mode profile (normalized electric field |E|) of an ethanol cladded Si_3N_4 slot waveguide. The height(h), width(w) and gap(g) of the waveguide are 220 nm, 700 nm and 150 nm respectively.

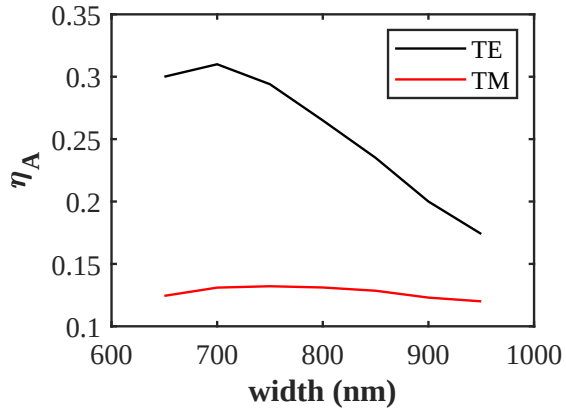

Figure 3.7: The Raman conversion efficiency η_A at 880 cm^{-1} Stokes shift calculated for Si_3N_4 slot waveguide for TE (black) and TM (red) mode.

3.4 Characterization of Raman background and η_o

In this section, we describe the experimental setup that is used to measure the Raman background and Raman conversion efficiency. The Raman background of the four photonic platforms (Al_2O_3, Si_3N_4, Ta_2O_5 and TiO_2) is compared, both in terms of spectral features as well as absolute strength using the same experimental conditions. Next, the signal collection efficiency of each photonic platform is characterized using ethanol as an analyte. Finally, a figure of merit (FOM) for an optimized strip and slot waveguide cross section of all the waveguide materials is established allowing a comparison of the four different platforms for their use as Raman sensor. Most part of the text and the figures used in this section are adapted from [31].

3.4.1 Methods

3.4.1.1 Measurement Setup

The Raman measurements are performed using a confocal Raman microscope (WITEC Alpha300R+). The schematic of the optical setup is shown in Fig. 3.9. The photonic chip is positioned vertically under the high NA objective (0.63 NA, 40 $\times$) i.e., light is coupled in and the Raman signal is collected out of the chip from the same cleaved facet. A Toptica XTRA

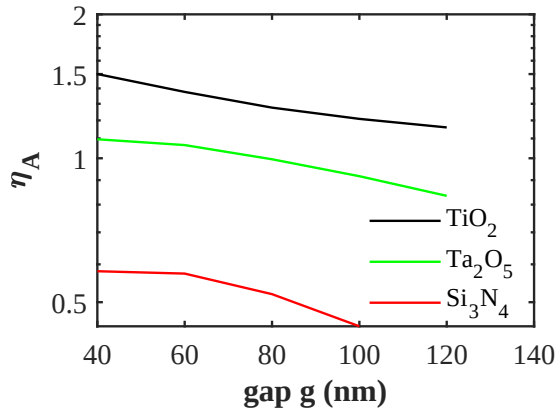

Figure 3.8: The Raman conversion efficiency η_A at 880 cm^{-1} Stokes shift calculated for Si_3N_4, Ta_2O_5 and TiO_2 slot waveguides. η_A is computed for a fixed waveguide height (h = 300 nm) and width (w = 500 nm).

II diode laser pumping at 785 nm wavelength is used and the polarization is set to excite the TE mode of the waveguide. A laser power of 10 mW is measured before the objective. The scattered signal collected in back reflection is imaged on a 100 μm multimode fiber. This fiber functions as confocal pinhole and entrance slit for guiding the Stokes scattered light into the spectrometer, which uses a 600 lines/mm grating to disperse the light onto a -70 ^{o}C cooled CCD camera (ANDOR iDus 401 BR$-$DD). The objective and chip were aligned with a 100 nm precision based on the maximum intensity of the waveguide$'$s Raman spectrum. Simultaneously, maximum light scattering along the waveguide was observed from a camera imaging the top-surface of the chip. All spectra were acquired with a 0.25 sec integration time. At least five waveguides per chip were measured.

3.4.1.2 Fabrication details of Al_2O_3, Si_3N_4, Ta_2O_5 and TiO_2 waveguides

Si_3N_4 strip waveguides used for our experiments are fabricated on a 200 mm silicon wafer containing a stack of $2.3 \pm 0.1\mu$m thick high-density plasma enhanced chemical vapor deposition (PECVD) silicon dioxide SiO_2 and 220 nm thick PECVD Si_3N_4 [32]. The structures were patterned with

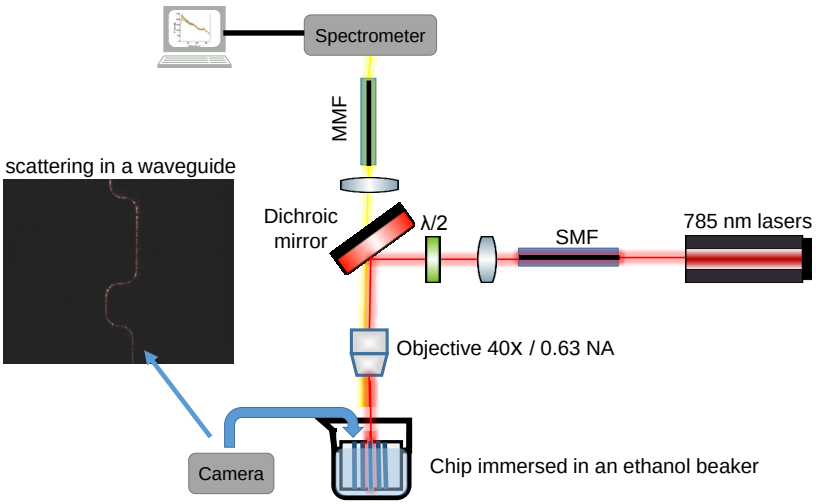

Figure 3.9: The schematic of an optical setup used for Raman measurements. The left inset shows the light scattering of a waveguide imaged by the side camera. SMF = single mode fiber and MMF = mult-imode fiber.

193 nm optical lithography and subsequently etched by fluorine based inductive coupled plasma-reactive ion-etch process to attain the final structure.

Alumina waveguides are patterned at University of Twente, The Netherlands (Group of Dr. Sonia Blanco). For alumina waveguides, a 450 nm thick Al_2O_3 layer was deposited on a thermally oxidized 100-mm Si wafer using an AJA ATC 1500 sputtering system. The UV exposed resist coated samples are inductively coupled plasma (ICP) etched using Oxford Plasma lab 100 (5:2, BCl_3: HBr).

TiO_2 waveguides are fabricated at University of Cornell, USA (Group of Prof. Jin Suntivich). A 180 nm thick TiO_2 film was deposited on a thermal oxidized silicon wafer by reactive sputtering. Next, a bilayer stack of anti-reflective coating and UV$-$210 photoresist were applied on the wafer. Then, the patterns are defined by a deep-ultraviolet stepper (λ =248 nm) and transferred under C_4F_6 plasma etching with He cooling.

Similarly, Ta_2O_5 waveguides are fabricated at University of Southampton, UK (Group of Prof. James Wilkinson). A 220 nm thick film of Ta_2O_5 was deposited onto oxidized silicon wafers using an OIPT Plasmalab 400 RF magnetron sputtering system [33] and annealed in oxygen for 2 hours at 600C. Electron beam lithography (Jeol JBX 9300) followed by argon ion

milling (OIPT Plasmafab 300 Plus) was used to produce strip waveguides of the width ranging from 500 nm to 700 nm.

The geometry and optical properties of the fabricated waveguides are summarized in Table. 3.1. The waveguide length (L) of Si_3N_4 and Ta_2O_5 is 1 cm each. While the waveguide lengths of Al_2O_3 and TiO_2 are 0.9 cm and 0.6 cm respectively.

material	refractive index (n_c)	waveguide geometry (w×h) nm^2	loss, α_m (dB/cm)	η_A	η_{BG}
Al_2O_3	1.60	900 × 450	1.9−2.6	0.013	0.27
Si_3N_4	1.89	700 × 220	2.0−3.1	0.053	0.49
Ta_2O_5	2.11	500 × 220	4.8−5.4	0.13	0.61
TiO_2	2.33	380 × 180	7.0−8.0	0.18	0.79

Table 3.1: The optical properties of the photonic platforms. The η_A (analyte Raman signal conversion efficiency) and η_{BG} (waveguide Raman background conversion efficiency) are computed for 785 nm pump and 843 nm Stokes wavelength.

3.4.2 Characterization of Raman background

Each chip is measured without ethanol to obtain insight in its intrinsic background scattering. All four waveguides have different lengths so that a fair comparison requires to normalize those spectra by their optimal length $LF(L_s)$ and by the coupling efficiency. The coupling efficiencies measured using high NA objective (0.63 NA, 40 ×) to Al_2O_3, Si_3N_4, Ta_2O_5 and TiO_2 waveguides are ≈ 2.9, 3.7, 8.3 and 7.9 dB/facet. The optimized length factor $LF(L_s)$ attributed to each waveguide is depicted in Fig. 3.10. The measured normalized Stokes spectra are shown in Fig. 3.11. The shaded areas represent the standard deviation of 5 different spectra for each waveguide material. This standard deviation is attributed to different coupling efficiencies and waveguide losses of the waveguides on the same chip. The TiO_2 scattering spectrum is scaled down by $1/8$ to plot all spectra in one window. From these measurements, it can be seen that the TiO_2 has by far the strongest background scattering. To validate this strong Raman background of TiO_2 waveguides, Raman spectra of two differently processed TiO_2 are measured and compared. The Raman background of two differently processed TiO_2 chips remarkably align well with each other. These results are shown in Appendix A. PECVD Si_3N_4 and Ta_2O_5 exhibit comparable Raman background, that is approximately 8 times weaker than

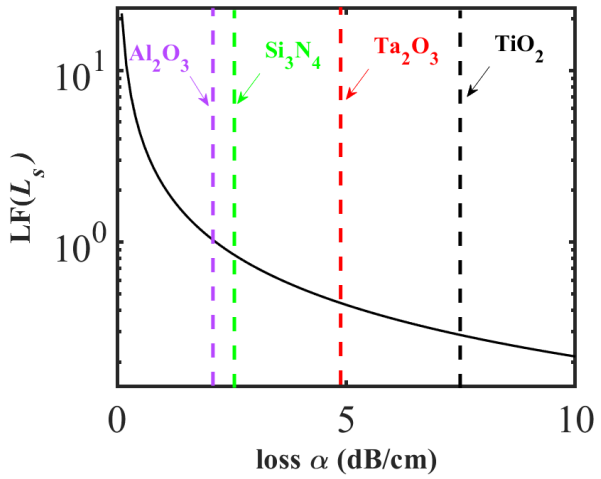

Figure 3.10: The optimized length LF (L_s) for each waveguide structure.

TiO_2. Also, PECVD Si_3N_4, Ta_2O_5 and TiO_2 shows relatively high Raman background in the $0-700$ cm^{-1} range and then much lower background at high Raman shifts. In the Ta_2O_5 Raman background, a major characteristic Raman band at 660 cm^{-1} corresponds to the Ta$-$O stretching vibrations of TaO_6 octahedra [34]. Al_2O_3 shows the weakest Raman background that mostly stays flat along the span of $50 - 1800$ cm^{-1} Raman shift. This characterization also shows that the background strength increases with the refractive index.

In order to discern the fluorescent contribution, each waveguide background is also measured at 633 nm pump wavelength. Due to different modal properties of the waveguide at 633 and 785 nm wavelength, each spectrum is normalized by its maximum counts. The results are shown in Fig. 3.12. Al_2O_3 exhibits slightly different background at higher wavenumbers ($>$1000 cm^{-1}) [35]. No significant change is observed in the spectral features of the Raman background of the other three materials. This confirms no or minimal contribution of auto-florescence to the recorded Raman background.

3.4.3 Characterization of η_A

To characterize the Raman conversion efficiency, the Al_2O_3, Si_3N_4, Ta_2O_5 and TiO_2 chips are immersed into a beaker containing ethanol. Each chip

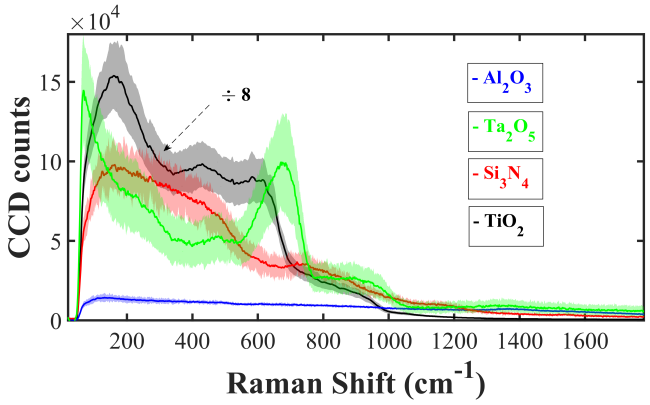

Figure 3.11: The Raman background measured from Al_2O_3, Si_3N_4, Ta_2O_5 *and* TiO_2 *waveguides. All spectra are scaled to its respective optimized length LF (*L_s*). In the* Ta_2O_5 *Raman background, a major characteristic Raman band at 660 cm*$^{-1}$ *corresponds to the Ta−O stretching vibrations of* TaO_6 *octahedra [34].*

is immersed in such a way that few micrometers length of the waveguide is in the air. Each spectrum is recorded after optimizing the strength of the 880 cm^{-1} Raman mode of ethanol. The spectra are shown in Fig. 3.13.a. Each spectrum is normalized by the coupling efficiency and rescaled to its optimal length factor $LF(L_s)$. On top of the strong broad band Raman background of the guiding material, the Raman modes of ethanol are clearly present. The dotted lines represent the 880, 1054, 1098, 1275 and 1456 cm^{-1} Raman vibrations of ethanol. To characterize the relative signal strength, the signal (C_{sig}) and the background (C_{BG}) counts at 880 cm^{-1} are extracted as shown in Fig. 3.13.b (inset). As depicted in Fig. 3.13.b, for the 880 cm^{-1} Raman shift, $C_{sig,SiN}$ / $C_{sig,AlO} \approx 3.63 \pm 0.45$, $C_{sig,TaO}/C_{sig,AlO} \approx 4.84 \pm 0.81$ and $C_{sig,TiO}/C_{sig,AlO} \approx 6.01 \pm 1.6$. This is in good correspondence to what was predicted in Table. 3.1. For example, if ζ_x=$\eta_x \times LF(L_s)_x$ then ζ_{SiN}/ζ_{AlO}=3.44, ζ_{TaO}/ζ_{AlO}=4.15 and ζ_{TiO}/ζ_{AlO}=5.6. It is worth mentioning that the higher index contrast of TiO_2 boosts the Raman signal strength i.e. $\eta_{TiO} \approx 14 \times \eta_{AlO}$. However, the higher waveguide losses, i.e. α_{TiO} = 7−8 dB/cm, negate this overall enhancement.

3.4.4 Figure of merit for an optimized strip waveguide

Knowing the Raman background scattering and the capability of each photonic platform to collect a Raman signal from an analyte for a given waveg-

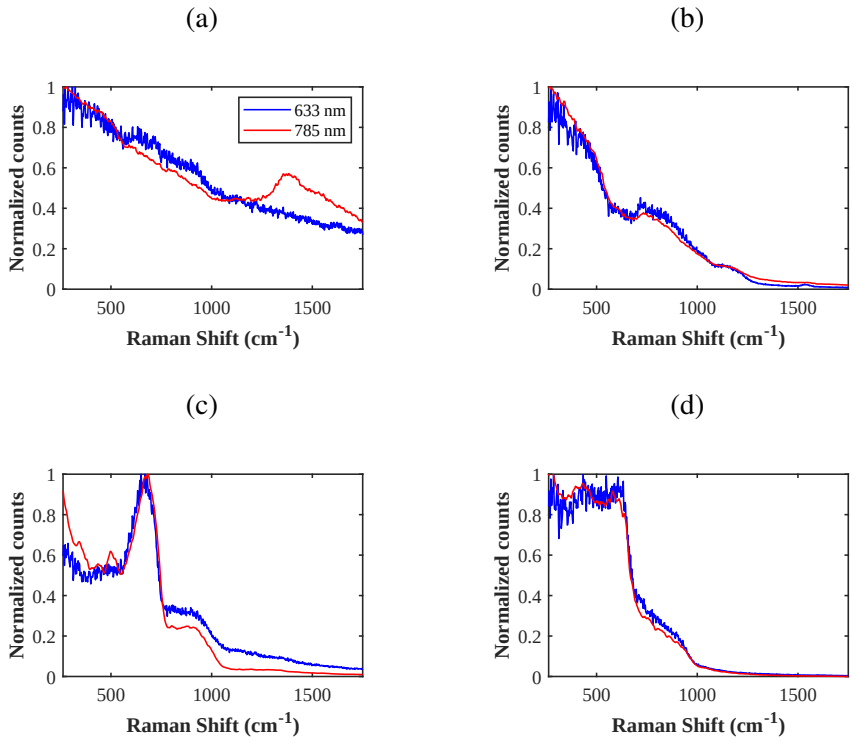

Figure 3.12: Raman spectra of air cladded a) Al_2O_3*, b)* Si_3N_4*, c)* Ta_2O_5 *and* TiO_2 *waveguides measured using 633 nm (blue) and 785 nm(red) pump wavelength.*

uide geometry, we can now establish a figure of merit for an optimized waveguide cross section of each material. Thus far, we have used the measured waveguide losses α_m in our comparison. However, because technological progress are likely to change those loss values, we are now considering the case of identical waveguide loss across the four types of waveguides: we set $\alpha = 1$ dB/cm. The figure of merit (FOM) for an optimized waveguide geometry is defined as the ratio of analyte signal strength (C^O_{sig}) to Raman background shot noise ($\sqrt{C^O_{BG}}$) where

$$C^O_{sig} = C_{sig} \times \frac{\eta_{OA}}{\eta_A} \times \frac{(LF(L_s))_{\alpha=1dB/cm}}{(LF(L_s))_{\alpha=\alpha_m}} \tag{3.7}$$

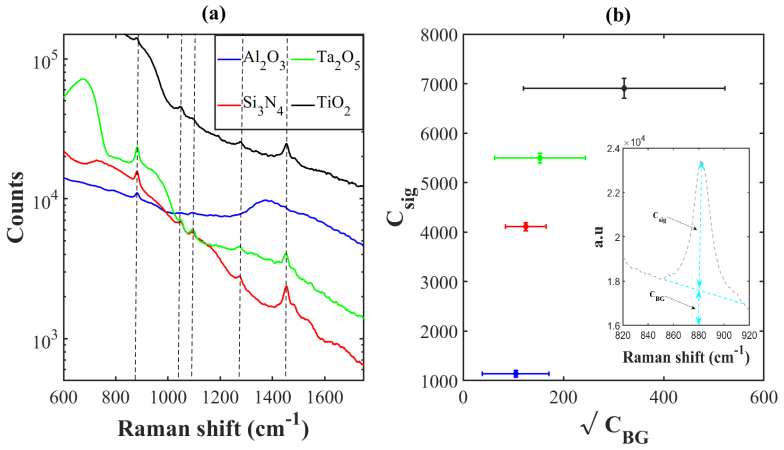

Figure 3.13: a) The Raman spectra measured from an ethanol clad waveguides of Al_2O_3, Si_3N_4, Ta_2O_5 *and* TiO_2. *The dotted lines represent the 880, 1054, 1098, 1275 and 1456* cm^{-1} *Raman modes of ethanol. b) The signal strength* C_{sig} *and background noise* $\sqrt{C_{BG}}$ *measured for 880* cm^{-1} *Raman mode of ethanol. The inset shows the* C_{sig} *and* C_{BG}.

and

$$C^{O}_{BG} = C_{BG} \times \frac{\eta_{OBG}}{\eta_{BG}} \times \frac{(LF(L_s))_{\alpha=1dB/cm}}{(LF(L_s))_{\alpha=\alpha_m}} \tag{3.8}$$

The FOM for each waveguide is presented in Table. 3.2. TiO_2 exhibits a large C^{O}_{sig} but the FOM is poor due to a large C^{O}_{BG}. Similarly for Al_2O_3, the FOM suffers due to the low C^{O}_{sig}. On the other hand, due to the low Raman background and high Raman conversion efficiency, Si_3N_4 and Ta_2O_5 have a more or less equal FOM, which is 2.7 and 3.9 times higher as compared to Al_2O_3 and TiO_2 respectively.

material	Al_2O_3	Si_3N_4	Ta_2O_5	TiO_2
$w_O \times h_O$ (nm^2)	525 × 1125	425 × 575	275 × 500	250 × 350
$\eta_{OA}(optimal)$	0.039	0.172	0.266	0.375
C^O_{sig} (counts)	$\approx 0.7 \times 10^4$	$\approx 3.2 \times 10^4$	$\approx 4.9 \times 10^4$	$\approx 7.7 \times 10^4$
C^O_{BG} (counts)	$\approx 0.8 \times 10^4$	$\approx 1.1 \times 10^4$	$\approx 2.5 \times 10^4$	$\approx 1.4 \times 10^5$
FOM=$\frac{C^O_{sig}}{\sqrt{C^O_{BG}}}$	≈ 79	≈ 305	≈ 310	≈ 116

Table 3.2: The estimated signal strength C^O_{sig} and Raman background C^O_{BG} for an optimized waveguide cross section $w_o \times h_o$. The optimal analyte Raman conversion efficiency (η_{OA}) is extracted from Fig. 3.5.

material	Si_3N_4	Ta_2O_5	TiO_2
$\eta_{OA}(optimal)$	0.59	1.1	1.5
C^O_{sig} (counts)	$\approx 1.1 \times 10^5$	$\approx 2.02 \times 10^5$	$\approx 3.1 \times 10^4$
C^O_{BG} (counts)	$\approx 0.44 \times 10^4$	$\approx 0.89 \times 10^4$	$\approx 4.4 \times 10^4$
FOM=$\frac{C^O_{sig}}{\sqrt{C^O_{BG}}}$	≈ 1658	≈ 2141	≈ 1477

Table 3.3: The estimated signal strength C^O_{sig} and Raman background C^O_{BG} for an optimized slot waveguide. The gap (g) and height (h) of all the waveguides is kept constant i.e. g = 40 nm and h = 300 nm. The optimal analyte Raman conversion efficiency (η_{OA}) is extracted from Fig. 3.8.

3.4.5 Figure of merit for an optimized slot waveguide

The Raman conversion efficiency for an optimized slot waveguide of three different refractive index is estimated in section 3.3.2. In this section, the FOM defined in the last section is computed for an optimized slot waveguide. FOM of a Si_3N_4, Ta_2O_5 and TiO_2 slot waveguides is presented in Table. 3.3. FOM for a 40 nm Si_3N_4, Ta_2O_5 and TiO_2 slot waveguides (g=40 nm, h=300 nm and w=500 nm) is approximately 5.4, 6.9 and 12.7 times larger than their respective strip waveguides. It is worth mentioning that the geometry for the slot waveguide can be improved further by optimization waveguide width and height that eventually provides even larger

FOM. Also, due to the higher field interaction with the side wall roughness, slot waveguides are more prone to the high waveguide losses. Therefore, the exact waveguide losses need to be incorporated in the FOM.

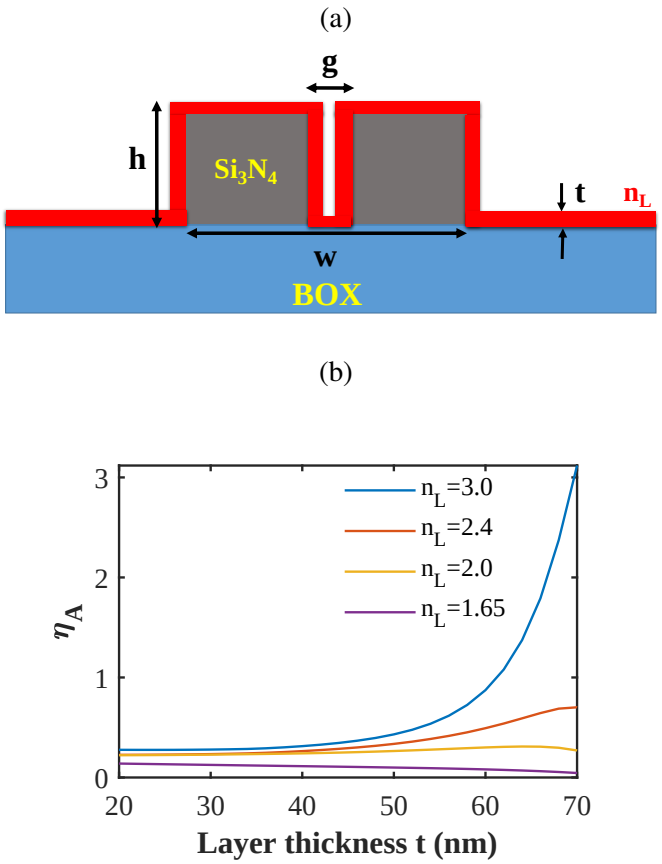

Figure 3.14: a) The schematic of an ALD coated Si_3N_4 *slot waveguide. t and* n_L *are the thickness and the refractive index of ALD layer. b) The Raman conversion efficiency* η_A *at 880* cm^{-1} *Stokes shift calculated for an ALD coated* Si_3N_4 *slot waveguides.* η_A *is computed for a fixed waveguide height (h = 300 nm) and width (w = 700 nm).*

3.5 ALD assisted narrow slot waveguides

In the last section, it was shown that the slot waveguide with a higher index and narrow slot width is always desirable for an efficient Raman spec-

troscopy. However, achieving a narrow slot demands high resolution photolithography techniques. Unfortunately, conventional optical lithography techniques i.e. DUV 193 nm optical lithography, hardly reaches to a feature size smaller than 100 nm due to the diffraction. Another way to achieve the smaller gap is using ebeam or focused ion beam lithography where structure size down to sub 10 nm [36, 37] can be achieved due to ultra-short wavelengths of electron/ion beams in the order of a few nanometers. However, the latter techniques offers low throughput [38, 39] due to dot-by-dot fashion exposure.

Another way to reduce the waveguide slot width is by filling a relatively broader slot using a conformal atomic layer deposition (ALD) coatings [40–42]. In [43, 44], a sub-5 nm gaps are realized using an ALD process. ALD is based on the successive, surface-controlled reactions from the gas phase [45]. As the reactions occur only at the surface, the process is self-limiting and the growth rate is well controlled. Also, the grown films are extremely conformal over the surface irrespective of topography. With a careful engineering, the angstrom-scale precision of the ALD process can be translated into an ultra small gaps. Moreover, this technique also leads to a high-throughput fabrication on a wafer scale level.

In this section, the signal conversion efficiency of ALD coated Si_3N_4 waveguide is analyzed. The free space excited and collected Raman background of four possible ALD materials i.e. Al_2O_3, HfO_2, TiO_2 and VO_2 is also compared.

3.5.1 Estimation of η_A of an ALD coated Si_3N_4 slot waveguide

To study the performance of an ALD coated slot waveguide, η_A is computed for four different refractive indices of possible materials that can be deposited via this method i.e. Al_2O_3, HfO_2, TiO_2 and VO_2. The schematic of the waveguide geometry is depicted in Fig. 3.14. a. A reference Si_3N_4 waveguide geometry is assumed i.e. w=700 nm, h=220 nm and g=150 nm (minimum feature size possible with 193-DUV lithography at imec). The ALD thickness (t) is swept over a range of 20 to 70 nm. The final gap after the ALD layer deposition is given by g-2$\times$t. As shown in Fig. 3.14, for an ALD layer of a refractive index $n_L < n_{Si_3N_4}$, η_A decreases with ALD layer thickness t. On the other hand, for an ALD layer of a refractive index $n_L > n_{Si_3N_4}$, η_A increases with ALD layer thickness t. For a fixed gap of g-2$\times$t, a higher refractive index layer leads to a high η_A. For example, for Si_3N_4 slot waveguide coated with 70 nm ALD layer thickness, η_A for n_L = 3 is 4.5 and 7.75 times higher than the n_L = 2.4 and n_L = 2.0, respectively. This is attributed to a higher modal overlap with analyte that resides in a smaller

gap of g-2×t.

material	Precursor	Reactant	Growth rate (nm/Cyc)	Growth T (°C)	Refractive index (NIR)
Al_2O_3	TMA	H_2O	0.1	200	1.6-1.65
HfO_2	TEMAHF	H_2O	0.07-0.08	250	1.95-2.0
TiO_2	TDMAT	H_2O	0.05-0.08	120	2.1-2.4
VO_2	TEMAV	H_2O	0.035	150	2.5-2.7

Table 3.4: The process parameters of different ALD materials. All these materials are grown at COCOON group, Ghent University.

3.5.2 Free space excited and collected Raman background of ALD Al_2O_3, HfO_2, TiO_2 and VO_2

Ideally, ALD coated slot waveguide should enhance the Raman conversion efficiency η_A without introducing any extra background signal. Therefore, due to a considerable modal confinement in the ALD layer, it is worth comparing the Raman background of the ALD layers with PECVD Si_3N_4. Based on the transparency and refractive indices in near infrared (NIR), four different ALD materials i.e. Al_2O_3, HfO_2, TiO_2 and VO_2, are deposited on a commercial calcium fluoride CaF_2 Raman substrates (purchased from Crystran Ltd., UK). ALD process parameters along with refractive indices are mentioned in Table. 3.4. The free space excited Raman background is measured using the same setup as shown in Fig. 3.9. The Raman background (with CaF_2 Raman contribution and dark counts subtracted) of four ALD material is shown in Fig. 3.15. For a fair comparison, the background of each material is scaled to 220 nm thickness (Si_3N_4 thickness). TiO_2 and VO_2 Raman spectra are scaled down by $1/10$ to plot all spectra in one window. TiO_2 and VO_2 exhibit huge Raman background as compared to Al_2O_3, Si_3N_4 and HfO_2. The Raman background of HfO_2 is comparable with PECVD Si_3N_4. Three strongest Raman peaks appear in HfO_2 Raman background at 378, 504 and 640 cm^{-1}. This corresponds well to the previous studies that shows the Raman peaks appearing due to the crystallization occurring during ALD of the thinner HfO_2 films at relatively low temperatures HfO_2 [46]. Al_2O_3 exhibits the lowest background that stays flat after 500 cm^{-1}. Considering relatively higher refractive index and low Raman background, HfO_2 can be a possible ALD material that can be used to narrow down the waveguide slot.

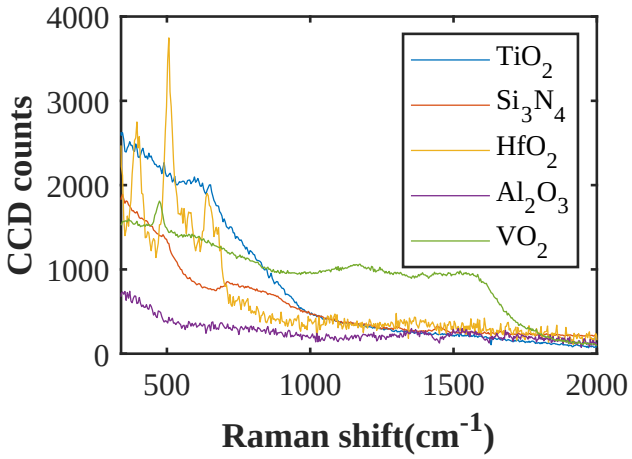

Figure 3.15: The free space excited Raman background measured from ALD Al_2O_3*,* HfO_2*,* TiO_2 *and* VO_2 *layers. All spectra are dark and* CaF_2 *background subtracted and scaled to 220 nm (*Si_3N_4 *thickness).* TiO_2 *and* VO_2 *Raman backgrounds are divided by 10.*

3.6 Comparison with other Raman sensors

In this section, we compare the performance of NWERS sensors with other existing Raman sensors e.g. fiber-based Raman sensors and Raman microscopes.

The potential of using a waveguide to enhance Raman signal was recognized as early as the late nineties and was reported in various forms, such as hollow core fiber (HCF) for gases [47] or liquid core waveguides for transparent liquids [47]. Due to the large confinement into the analyte, excitation of the Raman analyte can be enhanced, however, the collection efficiency suffers due to the large effective modal area. In the case of a hollow core fiber, the effective index of a mode and optical losses are mainly set by the analyte. To estimate the Raman conversion efficiency, a simple cylindrical hollow core fiber (CHCF) geometry proposed in [48] is considered. The internal and external radii of the fiber are set i.e r_1= 1 μm r_2= 1.2 μm. The modal profile of liquid (ethanol) filled cylindrical hollow core fiber at 785 nm wavelength is depicted in Fig. 3.16. The waveguide mode is excited at 785 nm pump wavelength. Assuming the fundamental mode, the Raman conversion efficiency (η_A) calculated using Eq 3.4 is 0.46. In

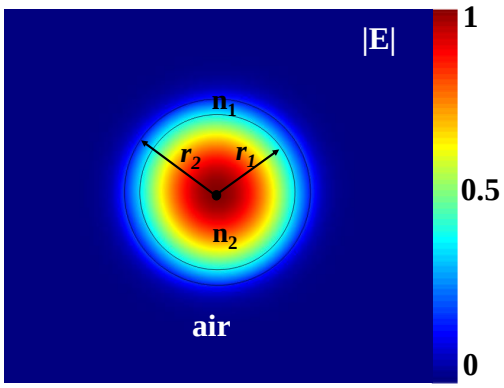

Figure 3.16: The electric field strength $|E|$ of a cylindrical hollow core fiber at 800 nm wavelength. r_1 and r_2 are 1 and 1.2 μm respectively. Similarly, n_1 = 1.44 (silica) and n_2 =1.37 (ethanol). Raman conversion efficiency (η_A) for this hollow core fiber is 0.46.

simulations, we assume ethanol (n_a=1.37) as an analyte at the Raman detuning of the 880 cm^{-1} line. The Raman conversion efficiency of CHCF is comparable to a TE excited single mode Si_3N_4 slot waveguide (shown in Fig. 3.7). The major benefit of the CHCF comes from the following two properties: low Raman background due to the negligible overlap with the silica ($<5\%$) and low propagation ($<$100 dB/Km loss [49]). Due to the ultra low propagation loss, HCF can boost the signal by a factor 10^3. Therefore, high sensitivity can be achieved using liquid filled hollow core fibers. However, as mentioned before, due to the large field confinement in the analyte, the absorption of the analyte will greatly influence the interaction length. Also, unlike a HIC waveguide, the large bending radius of HCF inhibits miniaturization. Moreover, filling a HCF with an analyte is difficult and time consuming. A standard filling process involves the inherit capillary effect that depends on the viscosity and the surface tension. To speed up the process, pressure syringes are also used [50], however filling a long HCF still takes a few minutes to an hour.

Next, we compare the performance of NWERS sensors with a diffraction limited Raman microscope (DLRM). The ratio (ϕ) of total collected Raman power in a Si_3N_4 waveguide to that of DLRM for a bulk analyte is shown in Fig. 3.17. Depending on the waveguide structure, ϕ can be 100 to 3000. The huge enhancement is attributed to the confined modal field and long interaction length of a NWERS sensor. The major advantage in the case of DLRM comes from a negligible Raman background that eventually

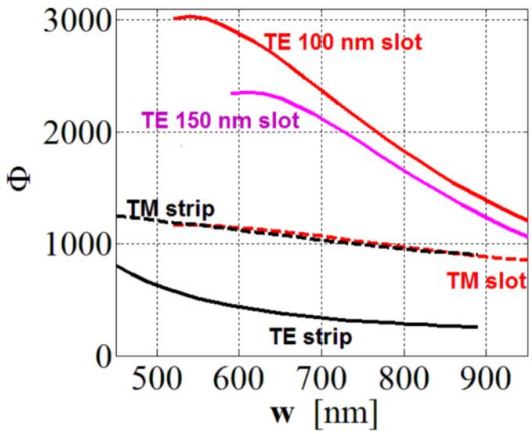

Figure 3.17: Theoretical values for the enhancement factor ϕ compared to the diffraction limited confocal microscope as a function of waveguide width for 1 cm strip and slot silicon nitride waveguides. The height of the waveguide is fixed i.e. 220 nm. The figure is taken from [52].

enhances the signal to noise ratio.

A qualitative comparison of a NWERS sensor vs CHCF and a diffraction limited Raman microscope is presented in Table. 3.5. In term of Raman signal strength, NWERS sensor and cylindrical HCF, clearly wins over a DLRM. On the other hand, there is no Raman background generated in the case of DLRM that leads to high signal to ratio. Due to the small bend radius of high index contrast photonic waveguide, NWERS sensors can be miniaturized using the waveguide spirals. Similarly, NWERS sensors also hold the promise of integration of more photonic functionalities such as spectral filtering of the pump beam [21], spectrometers [22, 23], possibly lasers [24, 25] and detectors [26] that can lead to a complete on-chip Raman spectroscope. An analyte can be applied to a NWERS sensors simply using a drop-casting. On the other hand, in the case of CHCF, pressure syringes are needed to fill a fiber. Also, considering the active multi-project wafer (MPW) runs and total volume, the cost of the NWERS sensor can be just a few euros/mm^2 to few hundred euros/mm^2 [51].

sensor	NWERS	Raman microscope	Cylindrical hollow core fiber
signal strength	***	*	***
low Raman background	*	***	**
miniaturization	***	*	**
cost efficient	***	*	***
ease of use	***	***	*
photonics integration	***	*	**

*Table 3.5: The qualitative comparison of a NWERS sensor vs diffraction limited Raman microscope and cylindrical hollow core fiber. *** = best, **=moderate, *=worse.*

3.7 Conclusion

To conclude, we present the waveguide enhanced Raman spectroscopy where the dielectric waveguide itself acts as a Raman sensor. The analytical formalism to quantify the Stokes to pump conversion efficiency of a waveguide is presented. Next, we compare the performance of four different photonic integration platforms (Al_2O_3, Si_3N_4, Ta_2O_5 and TiO_2) as an on-chip Raman spectroscopy platform. The performance is compared in terms of Stokes to pump conversion efficiency and the Raman background of the waveguide material. A first comparison is made accounting for the current technological fabrication capability and resulting propagation loss. A more general comparison is made that factors out the loss therefore looking forward at technological improvements. From this we can draw a number of conclusions. Due to the higher index contrast, TiO_2 waveguides exhibit the highest Raman conversion efficiency. However, the signal-to-background ratio is relatively poor due to the high Raman background. On the other hand, Al_2O_3 waveguides exhibit weak Raman background, but the signal collection efficiency suffers due to the low index contrast. Si_3N_4 and Ta_2O_5 strip waveguides seem to be nearly equally good platforms for Raman spectroscopy as their Raman background is rather low but their capability to collect the Raman signal from the analyte is strong. In practice, the loss in Si_3N_4 waveguides being lower than in Ta_2O_5 waveguides, it is presently more advantageous to use Si_3N_4. With the progress in making low loss waveguides, any of the investigated photonic platform could

become the best one as long as the waveguide loss is primarily due to the waveguide itself. In case the loss is dominated by the analyte, the figure of merit given in Table. 3.2 gives a definite answer on what technology is ideal. We also proposed NWERS using ALD coated Si_3N_4 slot waveguides. The simulation results for the Stokes to pump conversion efficiency of 70 nm thick ALD layer coated Si_3N_4 slot waveguide shows a 7.5 times improvement over an uncoataed waveguide. In the end, we briefly compared Raman background of four possible ALD coatings i.e. Al_2O_3, HfO_2, TiO_2 and VO_2, that can be used to coat Si_3N_4 for an efficient NWERS. The Raman background of ALD VO_2 is comparable to TiO_2 that is about 8 times stronger than PECVD Si_3N_4. On the other hand, ALD HfO_2 exhibits moderate Raman background that is comparable with PECVD Si_3N_4.

As mentioned before, in NWERS a dielectric waveguide acts as a Raman sensor where the major improvement comes from two phenomena: an enhanced spontaneous emission due to high index contrast waveguide and few centimeters long light-analyte interaction length. NWERS has shown considerable potential in many sensing applications comprising analytes in different phases i.e. in bulk and gases. However, for ultra small analytes i.e. monolayers, further signal enhancement is needed. In the subsequent chapters, we present another modality i.e. plasmonics, where Raman signal can be further enhanced by many folds, thanks to the high electric field enhancement offered by plasmonic structures.

References

[1] Y Levy, C Imbert, J Cipriani, S Racine, and R Dupeyrat. *Raman scattering of thin films as a waveguide*. Optics communications, 11(1):66–69, 1974.

[2] JF Rabolt, R Santo, and JD Swalen. *Raman spectroscopy of thin polymer films using integrated optical techniques*. Applied Spectroscopy, 33(6):549–551, 1979.

[3] JF Rabolt, R Santo, and JD Swalen. *Raman measurements on thin polymer films and organic monolayers*. Applied spectroscopy, 34(5):517–521, 1980.

[4] JP Rabe, JD Swalen, and JF Rabolt. *Order–disorder transitions in Langmuir–Blodgett films. III. Polarized Raman studies of cadmium arachidate using integrated optical techniques*. The Journal of chemical physics, 86(3):1601–1607, 1987.

[5] Johannes Sake Kanger, Cees Otto, Michiel Slotboom, and Jan Greve. *Waveguide Raman Spectroscopy of Thin Polymer Layers and Monolayers of Biomolecules Using High Refractive Index Waveguides*. The Journal of Physical Chemistry, 100(8):3288–3292, 1996.

[6] A Pope, A Schulte, Y Guo, LK Ono, B Roldan Cuenya, C Lopez, K Richardson, K Kitanovski, and T Winningham. *Chalcogenide waveguide structures as substrates and guiding layers for evanescent wave Raman spectroscopy of bacteriorhodopsin*. Vibrational spectroscopy, 42(2):249–253, 2006.

[7] Ashim Dhakal, Ali Raza, Pieter Wuytens, Frédéric Peyskens, Andre Skirtach, Nicolas Le Thomas, and Roel Baets. *Lab-on-a-chip Raman sensors outperforming Raman microscopes*. In 2016 Conference on Lasers and Electro-Optics (CLEO), pages 1–2. IEEE, 2016.

[8] Lev Gasparov, Theo Jegorel, Lars Loetgering, Srimanta Middey, and Jak Chakhalian. *Thin film substrates from the Raman spectroscopy point of view*. Journal of Raman Spectroscopy, 45(6):465–469, 2014.

[9] Ashim Dhakal, Ananth Z. Subramanian, Pieter Wuytens, Frédéric Peyskens, Nicolas Le Thomas, and Roel Baets. *Evanescent excitation and collection of spontaneous Raman spectra using silicon nitride nanophotonic waveguides*. Opt. Lett., 39(13):4025–4028, Jul 2014.

[10] Christopher C. Evans, Chengyu Liu, and Jin Suntivich. *TiO2 Nanophotonic Sensors for Efficient Integrated Evanescent Raman Spectroscopy*. ACS Photonics, 3(9):1662–1669, 2016.

[11] Scott A. Holmstrom, Todd H. Stievater, Dmitry A. Kozak, Marcel W. Pruessner, Nathan Tyndall, William S. Rabinovich, R. Andrew McGill, and Jacob B. Khurgin. *Trace gas Raman spectroscopy using functionalized waveguides*. Optica, 3(8):891–896, Aug 2016.

[12] Ashim Dhakal, Pieter C. Wuytens, Frdric Peyskens, Karolien Jans, Nicolas Le Thomas, and Roel Baets. *Nanophotonic Waveguide Enhanced Raman Spectroscopy of Biological Submonolayers*. ACS Photonics, 3(11):2141–2149, 2016.

[13] D. A. Coucheron, D. N. Wadduwage, G. S. Murugan, P. T. C. So, and B. S. Ahluwalia. *Chip-Based Resonance Raman Spectroscopy Using Tantalum Pentoxide Waveguides*. IEEE Photonics Technology Letters, pages 1–1, 2019.

[14] Ashim Dhakal, Ali Raza, Frédéric Peyskens, Ananth Z. Subramanian, Stéphane Clemmen, Nicolas Le Thomas, and Roel Baets. *Efficiency of evanescent excitation and collection of spontaneous Raman scattering near high index contrast channel waveguides*. Opt. Express, 23(21):27391–27404, Oct 2015.

[15] Derek M. Kita, Jérôme Michon, Steven G. Johnson, and Juejun Hu. *Are slot and sub-wavelength grating waveguides better than strip waveguides for sensing?* Optica, 5(9):1046–1054, Sep 2018.

[16] Ashim Dhakal, Pieter Wuytens, Ali Raza, Nicolas Le Thomas, and Roel Baets. *Silicon nitride background in nanophotonic waveguide enhanced Raman spectroscopy*. Materials, 10(2):140, 2017.

[17] Nathan F Tyndall, Todd H Stievater, Dmitry A Kozak, Kee Koo, R Andrew McGill, Marcel W Pruessner, William S Rabinovich, and Scott A Holmstrom. *Waveguide-enhanced Raman spectroscopy of trace chemical warfare agent simulants*. Optics letters, 43(19):4803–4806, 2018.

[18] Zilong Wang, Stuart J Pearce, Yung-Chun Lin, Michalis N Zervas, Philip N Bartlett, and James S Wilkinson. *Power budget analysis for waveguide-enhanced Raman spectroscopy*. Applied spectroscopy, 70(8):1384–1391, 2016.

[19] Nicolas Le Thomas, Ashim Dhakal, Ali Raza, Frédéric Peyskens, and Roel Baets. *Impact of fundamental thermodynamic fluctuations on light propagating in photonic waveguides made of amorphous materials*. Optica, 5(4):328–336, Apr 2018.

[20] Frdric Peyskens, Ashim Dhakal, Pol Van Dorpe, Nicolas Le Thomas, and Roel Baets. *Surface Enhanced Raman Spectroscopy Using a Single Mode Nanophotonic-Plasmonic Platform*. ACS Photonics, 3(1):102–108, 2016.

[21] Alexander Gondarenko, Jacob S. Levy, and Michal Lipson. *High confinement micron-scale silicon nitride high Q ring resonator*. Opt. Express, 17(14):11366–11370, Jul 2009.

[22] Xiaomin Nie, Eva Ryckeboer, Gunther Roelkens, and Roel Baets. *CMOS-compatible broadband co-propagative stationary Fourier transform spectrometer integrated on a silicon nitride photonics platform*. Opt. Express, 25(8):A409–A418, Apr 2017.

[23] Daan Martens, Ananth Z Subramanian, Shibnath Pathak, Michael Vanslembrouck, Peter Bienstman, Wim Bogaerts, and Roel Baets. *Compact silicon nitride arrayed waveguide gratings for very near-infrared wavelengths*. IEEE Photon. Technol. Lett., 27(2):137–140, 2015.

[24] Zhiping Zhou, Bing Yin, and Jurgen Michel. *On-chip light sources for silicon photonics*. Light: Science & Amp; Applications, 4(8):e358, Nov 2015.

[25] Emanuel P. Haglund, Sulakshna Kumari, Petter Westbergh, Johan S. Gustavsson, Gunther Roelkens, Roel Baets, and Anders Larsson. *Silicon-integrated short-wavelength hybrid-cavity VCSEL*. Opt. Express, 23(26):33634–33640, Dec 2015.

[26] Jurgen Michel, Jifeng Liu, and Lionel C Kimerling. *High-performance Ge-on-Si photodetectors*. Nature Photonics, 4(8):527, 2010.

[27] Przemek J Bock, Pavel Cheben, Jens H Schmid, Jean Lapointe, André Delâge, Siegfried Janz, Geof C Aers, Dan-Xia Xu, Adam Densmore, and Trevor J Hall. *Subwavelength grating periodic structures in silicon-on-insulator: a new type of microphotonic waveguide*. Optics express, 18(19):20251–20262, 2010.

[28] Vilson R Almeida, Qianfan Xu, Carlos A Barrios, and Michal Lipson. *Guiding and confining light in void nanostructure*. Optics letters, 29(11):1209–1211, 2004.

[29] Carlos Angulo Barrios, Benito Sánchez, Kristinn Bjrgvin Gylfason, Amadeu Griol, Hans Sohlström, Miquel Holgado, and Raphael Casquel. *Demonstration of slot-waveguide structures on silicon nitride/silicon oxide platform*. Optics express, 15(11):6846–6856, 2007.

[30] Young Chul Jun, Ryan M Briggs, Harry A Atwater, and Mark L Brongersma. *Broadband enhancement of light emission in silicon slot waveguides*. Optics Express, 17(9):7479–7490, 2009.

[31] Ali Raza, Stéphane Clemmen, Pieter Wuytens, Michiel de Goede, Amy S. K. Tong, Nicolas Le Thomas, Chengyu Liu, Jin Suntivich, Andre G. Skirtach, Sonia M. Garcia-Blanco, Daniel J. Blumenthal, James S. Wilkinson, and Roel Baets. *High index contrast photonic platforms for on-chip Raman spectroscopy*. Opt. Express, 27(16):23067–23079, Aug 2019.

[32] AZ Subramanian, Pieter Neutens, Ashim Dhakal, Roelof Jansen, Tom Claes, Xavier Rottenberg, Frédéric Peyskens, Shankar Selvaraja, Philippe Helin, Bert Du Bois, et al. *Low-loss singlemode PECVD silicon nitride photonic wire waveguides for 532–900 nm wavelength window fabricated within a CMOS pilot line*. IEEE Photonics Journal, 5(6):2202809–2202809, 2013.

[33] Zilong Wang, Michalis N. Zervas, Philip N. Bartlett, and James S. Wilkinson. *Surface and waveguide collection of Raman emission in waveguide-enhanced Raman spectroscopy*. Opt. Lett., 41(17):4146–4149, Sep 2016.

[34] Takashi Tsuchiya, Hideto Imai, Shogo Miyoshi, Per-Anders Glans, Jinghua Guo, and Shu Yamaguchi. *X-Ray absorption, photoemission spectroscopy, and Raman scattering analysis of amorphous tantalum oxide with a large extent of oxygen nonstoichiometry*. Phys. Chem. Chem. Phys., 13:17013–17018, 2011.

[35] Alan Mortensen, DH Christensen, O Faurskov Nielsen, and E Pedersen. *Broad background bands in Raman spectra of alumina studied by both visible and near-infrared excitation*. Journal of Raman spectroscopy, 24(10):667–673, 1993.

[36] Rajesh Menon, Amil Patel, Dario Gil, and Henry I Smith. *Maskless lithography*. Materials Today, 8(2):26–33, 2005.

[37] Matteo Altissimo. *E-beam lithography for micro-/nanofabrication*. Biomicrofluidics, 4(2):026503, 2010.

[38] R Fabian Pease and Stephen Y Chou. *Lithography and other patterning techniques for future electronics*. Proceedings of the IEEE, 96(2):248–270, 2008.

[39] Alongkorn Pimpin and Werayut Srituravanich. *Review on micro-and nanolithography techniques and their applications*. Engineering Journal, 16(1):37–56, 2012.

[40] Tapani Alasaarela, Antti Säynätjoki, Teppo Hakkarainen, and Seppo K Honkanen. *Feature size reduction of silicon slot waveguides by partial filling using atomic layer deposition*. Optical Engineering, 48(8):080502, 2009.

[41] A Säynätjoki, T Alasaarela, A Khanna, L Karvonen, P Stenberg, M Kuittinen, A Tervonen, and S Honkanen. *Angled sidewalls in sil-*

icon slot waveguides: conformal filling and mode properties. Optics Express, 17(23):21066–21076, 2009.

[42] T Alasaarela, D Korn, L Alloatti, A Säynätjoki, A Tervonen, R Palmer, J Leuthold, W Freude, and S Honkanen. *Reduced propagation loss in silicon strip and slot waveguides coated by atomic layer deposition*. Optics express, 19(12):11529–11538, 2011.

[43] Xiaoshu Chen, Hyeong-Ryeol Park, Matthew Pelton, Xianji Piao, Nathan C Lindquist, Hyungsoon Im, Yun Jung Kim, Jae Sung Ahn, Kwang Jun Ahn, Namkyoo Park, et al. *Atomic layer lithography of wafer-scale nanogap arrays for extreme confinement of electromagnetic waves*. Nature communications, 4:2361, 2013.

[44] Dengxin Ji, Alec Cheney, Nan Zhang, Haomin Song, Jun Gao, Xie Zeng, Haifeng Hu, Suhua Jiang, Zongfu Yu, and Qiaoqiang Gan. *Efficient Mid-Infrared Light Confinement within Sub-5-nm Gaps for Extreme Field Enhancement*. Advanced Optical Materials, 5(17):1700223, 2017.

[45] Tuomo Suntola and Jorma Antson. *Method for producing compound thin films*, November 15 1977. US Patent 4,058,430.

[46] SN Tkachev, MH Manghnani, A Niilisk, J Aarik, and H Mändar. *Micro-Raman spectroscopy and X-ray diffraction studies of atomic-layer-deposited ZrO 2 and HfO 2 thin films*. Journal of materials science, 40(16):4293–4298, 2005.

[47] Fetah Benabid, Jonathan C Knight, G Antonopoulos, and P St J Russell. *Stimulated Raman scattering in hydrogen-filled hollow-core photonic crystal fiber*. Science, 298(5592):399–402, 2002.

[48] Pietro Patimisco, Vincenzo Spagnolo, Miriam Vitiello, Gaetano Scamarcio, Carlos Bledt, and James Harrington. *Low-loss hollow waveguide fibers for mid-infrared quantum cascade laser sensing applications*. Sensors, 13(1):1329–1340, 2013.

[49] Benoît Debord, Foued Amrani, Luca Vincetti, Frédéric Gérôme, and Fetah Benabid. *Hollow-core fiber technology: The rising of gas photonics*. Fibers, 7(2):16, 2019.

[50] FM Cox, A Argyros, and MCJ Large. *Liquid-filled hollow core microstructured polymer optical fiber*. Optics Express, 14(9):4135–4140, 2006.

[51] Abdul Rahim, Thijs Spuesens, Roel Baets, and Wim Bogaerts. *Open-access silicon photonics: Current status and emerging initiatives*. Proceedings of the IEEE, 106(12):2313–2330, 2018.

[52] Ashim Dhakal, Pieter Wuytens, Frederic Peyskens, Ananth Subramanian, Andre Skirtach, Nicolas Le Thomas, and Roel Baets. *Nanophotonic Lab-On-A-Chip Raman sensors: a sensitivity comparison with confocal Raman microscope*. In 2015 International Conference on BioPhotonics (BioPhotonics), pages 1–4. IEEE, 2015.

4

Plasmon Physics

4.1 Introduction

In the previous chapter, we discussed Raman spectroscopy using the dielectric waveguides. Inspite of the added value of NWERS to the integrated platform, applications requiring ultra high sensitivity are pushing for further signal enhancement. Also, the typical power of on-chip integrated lasers (in few milliwatts) constitutes another motivation to enhance the Raman conversion efficiency. The extreme optical properties of plasmonic nano-structures enables a variety of optical functionalities (sensing [1], modulation [2], non-linear processing) at low power and in sub-micron foot-prints. Due to the highly localized field near a plasmonic structure, the weak Raman scattering can be enhanced by many folds. This phenomenon is called surface enhanced Raman scattering (SERS). SERS is the most profound application of plasmonics known to date.

In this chapter, the physics of the surface plasmon polariton (SPP) and localized surface plasmon (LSP) is presented. The field enhancement related to LSP and its role in boosting the surface enhanced Raman signal is also briefly discussed. The formalism used in the subsequent sections consist of the Maxwell's equations followed by the application of boundary conditions. Finally, using the Drude's model to estimate permittivity, the dispersion relation are derived.

4.2 Plasmon Physics

Plasmons are the quantized oscillations of the electron density in a metal. At the surface of metal, a plasmon can couple with a photon to create another quasiparticle called a surface plasmon polariton. As we will see in the following sections, there are three classes of the surface plasmon polaritons i.e. propagating surface plasmon polaritons, bulk plasmon and localized surface plasmons. Depending on the wavelength of operation, a metal-dielectric system can exhibit either a bulk or a surface plasmon polariton.

4.2.1 Surface Plasmons

Let's assume a metal-dielectric interface as shown in Fig. 4.1. ϵ_D and ϵ_M are the dielectric constants for the dielectric and metal. The plasmon mode is propagating along the interface i.e. K_{sp} is along the x direction. The dispersion relation for a TM polarized light i.e. (E_x, 0, E_z) and (0,H_y,0) is given by

$$K_{sp}(\omega) = \frac{\omega}{c}\sqrt{\frac{\epsilon_D \epsilon_M}{\epsilon_D + \epsilon_M}} \tag{4.1}$$

According to the generalized Drude theory, the permitivity of a metal can be written as [3]

$$\epsilon_M(\omega) = \epsilon_{int} - \frac{\omega_p^2}{\omega^2 + \iota\omega\tau} \tag{4.2}$$

where τ is the total decay rate and ϵ_{int} is the contribution due to the inter-band transitions. ω_p is the plasma frequency that depends on the electron charge e, effective mass $\mathrm{m_e}$ and density $\mathrm{n_e}$:

$$\omega_p^2 = \frac{n_e e^2}{\epsilon_o m_e} \tag{4.3}$$

In the subsequent section, we will derive the conditions necessary for a material to exhibit the plasmonic properties. Lets assume a perfectly free electron gas i.e. ϵ_{int} = 1 and τ = 0. The dispersion relation is now given as

$$\frac{cK_{sp}(\omega)}{\omega_p} = \frac{\omega}{c}\sqrt{\frac{1 - \frac{\omega_p^2}{\omega^2}}{2 - \frac{\omega_p^2}{\omega^2}}} \tag{4.4}$$

Solution to Eq.4.4 is plotted in Fig. 4.2. K_{sp} is splitted into two solutions i.e. solution 1 in the range $0 < \omega < 0.707\omega_p$ and solution II in the range of $\omega > \omega_p$. The frequency at $0.707\omega_p$ is the classical surface plasmon frequency for a metal-air system. Solution I corresponds to the surface

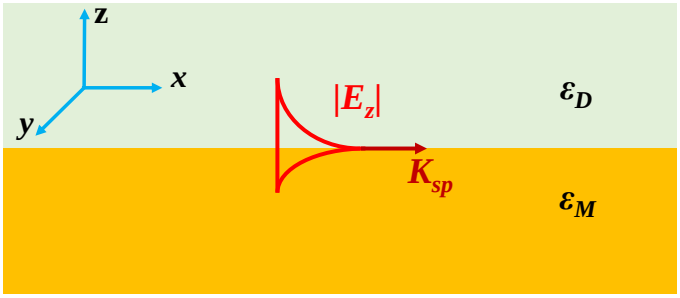

Figure 4.1: The schematic of the field of a surface plasmon polariton (SPP). ϵ_D and ϵ_D represent the permittivity of a dielectric and a metal respectively.

plasmon (SP) mode while the solution II relates to the bulk plasmon (BP) mode. No solution exists for the frequencies $0.707\omega_p < \omega < \omega_p$. This corresponds to the region where the permitivity of the metal is just below 0 i.e. -1 $< \epsilon_M <$ 0. At $\omega = 0.707\omega_p$, the K_{sp} saturates i.e. $\frac{\partial\omega}{\partial K_{sp}} <<$ c. At this frequency

$$\mathbb{R}(\epsilon_M) = -\epsilon_D \tag{4.5}$$

This is called non-retarded SP regime. On the other hand, retarted SP regime corresponds to the $\omega << 0.707\omega_p$. At this frequency the K_{sp} converges to free space K i.e. $\frac{\partial\omega}{\partial K_{sp}}$ = c. On the other hand for bulk plasmon solutions when K_{sp} approaches K_{BP}, metal behaves as a normal dielectric medium with $\epsilon_M > 0$.

The SPP field decay length is determined by

$$L_i = \frac{c}{\omega}\sqrt{\frac{\epsilon_D + \epsilon_M}{\epsilon_i^2}} \tag{4.6}$$

Usually, the dielectric constant of a metal is much larger than the dielectric i,e, $\epsilon_M > \epsilon_D$, therefore the L_M is shorter as compared to the L_D. For example for a silver-air interface, at 600 nm wavelength, L_{silver} = 24 nm and L_{air} = 390 nm. Likewise, for a a gold-air interface, at L_{gold} = 31 nm and L_{air} = 280 nm. This leads to highly concentrated field next to the metal-dielectric interface [4].

As shown in Fig. 4.2, the light line always stays above the K_{SPP}. This means that light hitting to a metal-dielectric interface in an arbitrary direction will not couple to the surface plasmon. A special configuration

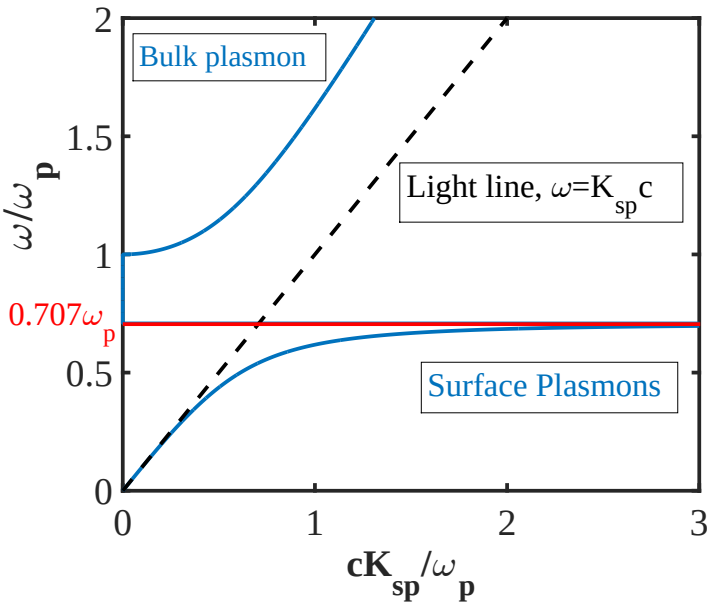

Figure 4.2: The dispersion graph of plasmon modes in a metal-air interface. The dotted line represents the light line. For $\omega < 0.707\ \omega_p$, modes are surface plasmon modes and for $\omega > \omega_p$, modes are bulk plasmon modes.

is needed to couple the light via a prism coupler [5] or periodic corrugation [6]. In the so called Kretschmann configuration, a prism with a dielectric permittivity is used to excite the surface plasmon. As shown in Fig. 4.3, a thin metal layer is used along the one facet of the prism. The metal-dielectric facet is illuminated at an angle greater than the total international reflection angle. The coupling to SPP occurs when the in plane component of the wave vector matches with the K_{sp} i.e.

$$\frac{\omega}{c}\sqrt{\epsilon_P} sin(\theta_{SP}) = K_{sp} \tag{4.7}$$

At θ_{SP}, a sharp minimum is observed in the reflection measurement. θ_{SP} is highly sensitive to the variations in the refractive index of the surface allowing the monitoring of ultra-thin films grown very close to the metal interface. Therefore, a slight change in the surrounding e.g. a layer on the gold surface or refractive index of dielectric etc. can be probed using the reflection measurements. This phenomenon is called SPR sensing [7, 8]. Sensor development and studies about kinetics of interaction between bio molecules [9, 10] are the most investigated applications in this field.

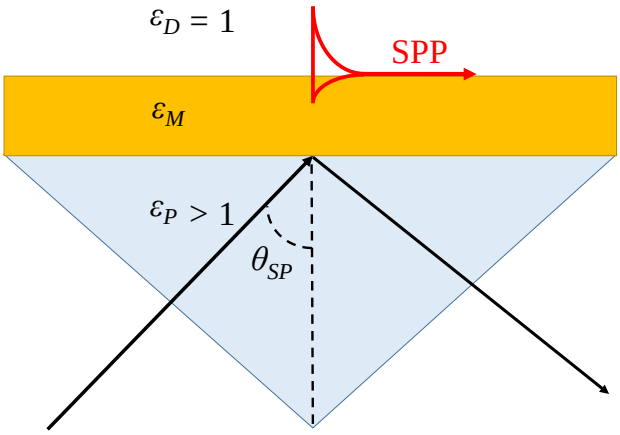

Figure 4.3: Kretschmann configuration to excite SPPs by wavevector matching using photon tunnelling in a total internal reflection geometry.

Surface plasmon modes can also be excited using the optical fibers and channel waveguides. To get an overview of optical fiber and waveguide based SPR sensing, readers are suggested to read [11, 12].

4.2.2 Localized Surface Plasmon Resonances

In the last section, we have seen that SPPs are the propagating electromagnetic waves coupled to the electron plasma at the metal-dielectric interface. Localized surface plasmon modes on the other hand are non-propagating modes that arise when a sub-wavelength conductive nanoparticle interact with oscillating electromagnetic field. Due to the non uniform surface of the particle i.e. spherical, a restoring force is applied on the electrons that leads to a resonance called localized surface plasmon resonance (LSPR). A striking consequence of this is the bright colors exhibited by particles both in transmitted and reflected light, due to resonantly enhanced absorption and scattering cross sections. As we will see later, for gold and silver particles, LSPR lies in the the visible wavelength. This effect has found applications for many hundreds of years, for example in the staining of glass for windows or ornamental cups for decoration.

For an analytical treatment, let us assume the simplest geometry of the conducting nanoparticle i.e a nano-sphere of the size d $<<$ λ. Further assume that the nanoparticle is immersed in a dispersionless and lossless

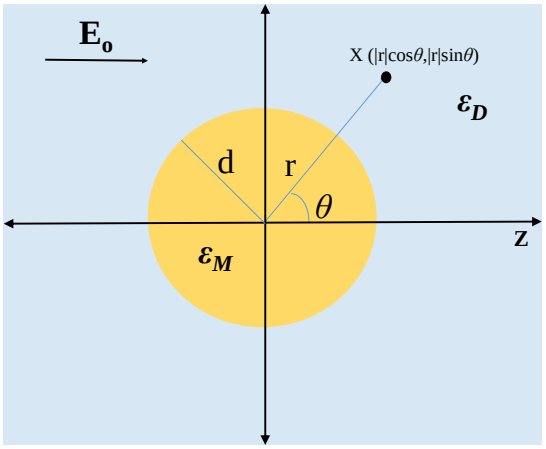

Figure 4.4: The schematic of a metallic nanoparticle placed into an electrostatic field. The surrounding environment is a dielectric medium of permittivity ϵ_D.

medium of the permittivity ϵ_D. The schematic of this problem is shown in Fig. 4.4. In this scenario, one can assume a constant phase of EM waves across the nanoparticle. Therefore, a quasi-static approximation can be applied to extract the spatial field distribution. When $\nabla \times E$ = 0, then the electric field can be extracted from the gradient of electric potential V_E

$$E = -\nabla V_E \tag{4.8}$$

Now using Gauss's law,

$$\nabla.E = \nabla.(-\nabla V_E) = \nabla^2 V_E = 0 \tag{4.9}$$

Since the problem holds an azimuthal symmetry, the general solution of Eq. 4.9 will be [13]

$$V_E(r,\theta) = \sum_{n=0}^{\infty}[A_n r^n + B_n r^{-(n+1)}]P_n(cos\theta) \tag{4.10}$$

where $P_n cos\theta$ are the Legendre Polynomials (orthogonal system) of order n, and θ is the angle between the position vector r at point x ($rsin\theta$,$rcos\theta$) and the z-axis. For the condition that $V_E(r,\theta)$ must remain finite at the origin, Eq. 4.10 can be split into two solutions: inside the sphere

$$V_{Ein}(r,\theta) = \sum_{n=0}^{\infty} A_n r^n P_n(cos\theta) \quad for \quad r < d \tag{4.11}$$

and outside the sphere

$$V_{Eout}(r,\theta) = \sum_{n=0}^{\infty}[B_n r^n + C_n r^{-(n+1)}]P_n(cos\theta) \quad for \quad r > d \quad (4.12)$$

The coefficients A_n, B_n and C_n can be determined by applying the boundary conditions at r $\rightarrow \infty$ and r = d. At r $\rightarrow \infty$, $B_1 = E_o$ and $B_n = 0$ for n$\neq$1. Now at r = d, the tangential components of the electric field demands

$$\frac{1}{d}\frac{\partial V_{Ein}}{\partial \theta} = \frac{1}{d}\frac{\partial V_{Eout}}{\partial \theta} \quad (4.13)$$

And the continuity of the normal components of the displacement field

$$\epsilon_o \epsilon_M \frac{\partial V_{Ein}}{\partial r} = \epsilon_o \epsilon_D \frac{\partial V_{Eout}}{\partial r} \quad (4.14)$$

By putting Eq. 4.11 and Eq. 4.12 in Eq. 4.13 and Eq. 4.14, remaining coefficients can be computed i.e. $A_n = C_n = 0$ for n $\neq$ 1. For n=1 (dipole mode), The V_E is now given as [13, 14]

$$V_{Ein}(r,\theta) = -\frac{3\epsilon_D}{\epsilon_M + 2\epsilon_D} E_o r(cos\theta) \quad (4.15)$$

$$V_{Eout}(r,\theta) = -E_o r(cos\theta) + \frac{\epsilon_M - \epsilon_D}{\epsilon_M + 2\epsilon_D} E_o d^3 \frac{cos\theta}{r^2} \quad (4.16)$$

In the derivation of the above equations the differential properties of Legendre function mentioned in [15] are used. By applying Eq. 4.8, 4.15 and 4.16, it can be seen that both the internal E_{in} and external dipolar fields E_{out} shows a resonance effect for the following condition

$$\mathbb{R}(\epsilon_M) = -2\epsilon_D \quad (4.17)$$

This field enhancement at the plasmon resonance allows many applications i.e. sensing [1] and modulation [2]. This resonance mode at ω_{LSP} is called dipole localized surface plasmon mode of a nanoparticle. For a metal whose permittivity follows the Drude model, this condition is satisfied at the frequency ω_{LSP}. Eq. 4.5 suggests that the resonance strongly depends on the dielectric perimittivity. The resonance red shifts as

$$\omega_{LSP} = \omega_P \sqrt{\frac{1}{1 + 2\epsilon_D}} \quad (4.18)$$

Eq. 4.5 suggests that ω_{LSP} strongly depends on the dielectric perimittivity. ω_{LSP} red shifts as ϵ_D is increased, thus making these sub-wavelength

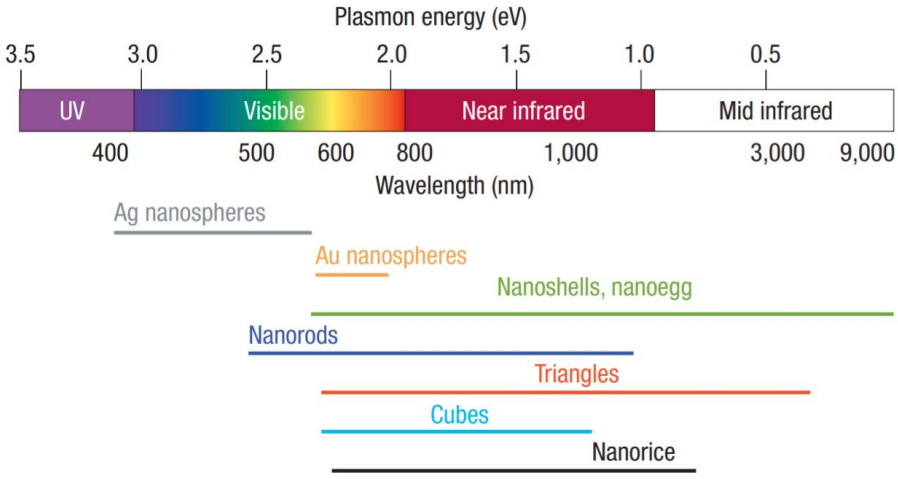

Figure 4.5: The resonance wavelength range of different plasmonic structures. Taken from [1].

plasmonic antennas an excellent platform for refractive index sensing [16, 17]. Also, ω_{LSP} depends on the size of the nanoparticle. In [11], it is shown that the extinction cross section (C_{sca}) scales with the volume of sphere. Therefore, the nanoparticle size can be engineered to have the resonance in the wavelength range of our interest [18]. This phenomenon finds applications in surface enhanced Raman spectroscopy. The resonance wavelengths of different plasmonic structures are depicted in Fig. 4.5. It is worth mentioning that for the large particle size, the quasi-static approximation does not hold anymore. Mie scattering can be used for bigger spherical nanoparticles [19]. Similarly, Gans theory can be used to any general shape of the particle i.e. spheroidal particles [7].

4.2.3 Electromagnetic field enhancement

In the last section it is shown that the dipole mode of a spherical nanoparticle can be excited efficiently at ω_{LSP}. In order to estimate the field enhancement offered by a metallic particle the analysis presented in [14] is briefly discussed. Only an isolated gold particle is considered. That means only the dipole mode can be coupled to the external EM radiation. Other high order modes cannot be excited due to their vanishing dipole moments [14].

The total field enhancement $|E_o|$ offered by a dipole mode normalized

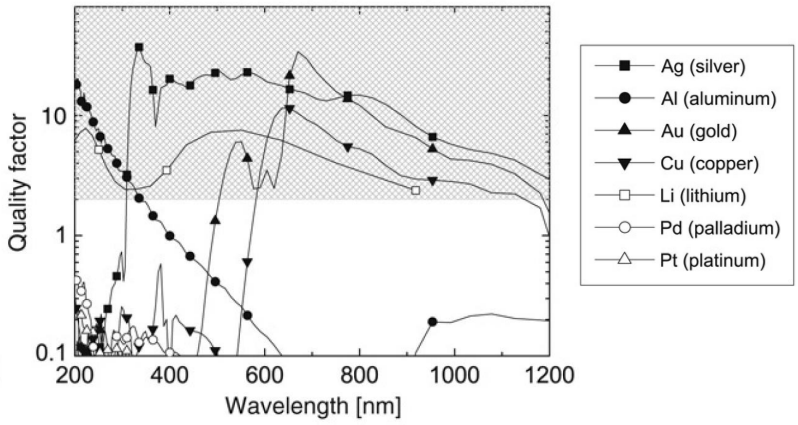

Figure 4.6: Quality factor of air-metal nanoparticles. The shaded area represents the area of interest for the sensing applications. Taken from [20].

to a electric field $|E_G|$ of a tightly confined Gaussian light beam is given by

$$\begin{aligned} F &= \frac{|E_o|}{|E_G|}\left(\frac{d}{d+x}\right)^3 \\ &= \frac{\sqrt{2}}{\sqrt{[Q^{-1}+2\chi_d^3/2\epsilon_m]^2+\delta^2}}\left(\frac{\chi_d}{\chi_d+\chi}\right)^3 \end{aligned} \tag{4.19}$$

where Q is the quality factor and given by Q=ω/γ,γ is the non-radiative decay rate, δ is normalized excitation detuning, χ and χ_d are the normalized radius and the distance from the sphere i.e. $\chi_d = 2\pi d/\lambda_d$. The gold nanoparticles have a Q in orders of 10 therefore offer a F $\approx$ 14. Quality factors of different air-metal nanoparticles are shown in Fig.‘4.6. In simple terms, Q is larger when γ hence Im(ϵ_M) is small. Gold and silver have a large quality factor in the NIR wavelength range. Silver oxidises quickly in ambient atmosphere so that gold is usually preferred for sensing applications. At visible wavelength, silver is by far the best plasmonic material. For UV plasmonics, aluminium has relatively higher Q value. Apart from these conventional noble metals, there exist other materials i.e. noble-transition alloys, alkali-noble inter-metallic compounds, doped semiconductors and 2-D materials. For a complete overview of the plasmonic properties of these materials, readers are directed to [21]. Also,

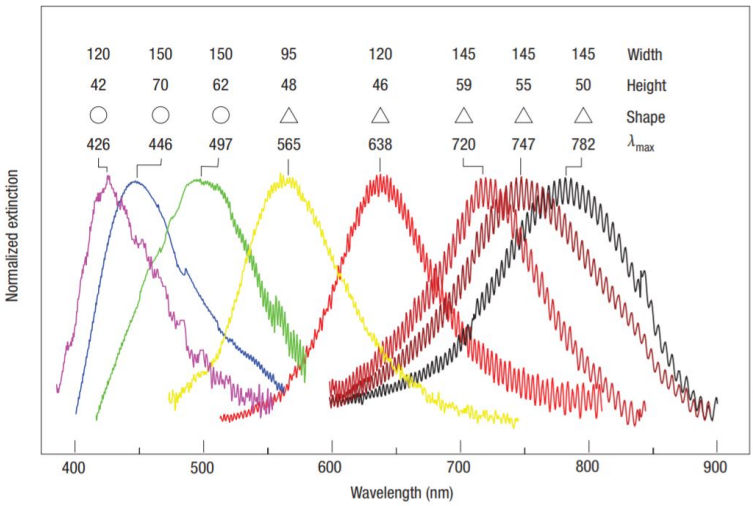

Figure 4.7: The geometrical dependence of the surface plasmon frequency for plasmonic rings and triangle. Taken from [22].

it is worth mentioning that the field enhancement F mentioned in Eq. 4.19, is strictly applicable to ultra small spherical geometries. For a large particle size, quasi-static approximation does not holds anymore. For large plasmonic structures and complex geometries, surface plasmon frequency ω_{SP} hence the field enhancement F, starts depending on the geometrical parameters [22]. As shown in Fig. 4.7, with increasing the lengths of plasmonic antennas two important mechanisms occur:

- Localized surface plasmon frequency gets red-shifted
- And FWHM increases

For more complex geometries, in general the enhancement factors have to be calculated numerically. Lumerical FDTD ($http://www.lumerical.com$) and Comsol Multiphysics ($https://www.comsol.com/$) are often used for this purpose.

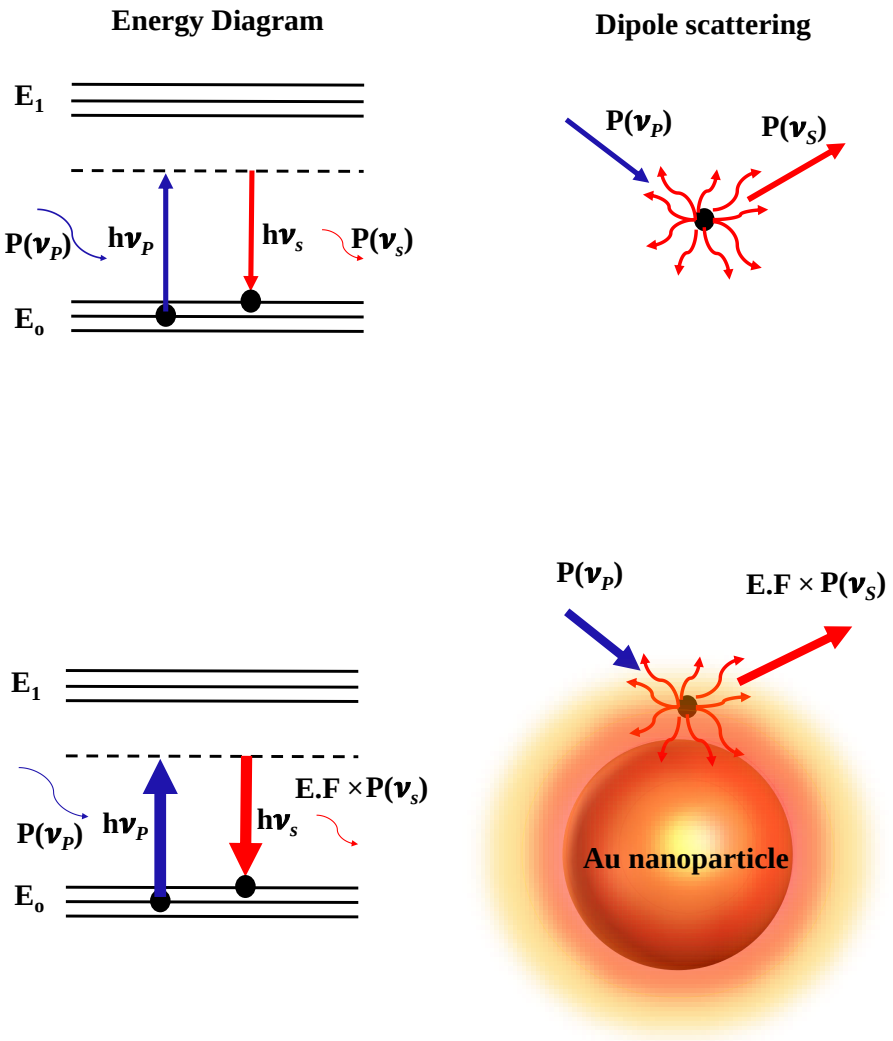

Figure 4.8: Description of spontaneous and surface enhanced Raman scattering. Spontaneous Raman signal (P_{ν_s}) is enhanced by the high field enhancement offered by the gold nanoparticle at pump ν_p as well as Stokes frequency ν_s.

4.3 Boosting Raman signal using field enhancement: Surface enhanced Raman spectroscopy

Due to the high field enhancement near a plasmonic structure, the weak Raman scattering can be enhanced by many folds. This phenomena is called surface enhanced Raman scattering (SERS). SERS is the most profound application of plasmonics known to date. Thanks to the high field enhancement, Raman scattering events of single molecules have been recorded using a roughened silver surface [23]. Just as a recap of Raman scattering phenomena presented in the introduction chapter, in the case of spontaneous Raman scattering, the molecules are excited to a higher vibrational states. This is depicted in Fig. 4.8. Depending on the initial state, the emitted photon can be red shifted (Stokes) or blue shifted (anti-Stokes). Unlike fluorescence spectroscopy, electron does not exhibit inelastic scattering in the higher energy state. Therefore, the Raman peaks are very well defined with a narrow line width. The Stokes power P_{ν_s} can be written as

$$P_s(\nu_s) = N\sigma_{RS} I(\nu_p) \tag{4.20}$$

where N is the number of scatterers within the excitation volume, σ_{RS} is the Raman cross section and I(ν_p) is the intensity of the excitation field at pump frequency ν_p. Typical value of Raman scattering cross sections lies between 10^{31} cm^2/molecule to 10^{28} cm^2/molecule, depending on whether the scattering is non-resonant or resonant. When the same molecule is brought next to a plasmonic structure e.g. an Au nanosphere as shown in Fig. 4.8, P_{ν_s} is enhanced due to two phenomena. Firstly, Raman cross section σ_{RS} is modified due to the electronic contribution [24]. This is called chemical enhancement. The chemical enhancement is relatively very moderate e.g. $\sigma_{SERS} \approx \sigma_{RS} \times 100$. [11]

Secondly, the enhanced electric field due to the excitation of localised surface plasmon (LSP), boosts the P_{ν_s} by many folds. This leads to the enhancement of both excitation as well as emitted light fields. The total enhanced Stokes power is given by

$$P_s(\nu_s) = EF \times N \times \sigma_{SERS} \times I(\nu_p) \tag{4.21}$$

where

$$EF = \left| \frac{E(\nu_p)}{E_o(\nu_p)} \right|^2 \times \left| \frac{E(\nu_s)}{E_o(\nu_s)} \right|^2 \tag{4.22}$$

Usually, the difference between pump and Stokes frequencies is quite small as compared to FWHM of the LSP i.e. ν_p=ν_s=ν , therefore, EF can be approximated as

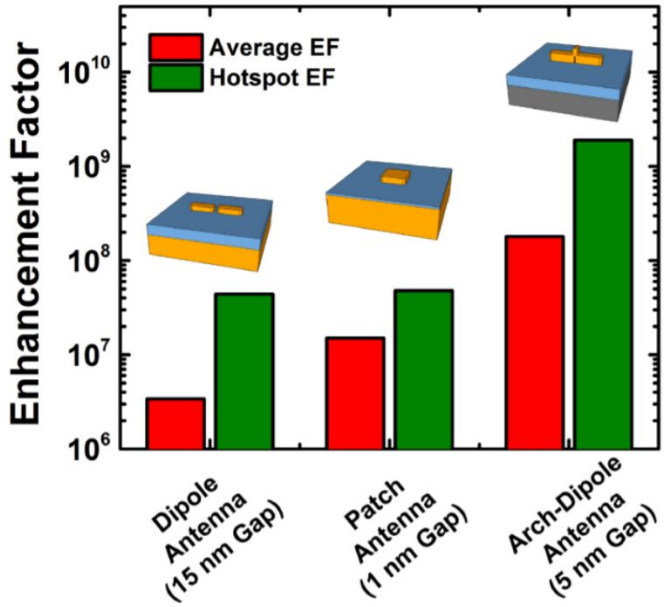

Figure 4.9: The hotspot (localized) and average enhancement factor of three different plasmonic structures. Taken from [25].

$$EF(\nu) = \left| \frac{E(\nu)}{E_o(\nu)} \right|^4 \tag{4.23}$$

Depending on the application, EF is reported at different positions around the plasmonic structure. For a single molecule detection, enhancement factor is reported at the maximum electric field point, this is called single molecule or hot spot enhancement factor (EF). Similarly, for a monolayer adsorbed on the surface of a plasmonic structure, an average EF is defined that takes an average of the enhanced field points all over the surface. The hot spot and average EF of several gap nanoplasmonic structures are depicted in Fig. 4.9.

4.3.1 SERS substrates

As discussed earlier, different plasmonic materials and structures have a specific wavelength of operation. Therefore, depending on the application, the right choice of a SERS substrate is essential for an efficient Raman spectroscopy. As a rule of thumb, the following properties need to be taken in account for a SERS substrate i.e. high SERS enhancement, good analyte

binding, long shelf-lives, controlled active sites to quantify the signal and relatively easy fabrication that leads to a reproducible SERS signal. In the early days of SERS exploration, SERS active substrates were either colloids of Au, Ag, or Cu or metallic foils/wires that had been chemically etched to create a roughened surface. Generally, SERS substrates are classified into three following categories: (1) metal nanoparticles in a suspension; (2) metal nanoparticles immobilized on solid substrates; and (3) nanostructures fabricated directly on solid substrates by nanolithography.

Suspension of the gold nanoparticles are prepared either by a mechanical process e.g. laser ablation of noble metals in liquid medium [26] or by using wet chemical methods e.g reducing silver or gold ions in a solution in the presence of a reducing agent [27]. On the other hand, immobilization of nanoparticles on a solid substrate provides a means by which to bring nanoparticles into close proximity to one another. Generally, a specific surface chemistry is applied on a secondary substrate, that allows the binding of gold nanoparticles with the substrate surface. For example, silanization on a quartz substrate is performed using (3-mercaptoppropyl)trimethoxysilane (MPTMS). The salinized quartz is then immersed into the suspension of metallic particles. Eventually, metallic particles bind with the quartz using trimethoxysilane moiety of MPTMS [28]. For a complete overview of these processes, readers are directed to the articles: [29, 30].

Highly ordered and well defined metallic structures are fabricated using lithography techniques. For example, nanosphere lithography (NSL) is an inexpensive, inherently parallel, high-throughput nanofabrication technique that can be used to produce well-ordered nanoparticles for SERS. Depending on the sequence of the steps involved in the process one can envision fabricating metal film over nanosphere (FON), periodic nanotriangle arrays, or nanovoid arrays [31, 32]. Similarly, custom design nanoantennas can be fabricated using electron beam lithography (EBL) where a a high resolution down to sub-10 nm is possible [33, 34]. This capability is important in the fabrication of SERS substrates due to the fact that the localized surface plasmons (LPS) responsible for the SERS effect greatly depend on the size, shape and arrangement of the nano-structure. However, direct writing EBL is a slow process thus hinders the mass scale fabrication. Also, there exist some other cheap lithography techniques that produce plasmonic platforms with nanometer-scale critical features e.g. nanoimprint lithography [35].

One of the most widely commercially available SERS substrates is Klarite. A Klarite substrate is comprised of an array of pyramidal shaped pits etched into silicon. The surface is then coated with a layer of gold to make it SERS-active [36]. This substrate has probably been the most char-

acterized of the substrates that have been prepared lithographically and used as a standard to compare the performance of new SERS substrates [30].

4.3.2 A monolayer as a SERS analyte

A monolayer is a single atom/molecule continuous sheet that adsorbed to a specific substrate. Monolayers of a material play a critical role in the modern instrumentation [37]. Many important physico-chemical reactions happen at the surface and interfaces, such as cell-membranes [38]. The study of monolayers at biointerfaces is crucial for applications ranging from clinical diagnostics and bio-materials to tissue engineering. Therefore, an optical technique that probes these reactions is essential. Furthermore 2-D materials [39, 40] like graphene and molybdenum disulfide, are thin sheets of atoms that usually deposited on a substrate using chemical vapour deposition (CVD) technique. Understanding CVD kinetics is important in controlling the electrical and optical properties of 2-D materials [41]. A non-destructive optical technique is essential to probe the quality of these single atom sheets. Similarly, in the monolayer research, there is a need for a precise tool that provides consolidated information about composition, molecular structure, and density of the surface molecules. Simultaneously characterizing the kinetics of the bio-chemical interactions at interfaces is equally important in many applications, such as the study of DNA hybridization [42, 43].

Due to the huge field intensity at the surface of a plasmonic structure, adsorbed molecule's monolayer is the best analyte to be detected using SERS. Most common monolayers that directly bind with the noble metals are alkane thiols and disulfides self assemble monolayers (SAM). Silane and thiols SAMs [44] are most common monolayers that binds to the gold. In next chapters, we will use 4-nitrothiophenol (NTP) monolayer to characterize the on-chip SERS sensors. NTP has a thiol group that selectively binds to the gold surface using sulphur-gold covalent bond [45].

4.4 Conclusion

To conclude, physical mechanisms underlying the field enhancement at the localized plasmon modes are presented. Depending on the wavelength of operation and nanoplasmonic structure size, there exist three kinds of surface plasmons i.e. i) propagating surface plasmon polaritons (PSPP), ii) bulk plasmons and iii) localized surface plasmons (LSP). Due to the resonant nature of LSP, a highly localized and enhanced field is excited at the

metal surface that leads to many fold electric field enhancement. This phenomena finds many applications, and one of the most profound application is surface enhanced Raman spectroscopy (SERS). Knowing the theory behind SERS and nanophotonics enhanced Raman spectroscopy (NWERS), we are introducing now our main work in which both SERS and NWERS are combined for an efficient on-chip Raman sensing. In the next chapter, we will present a novel approach in which nanoplasmonic antennas are integrated on a dielectric waveguide for an efficient on chip Raman sensing.

References

[1] Surbhi Lal, Stephan Link, and Naomi J Halas. *Nano-optics from sensing to waveguiding*. Nature photonics, 1(11):641, 2007.

[2] Argishti Melikyan, Luca Alloatti, Alban Muslija, David Hillerkuss, Philipp C Schindler, J Li, Robert Palmer, Dietmar Korn, Sascha Muehlbrandt, Dries Van Thourhout, et al. *High-speed plasmonic phase modulators*. Nature Photonics, 8(3):229, 2014.

[3] Neil W Ashcroft and N David Mermin. *Solid state physics*. 1976.

[4] JM Pitarke, VM Silkin, EV Chulkov, and PM Echenique. *Theory of surface plasmons and surface-plasmon polaritons*. Reports on progress in physics, 70(1):1, 2006.

[5] R. Dragila, B. Luther-Davies, and S. Vukovic. *High Transparency of Classically Opaque Metallic Films*. Phys. Rev. Lett., 55:1117–1120, Sep 1985.

[6] I Pockrand. *Coupling of surface plasma oscillations in thin periodically corrugated silver films*. Optics Communications, 13(3):311–313, 1975.

[7] Katherine A Willets and Richard P Van Duyne. *Localized surface plasmon resonance spectroscopy and sensing*. Annu. Rev. Phys. Chem., 58:267–297, 2007.

[8] Jiřı Homola, Sinclair S Yee, and Günter Gauglitz. *Surface plasmon resonance sensors*. Sensors and Actuators B: Chemical, 54(1-2):3–15, 1999.

[9] Christina Boozer, Gibum Kim, Shuxin Cong, HannWen Guan, and Timothy Londergan. *Looking towards label-free biomolecular interaction analysis in a high-throughput format: a review of new surface plasmon resonance technologies*. Current opinion in biotechnology, 17(4):400–405, 2006.

[10] Kathryn M Mayer and Jason H Hafner. *Localized surface plasmon resonance sensors*. Chemical reviews, 111(6):3828–3857, 2011.

[11] Stefan Alexander Maier. *Plasmonics: fundamentals and applications*. Springer Science & Business Media, 2007.

[12] Xuyen D Hoa, AG Kirk, and M Tabrizian. *Towards integrated and sensitive surface plasmon resonance biosensors: a review of recent progress*. Biosensors and bioelectronics, 23(2):151–160, 2007.

[13] John David Jackson. *Classical electrodynamics*, 1999.

[14] Greg Sun, Jacob B Khurgin, and Alexander Bratkovsky. *Coupled-mode theory of field enhancement in complex metal nanostructures*. Physical Review B, 84(4):045415, 2011.

[15] Eric W Weisstein. *Legendre polynomial*. 2002.

[16] Sabine Szunerits and Rabah Boukherroub. *Sensing using localised surface plasmon resonance sensors*. Chemical Communications, 48(72):8999–9010, 2012.

[17] Yi Xu, Ping Bai, Xiaodong Zhou, Yuriy Akimov, Ching Eng Png, Lay-Kee Ang, Wolfgang Knoll, and Lin Wu. *Optical Refractive Index Sensors with Plasmonic and Photonic Structures: Promising and Inconvenient Truth*. Advanced Optical Materials, 7(9):1801433, 2019.

[18] Huanjun Chen, Xiaoshan Kou, Zhi Yang, Weihai Ni, and Jianfang Wang. *Shape-and size-dependent refractive index sensitivity of gold nanoparticles*. Langmuir, 24(10):5233–5237, 2008.

[19] Wolfram Hergert and Thomas Wriedt. *The Mie theory: basics and applications*, volume 169. Springer, 2012.

[20] Eric Le Ru and Pablo Etchegoin. *Principles of Surface-Enhanced Raman Spectroscopy: and related plasmonic effects*. Elsevier, 2008.

[21] Paul R West, Satoshi Ishii, Gururaj V Naik, Naresh K Emani, Vladimir M Shalaev, and Alexandra Boltasseva. *Searching for better plasmonic materials*. Laser & Photonics Reviews, 4(6):795–808, 2010.

[22] Jeffrey N Anker, W Paige Hall, Olga Lyandres, Nilam C Shah, Jing Zhao, and Richard P Van Duyne. *Biosensing with plasmonic nanosensors*. In Nanoscience and Technology: A Collection of Reviews from Nature Journals, pages 308–319. World Scientific, 2010.

[23] Katrin Kneipp, Yang Wang, Harald Kneipp, Lev T Perelman, Irving Itzkan, Ramachandra R Dasari, and Michael S Feld. *Single molecule detection using surface-enhanced Raman scattering (SERS)*. Physical review letters, 78(9):1667, 1997.

[24] Katrin Kneipp. *Chemical contribution to SERS enhancement: an experimental study on a series of polymethine dyes on silver nanoaggregates*. The Journal of Physical Chemistry C, 120(37):21076–21081, 2016.

[25] Tae Joon Seok, Arash Jamshidi, Michael Eggleston, and Ming C Wu. *Mass-producible and efficient optical antennas with CMOS-fabricated nanometer-scale gap*. Optics Express, 21(14):16561–16569, 2013.

[26] John Neddersen, George Chumanov, and Therese M Cotton. *Laser ablation of metals: a new method for preparing SERS active colloids*. Applied Spectroscopy, 47(12):1959–1964, 1993.

[27] Rares Stiufiuc, Cristian Iacovita, Constantin M Lucaciu, Gabriela Stiufiuc, Alina G Dutu, Cristiana Braescu, and Nicolae Leopold. *SERS-active silver colloids prepared by reduction of silver nitrate with short-chain polyethylene glycol*. Nanoscale research letters, 8(1):47, 2013.

[28] Olivier Péron, Emmanuel Rinnert, Michel Lehaitre, Philippe Crassous, and Chantal Compère. *Detection of polycyclic aromatic hydrocarbon (PAH) compounds in artificial sea-water using surface-enhanced Raman scattering (SERS)*. Talanta, 79(2):199–204, 2009.

[29] Pamela Mosier-Boss. *Review of SERS substrates for chemical sensing*. Nanomaterials, 7(6):142, 2017.

[30] Xin Sun and Hao Li. *A Review: Nanofabrication of surface-enhanced Raman spectroscopy (SERS) substrates*. Current Nanoscience, 12(2):175–183, 2016.

[31] De-Yin Wu, Jian-Feng Li, Bin Ren, and Zhong-Qun Tian. *Electrochemical surface-enhanced Raman spectroscopy of nanostructures*. Chemical Society Reviews, 37(5):1025–1041, 2008.

[32] Pieter C Wuytens, Ananth Z Subramanian, Winnok H De Vos, Andre G Skirtach, and Roel Baets. *Gold nanodome-patterned microchips for intracellular surface-enhanced Raman spectroscopy*. Analyst, 140(24):8080–8087, 2015.

[33] Nahla A Abu Hatab, Jenny M Oran, and Michael J Sepaniak. *Surface-enhanced Raman spectroscopy substrates created via electron beam lithography and nanotransfer printing*. ACS nano, 2(2):377–385, 2008.

[34] Weisheng Yue, Zhihong Wang, Yang Yang, Longqing Chen, Ahad Syed, Kimchong Wong, and Xianbin Wang. *Electron-beam lithography of gold nanostructures for surface-enhanced Raman scattering*. Journal of Micromechanics and Microengineering, 22(12):125007, 2012.

[35] Steven J Barcelo, Wei Wu, Xuema Li, Zhiyong Li, and R Stanley Williams. *Nanoimprint lithography of plasmonic platforms for SERS applications*. Applied Physics A, 121(2):443–449, 2015.

[36] Karen Faulds, Aaron Hernandez-Santana, and W. Ewen Smith. *The inorganic chemistry of surface enhanced Raman scattering (SERS)*. In Spectroscopic Properties of Inorganic and Organometallic Compounds: Techniques, Materials and Applications, Volume 41, volume 41, pages 1–21. The Royal Society of Chemistry, 2010.

[37] Abraham Ulman. *An Introduction to Ultrathin Organic Films: From Langmuir–Blodgett to Self–Assembly*. Academic press, 2013.

[38] Dennis Chapman. *Biomembrane structure and function*. Springer, 1983.

[39] Mingsheng Xu, Tao Liang, Minmin Shi, and Hongzheng Chen. *Graphene-like two-dimensional materials*. Chemical reviews, 113(5):3766–3798, 2013.

[40] Zhenhua Sun and Haixin Chang. *Graphene and graphene-like two-dimensional materials in photodetection: mechanisms and methodology*. ACS nano, 8(5):4133–4156, 2014.

[41] Maria Losurdo, Maria Michela Giangregorio, Pio Capezzuto, and Giovanni Bruno. *Graphene CVD growth on copper and nickel: role of hydrogen in kinetics and structure*. Physical Chemistry Chemical Physics, 13(46):20836–20843, 2011.

[42] Edwin Southern, Kalim Mir, and Mikhail Shchepinov. *Molecular interactions on microarrays*. Nature genetics, 21(1s):5, 1999.

[43] Nirmalya K Chaki and K Vijayamohanan. *Self-assembled monolayers as a tunable platform for biosensor applications*. Biosensors and Bioelectronics, 17(1-2):1–12, 2002.

[44] Colin D Bain, E Barry Troughton, Yu Tai Tao, Joseph Evall, George M Whitesides, and Ralph G Nuzzo. *Formation of monolayer films by*

the spontaneous assembly of organic thiols from solution onto gold. Journal of the American Chemical Society, 111(1):321–335, 1989.

[45] J. Christopher Love, Lara A. Estroff, Jennah K. Kriebel, Ralph G. Nuzzo, and George M. Whitesides. *Self-Assembled Monolayers of Thiolates on Metals as a Form of Nanotechnology*. Chemical Reviews, 105(4):1103–1170, 2005. PMID: 15826011.

5

SERS using waveguide excited plasmonic antenna

The integration of sub-wavelength size nanoplasmonic structures with photonic platforms has received a considerable interest in the past few years. A hybrid plasmonic-photonic approach reunites the best of two worlds: on one side, the extreme optical properties of plasmonic nanostructures enable a variety optical functionalities (sensing [1], modulation [2], non-linear processing) at low power and in sub-micron footprints and on the other side, the possibility of massive fabrication of photonic integrated circuits. Furthermore, the ability of plasmonics to manipulate the light at a level below the diffraction limit makes it an excellent platform for surface enhanced Raman spectroscopy. Plasmonic antennas integrated on a dielectric waveguide can be excited efficiently using the evanescent field of a waveguide mode [3–6]. The concentrated light spots so called hot spots at plasmonic resonance can lead to many fold enhancement of the Raman scattering.

In chapter 3, we analyzed the nanophotonics waveguide enhanced Raman spectroscopy (NWERS) using a dielectric waveguide where the major Raman enhancement comes from two phenomena: enhanced spontaneous emission due to a high index contrast waveguide and few centimeters long light-analyte interaction. NWERS has shown considerable potential in many sensing applications comprising of analytes in different phases i.e. in bulk and gases. However, for ultra small analytes i.e. monolayers, further signal enhancement is needed. In the previous chapter, we ana-

lyze the SERS enhancement offered by a gold nanophere where the Raman signal can be enhanced many folds. Here, we introduce an other on-chip Raman modality that combines both techniques i.e the integration of nanoplasmonic antennas on a high index contrast waveguide. Dr. Peyskens (graduated, 2015, PRG, Ghent University) for the first time demonstrated on-chip surface enhanced Raman spectroscopy using an integrated antenna array on a single mode PECVD $\mathrm{Si_3N_4}$ waveguide.

In this chapter we present the analytical formalism of SERS using integrated nanoplasmonc antennas (developed before by Dr. Peyskens). The SERS performance of plamonic antennas i.e. arch dipole and nanobowties is presented and compared. The effect of the Raman background generated by a dielectric waveguide on a SERS signal of a nanobowtie antenna is also presented. Using the back reflection configuration and short access waveguide length, SERS for a monolayer using a single integrated antenna is demonstrated. In the end, we compare the SERS performance of an antenna sitting on the waveguide with an antenna embedded into the waveguide.

5.1 Analytical on chip SERS model

Localized surface plasmon (LSP) of a plasmonic antenna can be excited in a relatively simple configuration. One way to excite LSP is by integrating nanoantennas on a dielectric waveguide where the evanescent field of a waveguide mode couples to the antenna. This interaction is normally quantified as an interaction efficiency of a plasmonic antenna [7].

A schematic of the plasmonic antennas integrated on a $\mathrm{Si_3N_4}$ waveguide is shown in Fig. 5.1. Let's assume the total number of antennas is N. The access waveguide length before the array of antennae is L_a. And the access waveguide after antenna array is L_a. Each antenna is separated by a fix distance d, long enough to avoid the coupling between antennas. The total waveguide length in this case is L=2L_a+(N-1)d. In the absence of nanoantennas, the Raman conversion efficiency η (as defined in Chapter. 3) is given as

$$\eta(\mathrm{w},\mathrm{h},\lambda_p,\lambda_s) = \frac{n_g^2\lambda_s^2}{n}\iint \frac{\epsilon|\mathbf{E^m}(\mathbf{r},\lambda_\mathbf{p})|^\mathbf{2}}{\iint \epsilon|\mathbf{E^m}(\mathbf{r},\lambda_\mathbf{p})|^\mathbf{2}\mathrm{d}\mathbf{r}}\frac{1}{\mathbf{A_{eff}}(\mathbf{r},\lambda_\mathbf{s})}\mathrm{d}\mathbf{r} \quad (5.1)$$

where the effective modal area can be written as

$$A_{eff} = \frac{\iint\left(2\epsilon_o\epsilon(\mathbf{r},\lambda_\mathbf{s})\mathbf{E^m}(\mathbf{r},\lambda_\mathbf{s})|^\mathbf{2}\right)\mathrm{d}\mathbf{r}}{\epsilon_o\epsilon(\mathbf{r},\lambda_\mathbf{s})|\mathbf{E^m}(\mathbf{r},\lambda_\mathbf{s})|^\mathbf{2}} \quad (5.2)$$

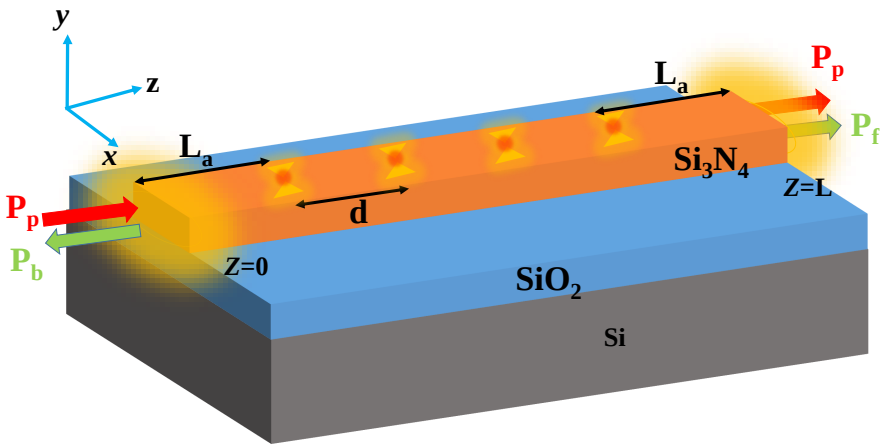

Figure 5.1: The schematic of plasmonic antennas integrated on a Si_3N_4 waveguide. The total length of the waveguide is L=2L_a+(N-1)d, where n = total number of antennas.P_b and P_f are the backward and forward scattered Stokes light.

Both η and A_{eff} solely depends on the modal field and can be computed at z=0 (at the input facet). When a plasmonic antenna is integrated on a waveguide, the field at a position r_o is enhanced by a factor EF i.e

$$\mathbf{EF}((\lambda_\mathbf{i}, \mathbf{r_o})) = \left| \frac{\mathbf{E^a}(\lambda_\mathbf{i}, \mathbf{r_o})}{\mathbf{E^m}(\lambda_\mathbf{i}, \mathbf{r_o})} \right| \tag{5.3}$$

where E^a is the enhanced field at a position r_o around the plasmonic antenna. As discussed in the previous chapter, EF depends on the shape and the size of a plasmonic antenna. For a gold bowtie antenna at 785 nm wavelength, $|EF|^4$ is 1.14×10^4 [8]. Using Eq. (5.1), (5.2) and (5.3), the single antenna conversion efficiency assuming an analyte of thickness t_a can be defined as

$$\eta_A(\mathrm{w}, \mathrm{h}, \lambda_p, \lambda_s) = \frac{n_g^2 \lambda_s^2}{n t_a} \iiint_V \frac{\epsilon |\mathbf{E^m}(\mathbf{r}, \lambda_\mathbf{p})|^\mathbf{2}}{\iint \epsilon |\mathbf{E^m}(\mathbf{r}, \lambda_\mathbf{p})|^\mathbf{2} \mathrm{d}\mathbf{r}} \times \frac{EF(\mathbf{r}, \lambda_\mathbf{p})^\mathbf{2} \mathbf{EF}(\mathbf{r}, \lambda_\mathbf{s})^\mathbf{2}}{\mathbf{A_{eff}}(\mathbf{r}, \lambda_\mathbf{s})} \mathrm{d}\mathbf{r} \tag{5.4}$$

where the external integral runs over the volume of an analyte. In the next section, we will present the Lumerical 3D-FDTD Solutions based model to compute the η_A for a monolayer of 4-Nitrothiophenol (NTP).

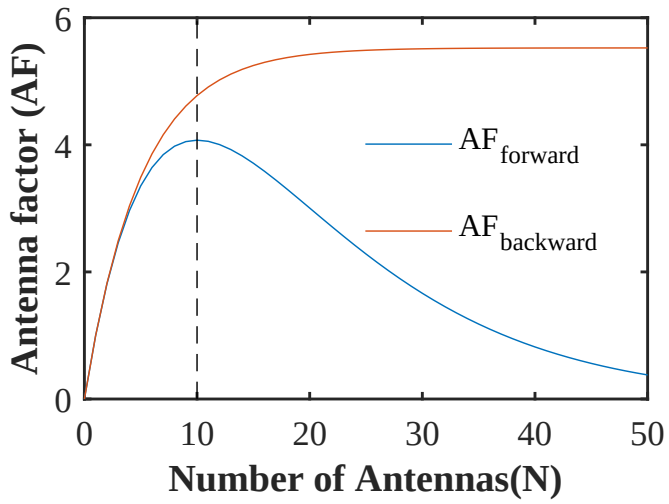

Figure 5.2: The antenna factor for a forward $AF_{forward}$ and back scattered $AF_{backward}$ Stokes signal. The dotted line represents the N_{opt}. $AF_{forward}$ decreases for the N >N_{opt}. On the other hand, $AF_{backward}$ saturates for $N \to \infty$. e_p and e_s used in these calculation are 0.45 and 0.41 respectively.

For the case of an array of nano-antennas, the extinction of the pump power and subsequently of the Stokes signal need to be taken in account. In Chapter 3, for the nanophotonic waveguide enhanced Raman signal (NWERS), a length factor is defined that takes in account the pump and Stokes power decay due to the waveguide losses. In a similar manner, a so called antenna factor AF can be defined for a forward as well as a back scattered Stokes signal. For a forward scattering configuration, the total Stokes power collected at the output facet of the waveguide is given as [8]

$$\frac{P_f(\lambda_s)}{P_p(\lambda_p)} = \rho\sigma\eta_A e^{-\alpha_w(2L_a+(N-1)d)} \overbrace{e_s^{1-N}\left(\frac{1-(\frac{e_s}{e_p})^N}{1-(\frac{e_s}{e_p})}\right)}^{\mathrm{AF}_{forward}} \tag{5.5}$$

where P_p is the pump power at the input facet. α_w is the waveguide loss. ρ and σ are the molecular density and Raman cross section of the analyte molecule. e_p and e_s are the extinctions at pump and Stokes wavelength respectively, and defined as

$$e_i[dB] = T_{ref}(\lambda_i)[dB] - T_{ant}(\lambda_i)[dB] \tag{5.6}$$

where T_{ref} and T_{ant} are the transmission in a reference and a functionalised waveguide. Due to the decay of the pump light, there exists an optimized number of antennas N_{opt} i.e. P_f starts to decay for n>N_{opt}. Using $\frac{dAF_{forward}}{dN}$ =0, N_{opt} can be calculated i.e.

$$N_{opt} = \frac{log\left(\frac{log(e_s)}{log(e_p)}\right)}{log\left(\frac{e_s}{e_p}\right)} \tag{5.7}$$

In a similar manner, the total back scattered Stokes power P_b collected at the input facet can also be defined [9]

$$\frac{P_b(\lambda_s)}{P_p(\lambda_p)} = \rho\sigma\eta_A e^{-\alpha(2L_a+(N-1)d)} \overbrace{\left(\frac{1-(\frac{1}{e_p e_s})^N}{1-(\frac{1}{e_p e_s})}\right)}^{\mathrm{AF}_{backward}} \tag{5.8}$$

Both $AF_{forward}$ and $AF_{backward}$ are plotted in Fig. 5.2. $AF_{forward}$ increases with number of antennas and then starts to decrease for N >N_{opt}. Contrary to the forward scattering, the back scattered signal has no optimum antenna number, but saturates for N $\rightarrow \infty$.

5.1.1 Lumerical Model

Lumerical 3D-FDTD Solutions is used to calculate the single antenna conversion efficiency η_A. We consider two antenna geometries i.e. bowtie (BT) [8] and arch dipole (AD) antenna [10, 11]. The schematic of both antennas is shown in Fig. 5.3(a). For the realization of experimental conditions, we used a refractive index value of 1.9 for the PECVD Si_3N_4 (width = 700 nm and height h = 220 nm), 1.45 for the SiO_2 under cladding and 1 for the top cladding (air). The metal stack thicknesses are fixed to 2 nm for the Ti adhesion layer (AL) and 30 nm for the Au. Built-in refractive index models for Au (Johnson and Christy29) and Ti (CRC30) are used. An additional surface layer of thickness t_a = 1 nm and index n_{NTP} = 1.62 [12] are used to model a 4-nitrothiophenol (NTP) monolayer. We used ultra-refined mesh (0.5 - 1 nm) in the antenna region (including the Ti adhesion layer and the NTP monolayer). The surface density value used for NTP is ρ = 5.56 $\times$ 10^{18} molecules/m^2. The Raman cross-section is σ = 1.38$\times$ 10^{-29} cm^2 /sr for 1340 cm^{-1} Raman line. To extract the local electric field from desired

region, a field monitor is used. In all simulation results, a fundamental TE mode of Si_3N_4 waveguide is used to excite the dipole mode of antennas. Finally, the integral in the numerator of Eq. 5.4 is calculated by integrating the electric field in a volume containing the NTP. While the integral in the denominator is computed by integrating the modal electric field points extracted from an un-functionalized waveguide. In all simulations, 785 nm and 877 nm (the Raman resonance of 1339 cm^{-1} ($\nu_s(NO_2)$)) are taken as the pump wavelength and Stokes wavelength.

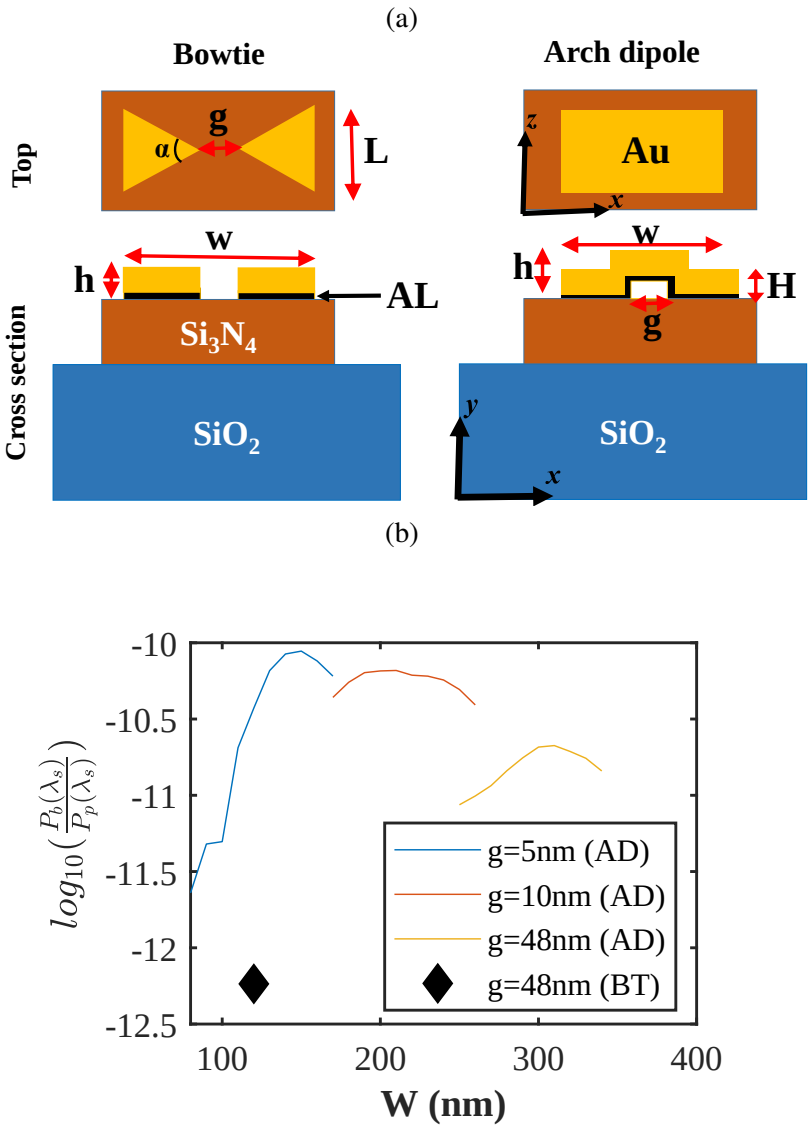

Figure 5.3: a) Schematics of a bowtie (BT) and an arch dipole (AD) antenna. b) $\frac{P_b(\lambda_s=877nm)}{P_p(\lambda_p=785nm)}$ of AD antenna as a function of gap g and width W. The other design parameters are L = 50 nm, h = 40 nm and H = 20 nm (no adhesion layer). Black diamond represents a bowtie (BT) antenna with the following geometry: α = 60 °, W = 100 nm, g = 48 nm and L = 120 nm. In both cases, an access length L_a=100 μm and a waveguide loss α = 3.2 dB/cm are assumed.

5.1.2 η_A for an arch dipole and a bowtie antenna

For the bowtie antenna we assume the following geometry i.e. α = 60 °, W = 100 nm, g = 48 nm and L = 120 nm. This corresponds to the localized plasmon resonance wavelength λ_{LSP} = 830 nm. The pump and Stokes extinctions without any adhesion layer are e_p=0.8 dB, and e_s=0.75 dB that corresponds to N_{opt} = 9. The integration of bowtie antenna on a Si_3N_4 strip waveguide is a key result of the PhD work of Frederic Peyskens [7–9]. All these parameters are extracted from the previous work [8]. $\frac{P_f(\lambda_s=877nm)}{P_p(\lambda_p=785nm)}$ for the given bowtie geometry is 5.8 $\times$ 10^{-13} [9].

For an arch dipole antenna, simulations are performed for three different gaps(g) i.e 5 nm, 10 nm and 48 nm. For each gap, the width of the antenna is swept in order to tune the localized plasmon resonance wavelength near the Stokes wavelength(λ_S = 877nm). Other design parameters of the antenna are: L=50 nm, h=40 nm and H= 20 nm. The ratio $\frac{P_f(\lambda_s=877nm)}{P_p(\lambda_p=785nm)}$ is plotted in Fig. 5.3(b). As expected, $\frac{P_f(\lambda_s=877nm)}{P_p(\lambda_p=785nm)}$ increases when the gap decreases e.g. for g=5 nm $\frac{P_f(\lambda_s=877nm)}{P_p(\lambda_p=785nm)}$ = 8.82 $\times$ 10^{-11}, that is 1.35 and 4.18 times greater as compared to g=10 nm and g=48 nm. $|EF|^4$ calculated at the middle of the gap is given as $|EF_{g=48nm}|^4$ = 7.6 $\times$ 10^5 and $|EF_{g=5nm}|^4$ = 1.1 $\times$ 10^7. In contrary to localized field enhancement factor $|EF|^4$, $\frac{P_f(\lambda_s=877nm)}{P_p(\lambda_p=785nm)}$ increases moderately from 48 to 5 nm gap. Also, increasing the gap blue shifts λ_{LSP}, therefore, w needs to be increased in order to compensate this frequency change. This trends hold as far as the gap mode is excited. For example in the case of bowtie antenna, λ_{LSP} first blue-shifts with increasing gap, and then red-shifts as the individual triangles become more and more uncoupled [13]. Figure. 5.4 shows the extinction of a 48 nm gap arch dipole antenna. λ_{LSP} shifts to higher wavelength when W increases from 270 to 330 nm. It is worth mentioning that the introduction of an adhesion layer e.g. Ti or Cr increases the extinction hence decrease the $\frac{P_f(\lambda_s=877nm)}{P_p(\lambda_p=785nm)}$. However, this can be avoided by using a polymer adhesion layer e.g. MPTS 3-Mercaptopropyltrimethoxysilane [14]. In [6], it is shown that a 3-fold increase of the collected signal using nanoplasmonic antennas integrated on a nanophotonic waveguide can be achieved by replacing the Ti adhesion layer with MPTS. Likewise, as we will discuss latter, the collected signal can also be enhanced by embedding an antenna into the waveguide.

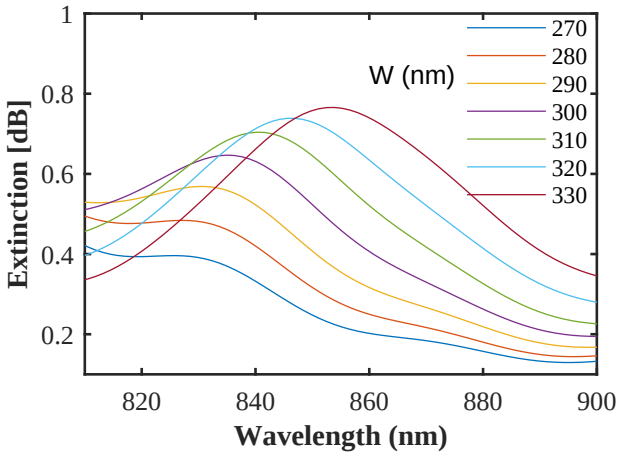

Figure 5.4: The extinction of an arch dipole antenna of the following geometry: g = 48 nm, L = 50 nm, h = 40 nm, H = 20 nm and W = 270 to 330 nm with an offset of 10 nm.

5.2 Effect of the access waveguide Raman background on the SERS signal

In Chapter 3, we discussed the Raman background generated from the dielectric waveguide and its impact on the analyte Raman signal. In order to excite the dipole mode of an antenna, the waveguide mode needs to be fundamental TE (E should be along the x-axis as shown in the Fig. 5.3(a)). Due to a significant overlap of fundamental TE mode with the waveguide core, a large Raman background is generated that is collected along with the SERS signal. For a waveguide of length L, the total back-scattered signal collected at the waveguide facet is given by

$$\frac{P_{bg}}{P_p(\lambda_p)} = \frac{1}{2} \times \rho_{Si_3N_4} \times \sigma_{Si_3N_4} \times \eta_{wg}(\mathrm{w}, \mathrm{h}, \lambda_p, \lambda_s) \times \left(\frac{1 - e^{-(\alpha_p + \alpha_s)L}}{\alpha_\mathrm{p} + \alpha_\mathrm{s}} \right) \tag{5.9}$$

where $\rho_{Si_3N_4}$, $\sigma_{Si_3N_4}$ and η_{wg} are Si_3N_4 molecular density, Raman cross section and background conversion efficiency. α_p and α_s are the waveguide losses at the pump and Stokes wavelength. Note that this is the same equation as defined in Chapter. 3 (Eq. 3.6). Here, we have replaced η_A

with η_{wg} to avoid the confusion between single antenna conversion efficiency and background conversion efficiency. At 877 nm (1340 cm^{-1}), $\frac{\rho_{SiN} \times \sigma_{SiN} \times \eta_{wg}}{2(\alpha_p + \alpha_s)}$ = 4.69 $\times$ 10^{-10} [15] for a waveguide loss $\alpha_p = \alpha_s = \alpha$ =3.2 dB/cm.

Assuming a configuration, in which single antenna is integrated on a waveguide, the total back scattered signal collected at the waveguide facet is given by

$$\frac{P_{bg}}{P_p(\lambda_p)} = \frac{1}{2} \times \rho \times \sigma \times \eta_{wg}(\mathrm{w}, \mathrm{h}, \lambda_p, \lambda_s) \times \left(\frac{1 - e^{-(\alpha_p + \alpha_s)L_a}}{\alpha_\mathrm{p} + \alpha_\mathrm{s}} + (e_p e_s)^{-1} e^{-\alpha_s L_a} \frac{1 - e^{-(\alpha_p + \alpha_s)L_b}}{\alpha_\mathrm{p} + \alpha_\mathrm{s}} \right) \tag{5.10}$$

where L_a is the length between the input facet and the antenna while L_b is the waveguide length between the antenna and the output facet. For a smaller L_b i.e. $\mathrm{L}_b << \mathrm{L}_a$, the second term in Eq. 5.10 disappears and eventually converges back to Eq. 5.9. Note that in Eq. 5.10, the minimal background generated due to the back reflected pump beam from antenna and the output facet is ignored.

In order to analyze the signal-to-noise ratio, an analytical formula is derived that incorporates the back-scattered signal generated by an antenna and the background associated with the PECVD Si_3N_4. The signal to noise ratio is computed using Eq. 5.8 and Eq. 5.10 and given as

$$SNR = \sqrt{C_{exp}} \times \frac{P_{bg}}{\sqrt{P_b + P_{bg}}} \tag{5.11}$$

here we introduced a factor that depends on the experimental conditions i.e. pump power, integration time, coupling losses and spectrometer losses (grating transmission, input slit loss, photons to counts ratio etc. (See Appendix B).

A 2-D chart showing the SNR (in $\log_{10}$ scale) for different waveguide background conversion efficiencies η_{wg} and antenna conversion efficiencies η_A is presented in Fig. 5.5. A 0.5 mm long access waveguide is assumed in all the cases. The area in white color in the bottom of the chart represents the SNR < 1. In Fig. 5.5, two horizontal lines i.e. magenta and green represent the SERS signal strength of an NTP coated optimized bowtie and arch dipole antenna, respectively. The vertical red line represents the background strength of a single mode PECVD Si_3N_4 waveguide (width=700 nm, height=220 nm). Due to the high SERS signal strength, an optimized

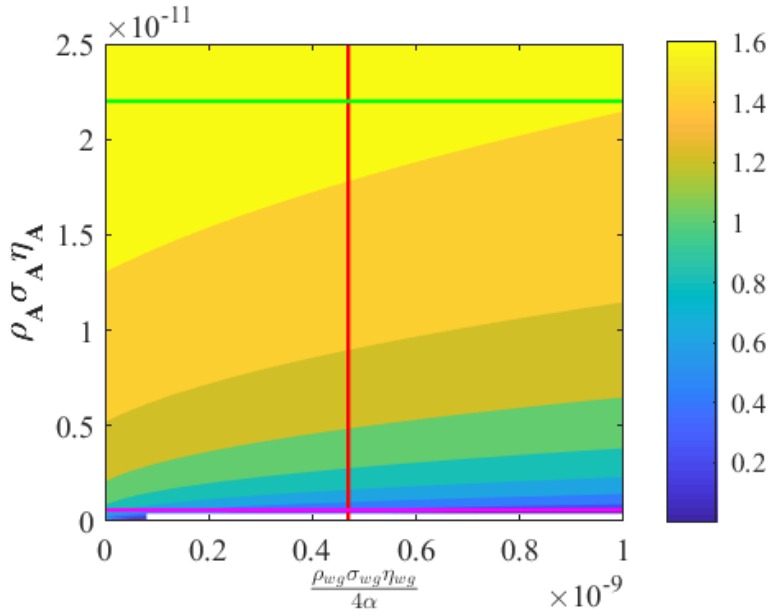

Figure 5.5: Signal-to-noise ratio i.e. $SNR = \sqrt{C_{exp}} \times \frac{P_{bg}}{\sqrt{P_b + P_{bg}}}$ *(in log scale) for the SERS signal generated from a monolayer deposited on an antenna integrated on a waveguide. The red vertical line represents a single mode PECVD* Si_3N_4 *waveguide. The magenta and green horizontal lines represent an optimized NTP coated gold bowtie and an AD antenna integrated on* Si_3N_4 *waveguide.*

arch dipole antenna offers 25 times higher signal to noise ratio as compared to a bowtie antenna for a same gap of 48 nm. In the next section, we will introduce experimental results and verify this SNR model. The bowtie antenna geometry provides moderate field enhancement but is relatively easy to fabricate. On the other hand the AD antenna provides huge EM enhancement but more challenging to fabricate. Therefore, due to the relatively difficult fabrication of an arch-dipole antenna, we have limited our experimental discussion to a bowtie antenna integrated on a single mode PECVD Si_3N_4 waveguide. To get an overview of the fabrication of an arch dipole antenna readers are directed to [10].

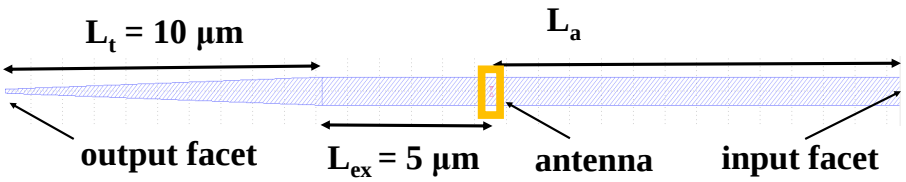

Figure 5.6: The schematic (Graphic Database System image) of a single plasmonic antenna integrated on a single mode Si_3N_4 waveguide. A taper of length L_t = 10 μm is introduced at the end of the waveguide to avoid any back reflection of the pump light at the output facet.

5.2.1 Experimental results of a single plasmonic antenna integrated on a Si_3N_4 waveguide

To do the experimental analysis, a single plasmonic bowtie antenna is integrated on a single mode Si_3N_4 waveguide. The schematic of the device is shown in Fig. 5.6. Each waveguide is terminated using a 5 μm extension length followed by a 10 μm long linear taper to avoid any back reflection of the pump light at the output facet. The fabrication of this device is discussed below.

5.2.1.1 Fabrication of the device

In order to demonstrate the SERS using a single antenna integrated on a Si_3N_4 waveguide, electron beam lithography (EBL) is used to achieve an antenna gap of sub 50 nm [9]. The device is fabricated mainly in two direct writing EBL steps: the fabrication of nanoantennas and the patterning of a Si_3N_4 waveguide. The whole fabrication process is depicted in Fig. 5.7.

The starting dielectric wafer is a PECVD Si_3N_4/SiO_2/Si (220 nm / 2.4μm / 750μm) purchased from the imec foundry ($https://www.imec-int.com$). The Si_3N_4 is deposited on top of a 2.3 μm silicon dioxide film via PECVD at a low temperature [16]. First of all 1 cm^2 dielectric chips are diced from a wafer and thoroughly clean in an ultrasonic acetone bath for 15 minutes. Subsequently, the samples are rinsed with acetone and isopropyl alcohol (IPA) and dried with an N_2 gun.

In the first EBL step, the gold nanoantennas and alignment markers are patterned in a photoresist layer of PMMA 950K (3% chlorobenzene). This PMMA layer is spin coated on the dielectric slab using 6000 RPM for 1 minute spin time resulting in an average resist thickness of 70 nm. This

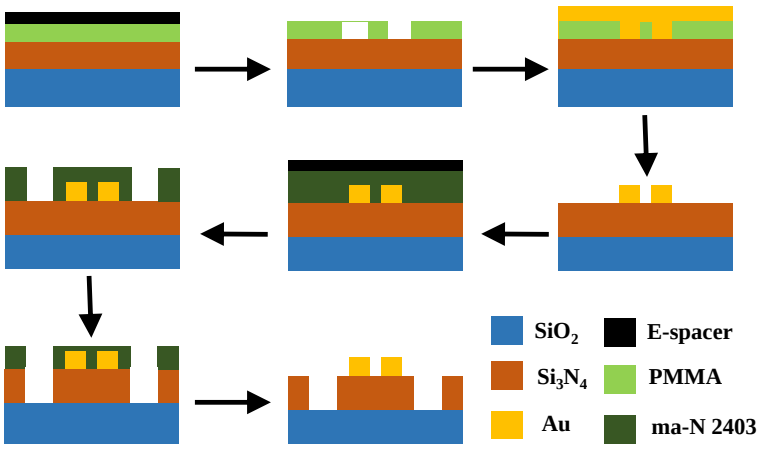

Figure 5.7: The fabrication process of a bowtie antenna integrated on a PECVD Si_3N_4 *strip waveguide.*

resist thickness enables the lifting off a 30 nm thick gold. After the resist coating, the sample is baked at 165° C for 30 mins inside a convection oven. To avoid any charging effect, a thin layer of E-space 3000Z is spin coated over the resist at 1500 RPM for 70 sec spin time followed by a 10 min long bake at 95°C temperature. Then the sample is exposed using a 2 nm grid with a 280 μmC dose. After the exposure, the sample is dipped into the DI water for 1 min to remove E-space 3000Z. A 50% diluted Methyl iso-butyl ketone (MIBK) in ethanol (1:1) is used for the development of the resist. Before development, the solution is put on a temperature stabilizer for 1 hour at 21°C. The sample is then immersed in this thermally stable solution for 1 minute and is subsequently rinsed with IPA for about 30 seconds and dried with an N_2 gun. After development a short O_2 plasma (1 min) is applied to purify the surface because small remainders of PMMA can have a detrimental impact on the adhesion between the Si_3N_4 and the metal stack. Ti/Au stack (with 2 nm/30 nm thickness) is sputtered with a low power recipe in a commercial Pfeiffer Spider 630. A low power leads to a controlled metal layer thickness and small grain sizes hence low surface roughness. The first Ti layer serves as an adhesion layer between the Si_3N_4 and the gold. Finally, the sample is immersed in acetone for metal lift-off. The whole metal lift off process takes about 1 hour. And the beaker with fresh acetone is replaced thrice during this time to avoid the sedimentation of undesired metal flakes on the sample.

In a second EBL step, Si_3N_4 waveguides (underneath the metal nanoantennas) along with the position and cleaving markers are defined. A negative e-beam resist (ma-N 2403) is used in combination with a 10 nm grid exposure to define the 700 nm wide Si_3N_4 waveguides (single mode at 785 nm wavelength). A 300 nm ma-N 240 thick resist is spin coated using 2000 RPM and 30 sec spin time. Then the sample is baked at 110°C for 30 min. Again, a thin E spacer layer is spun on top of the ma-N 2403 to counteract the charging and followed by a 10 min long bake at 95°C. After E spacer removal, the sample is dried with N_2 before the resist is developed in ma-D 525 developer for 150 seconds. During development, the sample is gently stirred every 30 seconds. A 120 seconds immersion in a DI overflow bath eventually stops the development. The sample is then etched in a commercial ICP plasma etcher (Oxford Plasmalab 100), using a mixture of 90 sccm C_4F_8 and 30 sccm SF_6. In the end, mr-Rem 400 resist remover is used to completely remove the organic residual on the chip.

The optical microscope image along with the scanning electron microscope (SEM) images of the chip is shown in the Fig. 5.8. The position marker is used to spot the single antenna from the optical microscope. The final gap g $\approx$ 38 nm is achieved. Due to the misalignment (possibly due to the stage drift), the center of the bowtie antenna is misplaced by 174 $\pm$ 3 nm from the center of the waveguide. However, numerical simulations indicates that this misalignment should not drastically affect the antenna conversion efficiency i.e. $\frac{P_f(\lambda_s=877nm)}{P_p(\lambda_p=785nm)}$ for the given misalignment is 2.1 $\times$ 10^{-13}.

5.2.1.2 4-Nitrothiophenol (NTP) coating

Due to the selective binding with the gold, low absorption in NIR wavelength range, easy access and high Raman cross section, 4-Nitrothiophenol (NTP) is used as an analyte to characterize the SERS sensor. We use a standard binding recipe, e.g. chemisorption of thiols from an ethanolic solution [17], to get a self-assembled monolayer of NTP. The procedure is as follows: the chips are cleaned thoroughly by first rinsing with acetone and isopropyl alcohol in an ultrasonic bath, followed by a 5 mins exposure to an O_2 plasma. The chips are then immersed overnight into a beaker containing 1 mM NTP solution in ethanol. This is followed by a deep cleaning using pure ethanol and N_2 dry clean. As a result, a uniform monolayer of NTP is formed on top of the gold through gold$-$sulphur bond. Note that an overnight soaking to form an NTP monolayer is an overkill and this procedure can be accelerated ($<$ 1 hr) by optimizing the thiol$-$ethanolic solution [12, 18]. Similarly, the accessibility of an analyte to a narrow

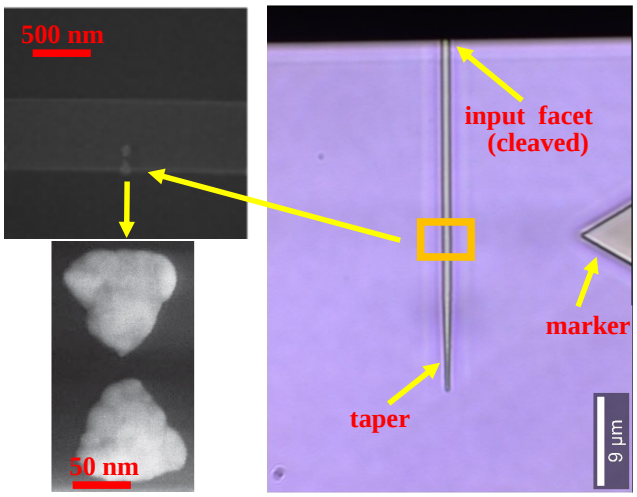

Figure 5.8: Optical microscope (right) and SEM images (left) of a bowtie antenna integrated on a PECVD Si_3N_4 *strip waveguide.*

gaps ($<$ 10 nm) can also be enhanced using wetting techniques [19]. In the next section, the measurement results of the fabricaetd SERS device are presented.

5.2.1.3 Results and discussion

As discussed earlier, the pump wavelength $\lambda_p = 785$ nm is used for all reported results. The same optical setup as presented before in Chapter. 3 (Fig. 3.9) is used. A laser power of 0.5 mW before objective was measured at the entrance facet of a high NA objective (Zeiss 100x/0.9 EC Epiplan NEOFLUAR; ∞/0 objective). A low pump power is used to avoid the photo-reduction of NTP to 4,4-dimercaptoazobenzene (DMAB) through a chemical reduction reaction [20]. We will explain this photo-reduction process in detail in the next chapter. The fundamental TE mode of the waveguide is excited by controlling the polarization using a λ/2 plate. Each spectrum is recorded after optimizing the Raman signal as well as the scattering image using the side camera.

Firstly, Raman spectra are measured from a reference waveguide (0.5 mm long) and from a single antenna integrated waveguide (functionalized) with an access waveguide length of L_a=50 μm. Both waveguide are fabricated on a same chip. The results are presented in Fig. 5.9. No NTP peak is observed from the reference waveguide confirming no NTP binding to the

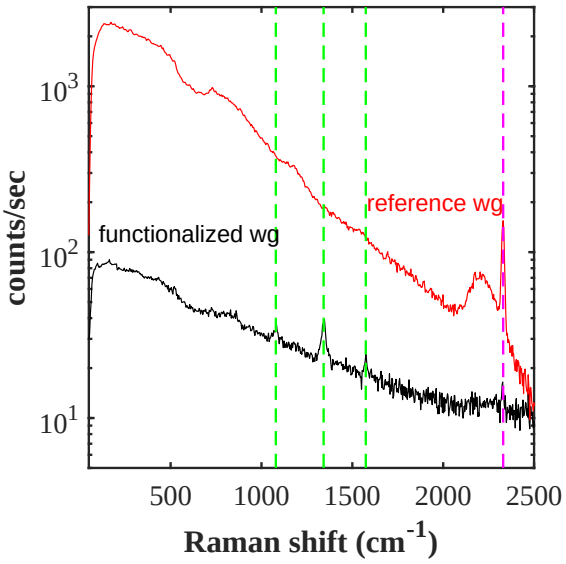

Figure 5.9: (a) The Raman spectrum (black) measured from a functionalized (single antenna integrated) waveguide and a reference Si_3N_4 *waveguide (red) on same sample. Three green dotted lines represents the dominant NTP Raman modes at 1075, 1339 and 1575 cm*$^{-1}$*. The pink dotted line represent* N_2 *Raman line intrinsic to the* Si_3N_4 *background.*

Si_3N_4 waveguide. The spectrum from the plasmonic functionalized waveguide shows not only the NTP Raman modes, but also a weaker background than the reference waveguide. Three green dotted lines represent the position of dominant NTP Raman modes at 1075, 1339 and 1575 cm^{-1}. The pink dotted line represent the Raman mode intrinsic to the Si_3N_4 background. This is attributed to interstitial N_2 incorporated in the waveguide core during the deposition process [15].

As confirmed by Fig 5.9, the access waveguide does not contribute to the NTP spectrum. However, it does generate a broadband background that can mask the SERS signal of interest if its length is too large. Therefore 10 different access waveguide lengths L_a from 50 to 500 μm with a step size of 50 μm are measured using the same experimental parameters. Figure. 5.10.a shows Raman spectra of a waveguide functionalized with a single bowtie antenna. The Raman background Si_3N_4 is increased with

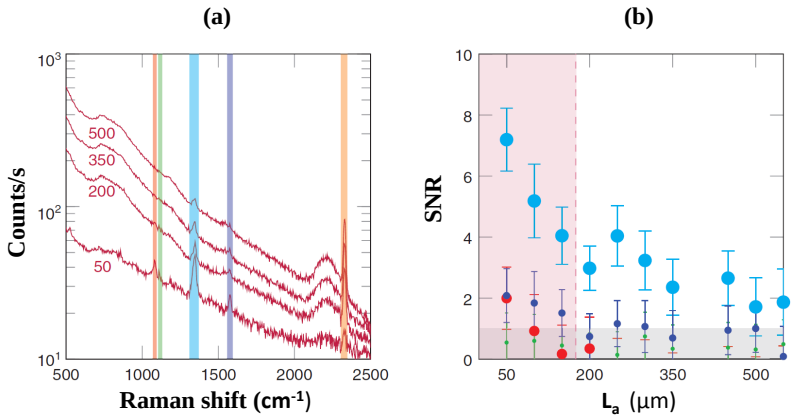

Figure 5.10: Back-scattered Raman spectra of a waveguide covered with a single antenna and varying length L_a = [50:50:500] μm. The access waveguide lengths L_a are mentioned next to their corresponding Raman spectra. SNR of all peaks for N = 1. Each color corresponds to the respective peak in the Raman spectrum. The grey shaded area represents SNR <1 and hence marks a region where detection is impossible. The pink shaded area represents the access waveguide length span ($0 < L_a < 175$ μm) where the second strongest NTP peak (1575 cm^{-1}) is also visible, which is evidenced by an SNR $\geq$ 1. This is adapted from [9].

the access waveguide length. Figure. 5.10.b shows the corresponding SNR for all pNTP peaks as a function of access waveguide length L_a. The grey shaded area represents an area when NTP cannot be detected i.e. SNR $\leq$ 1. The pink shaded area represents the access waveguide length span ($0 < L_a < 175$ μm) where the second strongest NTP peak (1575 cm^{-1}) is also visible, which is evidenced by an SNR $\geq$ 1.

5.3 An antenna integrated on a waveguide vs an antenna embedded in a waveguide

In previous sections, we only assumed the evanescent excitation and collection of SERS signal from a nanoantenna integrated on a waveguide. The coupling between the guided field and the nanostructure takes place in the evanescent region of the waveguide, which is excited by the fundamental TE-like mode having the fundamental electric field component parallel to the chip plane. This results in relatively small interaction efficiencies be-

tween the waveguide mode and nanoantenna. Another way to enhance the coupling efficiency between nanoantenna and the guided mode is by using embedded plasmonic antennas. The relatively simpler geometry e.g. a nanorod, can be embedded into the waveguide [21].

In this section, we will briefly explain the SERS using an embedded bowtie antenna and compare it with evanescently excited nanoantenna. This work has been done with a joint collaboration with Prof. Alejandro Martínez (Nanophotonics Technology Center, Universitat Politecnica de Valencia).

5.3.1 Device design

SEM images of both configurations under study are shown in Fig. 5.11. In the first configuration, a bowtie antenna is integrated on top of the waveguide (Fig. 5.11(a)). While in the second configuration, an antenna is inserted in a subwavelength gap in the waveguide (Fig. 5.11(b)). The fabrication details of both configurations can be found in [22]. Hereafter, we will term these configurations C_1 and C_2, respectively. In both cases, we consider Si_3N_4 waveguides with a rectangular cross-section (width = 700 nm and height = 220 nm) on a silica substrate and bowtie nanoantennas made of gold (Au). For C_1, same design was used as mentioned in Fig. 5.3(b). However, to define an optimized antenna design for C_2, I=$|E|^2$ is calculated using the mode solver. C_2 was designed to get the highest value of I=$|E|^2$ in the wavelength region used in the experiments (λ_p=780 nm and λ_p=877 nm(1339 cm^{-1} NTP Raman mode)). The wavelength at highest I(λ)=$|E(\lambda)|^2$ corresponds to the localized surface plasmon resonance. After optimization, dimensions of the C_2 nanoantenna are: α=64°, W=100 nm, g=48 nm and L=120 nm for waveguide gap of 200 nm. The thickness of the gold layer (t) is kept same in both cases i.e. t=30 nm. All these parameters are previously defined in Fig. 5.3(b). I(λ) for the designed antenna geometry is shown in Fig. 5.14 (solid line). The geometry of the fabricated device is turned out to be α = 59.7°, g=35 nm, t=30 nm and L=135 nm. As shown in Fig. 5.14 (dashed line), I(λ) for the designed antenna geometry is slightly red-shifted. To estimate the coupling efficiency of a scattered signal to a waveguide, β=$\frac{P_{coupled}}{P_T}$ is also calculated for both configurations where $P_{coupled}$ and P_T are the waveguide coupled and the total scattered power of a dipole. In both cases, a dipole source is assumed in the middle of the gap. Remarkably, $\beta(\lambda = 877nm)$ turns out to be 17% for C_2 configuration. While, $\beta(\lambda = 877nm)$ for C_1 is 5.5%. This shows that the waveguide coupled scattered signal from a dipole oscillating in the middle of antenna with C_2 configuration is at least 3 times larger than an antenna with C_1.

(a)

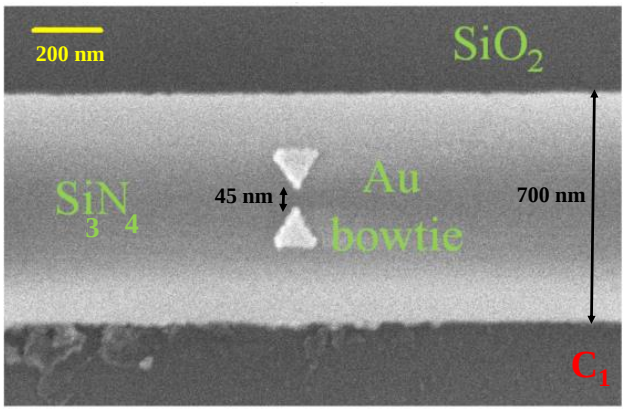

(b)

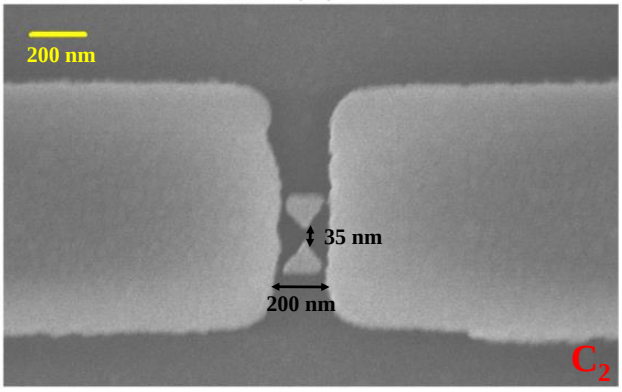

Figure 5.11: SEM images of the fabricated samples for both configurations C_1 (antenna is integrated on top of the waveguide) and C_2 (antenna is inserted into the waveguide gap of 200 nm). The yellow line stands for 200 nm.

5.3.2 Experimental results

The 4-Nitrothiophenol (NTP) monolayer is used to characterize the performance of both sensors. Both chips are cleaved in way that the access waveguide length is approximately 400 μm. A pump power of 1 mW (before objective) and 1 sec integration time are used. The same optical setup as presented before in Chapter. 3 (Fig. 3.9) is used. The fundamental TE mode of the waveguide is excited by controlling the polarization using a

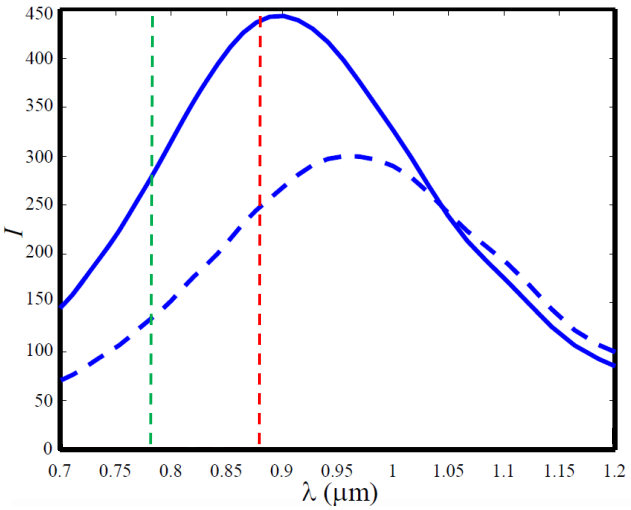

Figure 5.12: I(λ)=$|E(\lambda)|^2$ for the designed (solid line) and fabricated (dashed line) C_2 antenna geometry. The dimensions of the designed nanoantenna are: α=64°, W=100 nm, g=48 nm, t=30 nm and L=120 nm for a waveguide gap of 200 nm. The geometry of the fabricated device is turned out to be α = 59.7°, g=35 nm, t=30 nm and L=135 nm. Green and red dashed lines represent pump (λ_p=785 nm) and Stokes (λ_s=877 nm (1339 cm^{-1} NTP Raman mode)) wavelengths, respectively.

λ/2 plate. Each Raman spectrum is recorded after optimizing the Raman signal as well as the scattering image using the side camera.

The measurement results are presented in Fig. 5.13. No NTP peak is seen in the Raman spectrum measured from a reference waveguide (black). However, a strong NTP spectrum is present in the signal recorded from the waveguide functionalized with a single antenna (red). Apart from the expected pNTP Raman modes, a spurious Raman like background generated from the Si_3N_4 waveguide is observed in all Raman spectra. In the first set of measurements, the chip containing a set of waveguides with the bowtie on top (C_1) is measured. The Raman peak of the 1339 cm^{-1} mode is visible in Fig. 5.13(a). However, due to the low excitation and collection efficiency, no other Raman modes are present. In the second set of the measurements, the set of samples with antennas in the gap (C_2) was explored. As shown in Fig 6(b), aside from 1339 cm^{-1} Raman modes, two more peaks at 1076 cm^{-1} and 1580 cm^{-1} (benzene ring vibrations) also appear in Raman spectra.

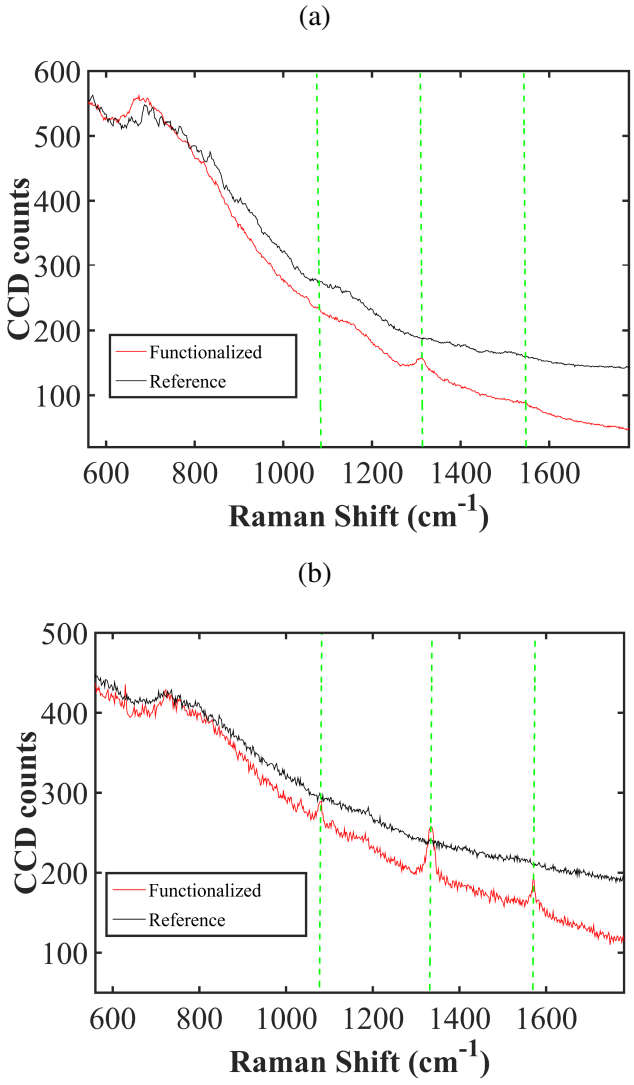

Figure 5.13: Raman spectra measured from waveguides functionalized with single antenna for a) C_1 and b) C_2 configurations. The green dotted line represents the NTP Raman modes i.e. 1080, 1339 and 1575 cm^{-1}.

In the Fig. 5.14, we compare the Raman signal strength measured from both antenna configurations. For the same pump power and integration time, the Raman signal recorded for C_2 is at least three times stronger than

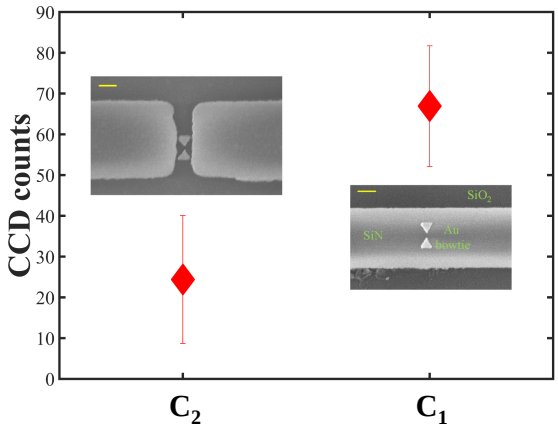

Figure 5.14: CCD counts corresponding to 1339 cm^{-1} Raman mode of NTP for C_1 and C_2 configurations. The error bar corresponds to standard deviation along 5 identical waveguides on the same chip.

in C_1, where both antenna geometries were optimized for the highest signal strength. It is worth mentioning that the dimension of the fabricated bowties were a little bit different from the nominal bowtie geometry because of fabrication inaccuracies. Further improvement can be achieved by sweeping design parameters on the mask layout.

5.4 Conclusion

In this chapter, the SERS using integrated plasmonic antennas on a dielectric waveguide is presented. An analytical formalism is presented to quantify the SERS signal generated from a monolayer. The SERS performance of an integrated arch dipole antenna and a bowtie antenna is also compared analytically. The effect of the Raman background of a dielectric waveguide on the SERS signal is also analyzed both analytically as well as experimentally. In the end, we demonstrate the SERS using an antenna embedded into the subwavelength gap of a waveguide. The result shows that SERS signal with this antenna configuration is at least three times stronger than the evanescently excited and collected SERS (an antenna sitting on top of the waveguide).

To this end we have considered a bowtie antenna integrated on a waveguide and an antenna embedded into the waveguide. More efficient antenna

design can boost the overall SERS enhancement. For example one of the designs discussed in this chapter is an arch dipole antenna integrated on a single mode Si_3N_4 waveguide. Likewise, double-resonance plasmonic antennas can also be used where both resonance are tuned at pump and Stokes wavelength [23]. Also, devices presented in this chapter, are fabricated using e-beam lithography. Therefore, it hinders the mass scalability. In the next chapter, we will introduce another integrated sensor geometry that provides higher SERS signal as compared to the nanoantenna and at the same time can be fabricated using an e-beam free lithography technique.

References

[1] Surbhi Lal, Stephan Link, and Naomi J Halas. *Nano-optics from sensing to waveguiding*. Nature photonics, 1(11):641, 2007.

[2] Argishti Melikyan, Luca Alloatti, Alban Muslija, David Hillerkuss, Philipp C Schindler, J Li, Robert Palmer, Dietmar Korn, Sascha Muehlbrandt, Dries Van Thourhout, et al. *High-speed plasmonic phase modulators*. Nature Photonics, 8(3):229, 2014.

[3] Mahsa Darvishzadeh-Varcheie, Caner Guclu, Regina Ragan, Ozdal Boyraz, and Filippo Capolino. *Electric field enhancement with plasmonic colloidal nanoantennas excited by a silicon nitride waveguide*. Optics express, 24(25):28337–28352, 2016.

[4] Felipe Bernal Arango, Andrej Kwadrin, and A Femius Koenderink. *Plasmonic antennas hybridized with dielectric waveguides*. ACS nano, 6(11):10156–10167, 2012.

[5] Marta Castro-Lopez, Nuno de Sousa, Antonio Garcia-Martin, Frederic Y Gardes, and Riccardo Sapienza. *Scattering of a plasmonic nanoantenna embedded in a silicon waveguide*. Optics express, 23(22):28108–28118, 2015.

[6] Nina Turk, PC Wuytens, Ali Raza, Andre Skirtach, and Roel Baets. *Organic Adhesion Layer for an Increased Waveguide-Excited Surface-Enhanced Raman Signal*. In Laser Science, pages JW3A–82. Optical Society of America, 2017.

[7] Frédéric Peyskens, Ananth Z Subramanian, Pieter Neutens, Ashim Dhakal, Pol Van Dorpe, Nicolas Le Thomas, and Roel Baets. *Bright and dark plasmon resonances of nanoplasmonic antennas evanescently coupled with a silicon nitride waveguide*. Optics express, 23(3):3088–3101, 2015.

[8] Frederic Peyskens, Ashim Dhakal, Pol Van Dorpe, Nicolas Le Thomas, and Roel Baets. *Surface Enhanced Raman Spectroscopy Using a Single Mode Nanophotonic-Plasmonic Platform*. ACS Photonics, 3(1):102–108, 2016.

[9] Frédéric Peyskens, Pieter Wuytens, Ali Raza, Pol Van Dorpe, and Roel Baets. *Waveguide excitation and collection of surface-enhanced Raman scattering from a single plasmonic antenna*. Nanophotonics, 2018.

[10] Tae Joon Seok, Arash Jamshidi, Michael Eggleston, and Ming C Wu. *Mass-producible and efficient optical antennas with CMOS-fabricated nanometer-scale gap*. Optics Express, 21(14):16561–16569, 2013.

[11] Ali Raza, Frédéric Peyskens, Stéphane Clemmen, and Roel Baets. *Towards single antenna on-chip surface enhanced Raman spectroscopy: Arch dipole antenna*. In 7th International Conference on Metamaterials, Photonic Cyrstals and Plasmonics (META16), 2016.

[12] A. Jakubowicz, H. Jia, R. M. Wallace, and B. E. Gnade. *Adsorption Kinetics of p-Nitrobenzenethiol Self-Assembled Monolayers on a Gold Surface*. Langmuir, 21(3):950–955, 2005. PMID: 15667173.

[13] David P Fromm, Arvind Sundaramurthy, P James Schuck, Gordon Kino, and WE Moerner. *Gap-dependent optical coupling of single bowtie nanoantennas resonant in the visible*. Nano letters, 4(5):957–961, 2004.

[14] Charles A Goss, Deborah H Charych, and Marcin Majda. *Application of (3-mercaptopropyl) trimethoxysilane as a molecular adhesive in the fabrication of vapor-deposited gold electrodes on glass substrates*. Analytical Chemistry, 63(1):85–88, 1991.

[15] Ashim Dhakal, Pieter Wuytens, Ali Raza, Nicolas Le Thomas, and Roel Baets. *Silicon nitride background in nanophotonic waveguide enhanced Raman spectroscopy*. Materials, 10(2):140, 2017.

[16] Sebastian Romero-García, Florian Merget, Frank Zhong, Hod Finkelstein, and Jeremy Witzens. *Silicon nitride CMOS-compatible platform for integrated photonics applications at visible wavelengths*. Optics express, 21(12):14036–14046, 2013.

[17] J. Christopher Love, Lara A. Estroff, Jennah K. Kriebel, Ralph G. Nuzzo, and George M. Whitesides. *Self-Assembled Monolayers of Thiolates on Metals as a Form of Nanotechnology*. Chemical Reviews, 105(4):1103–1170, 2005. PMID: 15826011.

[18] Sasan Asiaei, Patricia Nieva, and Mathilakath M. Vijayan. *Fast Kinetics of Thiolic Self-Assembled Monolayer Adsorption on Gold: Modeling and Confirmation by Protein Binding*. The Journal of Physical Chemistry B, 118(47):13697–13703, 2014. PMID: 25353396.

[19] Chang Chen, XiuMei Xu, Yi Li, Hilde Jans, Pieter Neutens, Sarp Kerman, Guy Vereecke, Frank Holsteyns, Guido Maes, Liesbet Lagae, Tim Stakenborg, and Pol van Dorpe. *Full wetting of plasmonic nanopores through two-component droplets*. Chem. Sci., 6:6564–6571, 2015.

[20] Ping Xu, Leilei Kang, Nathan H Mack, Kirk S Schanze, Xijiang Han, and Hsing-Lin Wang. *Mechanistic understanding of surface plasmon assisted catalysis on a single particle: cyclic redox of 4-aminothiophenol*. Scientific reports, 3:2997, 2013.

[21] Alba Espinosa-Soria, Amadeu Griol, and Alejandro Martínez. *Experimental measurement of plasmonic nanostructures embedded in silicon waveguide gaps*. Optics express, 24(9):9592–9601, 2016.

[22] J. Losada, A. Raza, S. Clemmen, A. Serrano, A. Griol, R. Baets, and A. Martinez. *SERS Detection via Individual Bowtie Nanoantennas Integrated in Si3N4 Waveguides*. IEEE Journal of Selected Topics in Quantum Electronics, 25(3):1–6, May 2019.

[23] Yizhuo Chu, Mohamad G Banaee, and Kenneth B Crozier. *Double-resonance plasmon substrates for surface-enhanced Raman scattering with enhancement at excitation and stokes frequencies*. ACS nano, 4(5):2804–2810, 2010.

6

SERS using hybrid plasmonic slot waveguide

6.1 Introduction

In the previous chapter, we presented an on-chip surface enhanced Raman spectroscopy (SERS) using the nanoplasmonic antennas integrated on a single mode Si_3N_4 waveguide. The combination of integrated photonics with plasmonic structures can indeed provide a strong field enhancement resulting in an enhanced light−matter interaction [1–4]. SERS relies on a plasmonic enhancement for increasing the electric field strength by many orders of magnitude. Many SERS substrates have been developed [5–7] providing more reproducible Raman spectra. In this chapter we introduced another efficient on-chip Raman sensor, in which plasmonic antennas are replaced by metal slot waveguides. Raman spectroscopy using metal waveguide gain both from a strong field enhancement due to the highly confined propagating plasmon polariton gap mode and a limited spurious background, thanks to limited field overlap with the dielectric waveguide. Moreover, the fabrication avoids any use of e-beam lithography and rather relies on the atomic layer deposition (ALD) to create the nanometer scale gaps required for a large plasmonic enhancement. Unlike plasmonic nanoantenna, this plasmonic slot waveguide offers micrometer long interaction length and an off-resonant enhancement hence a broadband Raman conversion ef-

ficiency [8–10]. In this chapter, the sensor is tested using a monolayer of 4-Nitrothiophenol (NTP) and bulk ethanol. The performance of this sensor is compared with other on-chip SERS substrates discussed before. Furthermore, another step towards scalable and fabrication-less 10 nm wide nanotrenches integrated on Si_3N_4 is taken. 10 nm wide nanotrenches are grown directly on a slot waveguide using a novel ALD gold process. In the end, the SERS performance of waveguide excited SERS sensors is compared with the state of the art free space excited SERS substrate.

6.2 Metal-dielectric-metal structures

Due to the small effective modal area, sub-wavelength field confinement and micrometers long propagation length [11], the metal-dielectric-metal (MDM) structures have attracted huge attention. Unlike metal-dielectric slab where only a SPP mode at ω_{SP} is propagating, MDM structure supports the guided modes in a long wavelength range. In Chapter. 2. we analyzed the enhanced spontaneous emission rate of a dipole sitting inside an MDM structure that indeed shows a broad band enhanced emission. This is an advantage over a nanoplasmonic antenna, where the FWHM is limited ($<$ 150-200 nm) due to the resonant nature of the localized plasmonic mode.

Since the last decade, there is a huge interest in integrating these MDM waveguides with other photonic functionalities to envision a complete on chip photonic systems e.g. on chip modulators [12] and refractive index sensors [13]. Usually, the MDM waveguides are integrated with a dielectric strip waveguides using a mode transition structure. Normally, a taper is introduced between a MDM waveguide and dielectric strip waveguide that transits the mode in an adiabatic fashion [14, 15]. However, due to the good mode matching in the case of slot waveguide, an efficiency up to 70% is still possible by connecting metal and photonic slot waveguide without any transition [16, 17]. This can be further improved by introducing a gap structure between both waveguide [17]. In the next sections, we are introducing another MDM like waveguide structure that is connected directly with a PECVD Si_3N_4 slot waveguide.

6.3 Device design

The geometry of the sensor is depicted in Fig. 6.1. The plasmonic sensor is preceded by a low loss 400 μm long Si_3N_4-Al_2O_3 slot waveguide acting as an access waveguide. Al_2O_3 is used as an intermediate layer owing to

its low Raman background as we seen before in Chapter. 3. The length of the plasmonic waveguide (L_p) is set to 100 μm, far larger than the expected decay length (5 μm).

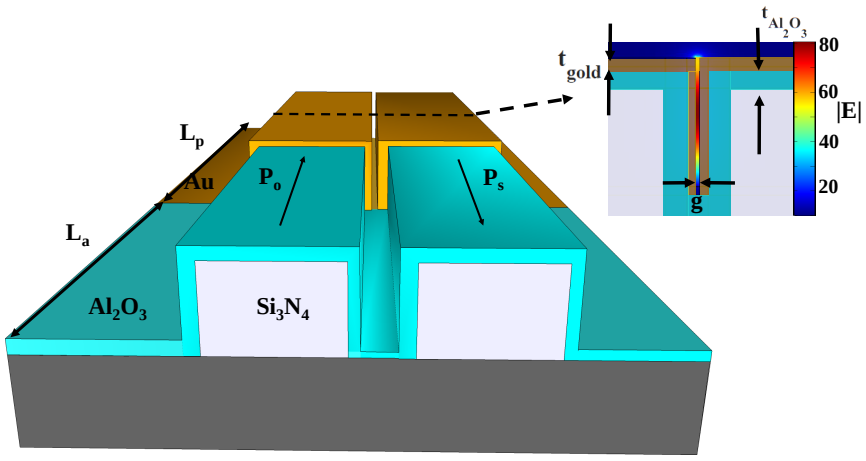

Figure 6.1: The schematic of hybrid Si_3N_4 *-* Al_2O_3*- Gold waveguide. Right top inset shows the propagating plasmon excited using fundamental TE mode of access waveguide .*

The fundamental TE mode of the Si_3N_4-Al_2O_3 slot waveguide at a pump wavelength λ_p excites the gap plasmonic mode with a coupling efficiency γ_p. This propagating surface plasmon polariton (PSPP) mode is strongly confined in the gap (g) and interacts with the analyte (NTP) uniformly lying over the gold. The pump beam excites the vibrational modes of the NTP molecules to generate the enhanced Stokes signal that mostly remains coupled to the hybrid plasmonic mode (in both contra- and co-propagating directions). This enhanced pump excitation and subsequent stokes signal generation can be computed numerically to estimate the Raman conversion efficiency η (see Eq. 3.4). The backward collected signal increases until a certain waveguide length and then saturates due to the decay of pump light. The saturation length is set by the total waveguide loss α_p. The total Stokes signal P_s normalized by the total guided pump power P_o for the device operating in the aforementioned setup can be defined nu-

merically as

$$\frac{\mathrm{P_s}}{\mathrm{P_o}} = \zeta = (\gamma_\mathrm{p}\gamma_\mathrm{s}) \times \eta \times \sigma \times \rho \times \overbrace{\left(\frac{1 - e^{-(\alpha_p + \alpha_s)L_p}}{\alpha_\mathrm{p} + \alpha_\mathrm{s}}\right)}^{\text{Length factor}} \tag{6.1}$$

where ρ and σ are the molecular density and differential Raman cross section of the analyte. The length factor represents the SERs signal dependence on plasmonic waveguide length (L_p). Similar equation was defined before (Eq. 3.6) for a back-scattered signal from an analyte lying on a dielectric waveguide.

6.4 Simulations

To analyze the effect of gold thickness t_{gold} and ALD alumina thickness $t_{Al_2O_3}$, a COMSOL Multiphysics mode solver is used to compute the eigenmodes of the hybrid $\mathrm{Si_3N_4} - \mathrm{Al_2O_3} - \mathrm{Au}$ waveguide. We consider a $\mathrm{Si_3N_4}$ slot waveguide with a refractive index of $n_{Si_3N_4} = 1.9$, coated with an $\mathrm{Al_2O_3}$ layer whose refractive index is $n_{Al_2O_3} = 1.6$ and a final thin coating of gold whose complex refractive index is given by the Johnson and Christy model. Our simulation assumes only hybrid$-$TE excitation (maximum |E| along the surface of the sample) as this mode possesses the highest field confinement into the gap. The electrical field strength |E| is plotted in Fig. 6.1 showing the field confinement (≈ 92 % for g=20 nm) is much stronger than in the case of a $\mathrm{Si_3N_4}$ slot waveguide (≈ 35 % for g=150 nm). This confinement is expected to strongly reduce the spurious background flux of photons originating from the guiding core of the waveguide ($\mathrm{Al_2O_3}$ and $\mathrm{Si_3N_4}$). The test monolayer of NTP is 1$-$nm thick and selectively binds to gold. Knowing its refractive index [18] $n_{NTP} = 1.62$ and the Raman resonance of 1339 cm^{-1} ($\nu_s(NO_2)$), we can estimate the conversion efficiency η when the pump wavelength is set to 785 nm and the Stokes wavelength is 877 nm. For a 100 μm long plasmonic waveguide, the ratio $\zeta = P_s/P_o$ of the generated Stokes power over the incoming pump power is plotted in Fig. 6.2 for a range of thicknesses $t_{Al_2O_3}$ and t_{gold} chosen such that the gap (g) ranges from 150 nm to 10 nm. For simplicity, we keep a constant coupling coupling efficiency i.e. $\gamma_p = \gamma_s = 5$ dB for all combinations of $t_{Al_2O_3}$ and t_{gold}. The plot shows a nearly constant enhancement for a fixed gap size, that is a fixed $t_{Al_2O_3} + t_{gold}$. For our design, we target a thicker alumina layer ($\sim$ 58 nm) and rather thin gold layer ($\sim$ 13-16 nm) for two reasons. Indeed, the thickness of $\mathrm{Al_2O_3}$ is experimentally better controlled (thanks to ALD) leading to an easier fabrication. Moreover, a lesser amount of gold

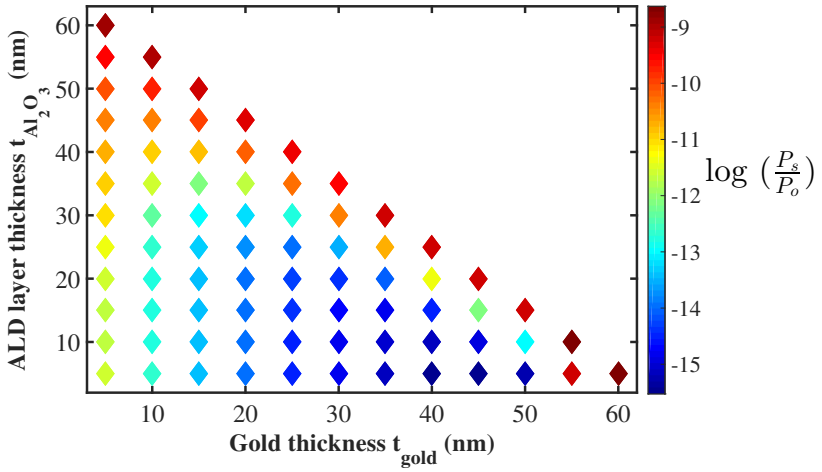

Figure 6.2: The dependence of $\zeta = P_s/P_o$ on gold thickness t_{gold} and ALD alumina thickness $t_{Al_2O_3}$ for 100 μm long plasmonic waveguide. The color bar is plotted in log scale.

also reduces the reflection at the transition between access and plasmonic waveguide. For example, for $t_{Al_2O_3}$=12 nm and t_{gold}=58 nm, the back reflection of pump light is -22.7 dB. on the other hand, for $t_{Al_2O_3}$=58 nm and t_{gold}=12 nm, the back reflection drops to -38.7 dB (see Appendix C). For $t_{Al_2O_3} = 58$ nm and $t_{gold} = 13$ nm, the plasmonic waveguide losses at pump (α_p) and Stokes wavelength (α_s) measured using the cut-back method are respectively 2.4 and 2.1 dB/μm (see Appendix C). Similarly, the measured γ_p and γ_s are 3.95 and 5.1 dB/facet respectively. For these values of α_p, α_s, γ_p, γ_s and a plasmonic waveguide length $L_p = 100$ μm, ζ calculated using COMSOL Multiphysics mode solver is 1.96×10^{-9}. The single molecule enhancement factor [19] i.e. SMEF= $|E(\lambda_p)|^2|E(\lambda_s)|^2$ is also calculated by assuming a dipole located in the middle of gap i.e. SMEF $= 1.5 \times 10^7$.

6.5 E-beam free fabrication

SERS sensors presented in the previous chapter were fabricated using electron beam lithography (EBL). EBL gives high resolution down to sub 10 nm. However, EBL offers low throughput due to a dot-by-dot fashion exposure, therefore, it hinders the mass scalability. Wuytens et al, demonstrated nanotraingles fabricated on a dielectric strip waveguide using micro-sphere lithography [20]. Micro-sphere lithography demands wider waveg-

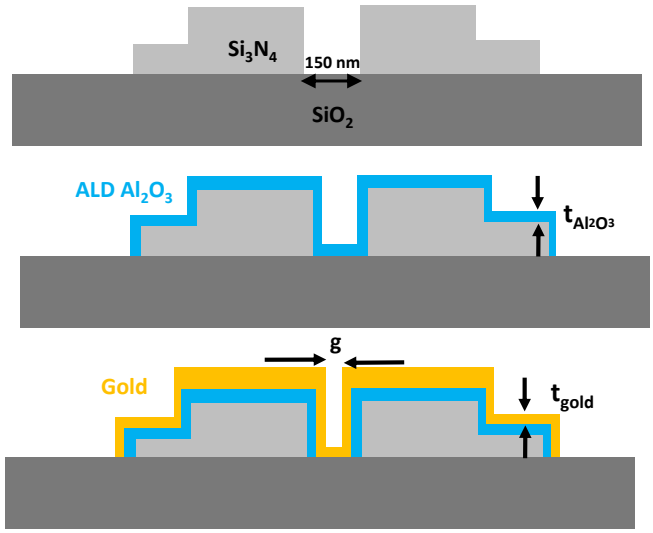

Figure 6.3: Fabrication steps of ALD assisted metal slot waveguide. $t_{Al_2O_3}$ and t_{gold} are thicknesses of ALD alumina and gold layer. g is the metal slot gap.

uide, hence limits the excitation efficiency. Also, as in the case of e-beam fabricated bowties, nanotriangles are fabricated on a strip waveguide that generates huge Raman background as compared to slot waveguide [21].

The patterning technique we used here for metal slot waveguide is based on an atomic layer deposition of Al_2O_3. The process is as follows: Si_3N_4 slot waveguides used for our experiments are fabricated at imec on a 200 mm silicon wafer containing a stack of $2.3 \pm 0.1\mu$m thick high-density plasma enhanced chemical vapor deposition (PECVD) silicon oxide SiO_2 and 220 nm thick PECVD Si_3N_4 [22]. The structures are patterned with 193 nm optical lithography and subsequently etched by fluorine based inductive coupled plasma-reactive ion-etch process to attain the final structure. The resulting average slot width is 150 nm. The waveguide topology is depicted in Fig. 6.3. Then, the structure is conformally coated with 58 nm of Al_2O_3 using atomic layer deposition (ALD). Figure. 6.4 shows the modal overlap with Al_2O_3 layer that goes upto 14% for t_{gold} = 20 nm and $t_{Al_2O_3}$ = 30 nm. Considering such a high modal overlap, the low Raman background material is essential to avoid any extra background. Therefore, ALD Al_2O_3 is chosen based on our previous analysis (see Chapter 3). The result shows that Al_2O_3 exhibits minimal Raman background as compared to PECVD Si_3N_4. The ALD deposition is performed in a home built ALD setup that has a base pressure of 10^{-6} mbar. Deposition of the Al_2O_3 layer

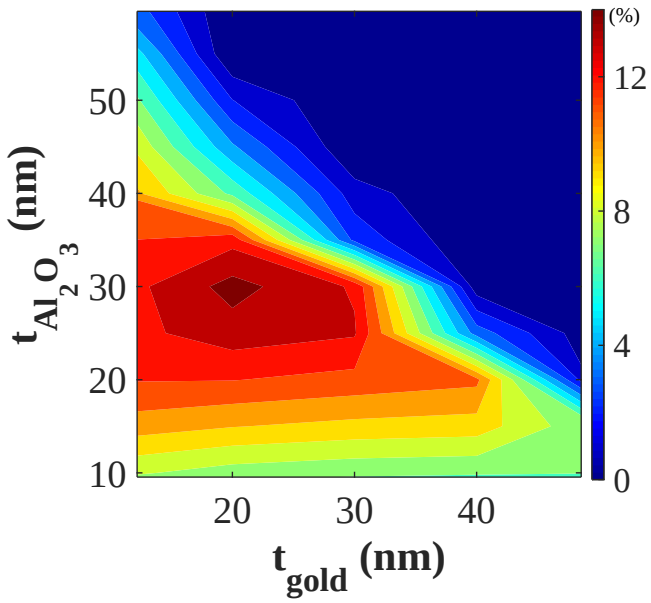

Figure 6.4: The modal confinement factor in the ALD Al_2O_3 layer. $t_{Al_2O_3}$ and t_{gold} are thicknesses of ALD alumina and gold layer as defined in Fig. 6.3.

is performed using a thermal ALD process [23] at a substrate temperature of 120°C using trimethylaluminum and water pulses of 5s at 5×10^{-3} mbar. After the Al_2O_3 deposition, AZ 5214 resist is spin coated over the chip using 3500 RPM and 40 sec spinning time. This is followed by an 11 sec DUV exposure, 3 min post bake at 120 C and a 50 sec flood-e exposure (for image reversal). After the DUV exposure, the development was done in a solution containing AZ400: DI$-$water (3:1). A short O_2 plasma (PVA-TEPLA GIGAbatch 310 m, 6000 sccm O_2, 600 W, 750 mTorr) was performed to remove the residual resist. A thin $1-2$ nm of Ti followed by a 13-15 nm of gold along the side wall is deposited using the Au-sputtering. Finally, a 100 μm gold waveguide is defined using the metal lift-off. The SEM images of the final fabricated device are shown in Fig. 6.5.

After the fabrication, the back silicon is thinned down from 750 μm to 250 μm using 20 μm Al_2O_3 particles by means of Logitech lapping machine. This helps in cleaving the chips with an accuracy of $\pm 50\ \mu m$.

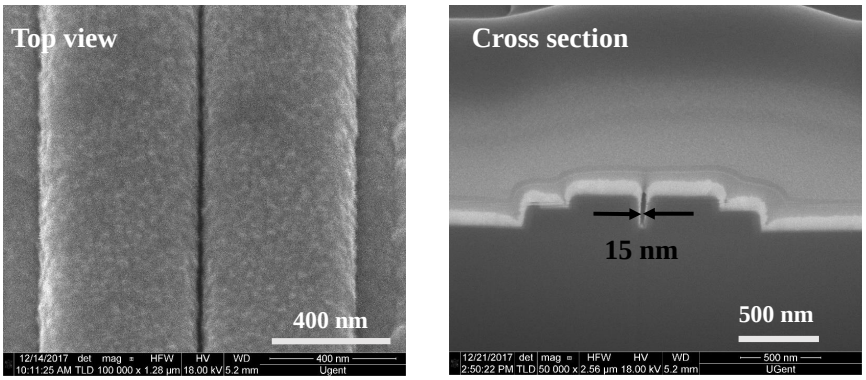

Figure 6.5: SEM images of hybrid metal slot waveguide waveguide (Top view and cross section of the fabricated device).

6.6 Experimental results: Using a monolayer

Due to the relatively high Raman cross section and efficient binding with the gold, 4-nitrothiophenol (NTP) is used as an analyte monolayer to characterize the sensor. Also, our choice of a monolayer as an analyte supports many bio-applications from clinical diagnostics, proteomics, genomics and bio-materials to tissue engineering [20, 24–26]. The same binding recipe as mentioned in the previous chapter is used to bind the NTP to gold surface.

As discussed earlier, the pump wavelength $\lambda_p = 785$ nm is used for all report ed results unless it is mentioned explicitly. Raman spectra are measured from both 100 μm long gold coated and 0.6 mm long bare Si_3N_4 slot waveguides, the latter serving as a reference. The results are presented in Fig. 6.6. Both chips have been processed so that a monolayer of NTP coats the gold nanostructures. Indeed, no NTP peak can be seen from the reference waveguide (free of gold). The spectrum from the plasmonic waveguide shows not only the NTP Raman modes, but also a weaker background than the reference waveguide. This is because the pump beam is strongly attenuated in the plasmonic structure and no further Raman background is generated after it. In the absence of gold, light is much less attenuated and a spurious background is generated after the sensor. It is interesting to study the dependence of the SERS signal on the length of the plasmonic

waveguide (L_p) and the length of the access waveguide (L_a). In the first set of experiments, the access waveguide length is kept constant while the plasmonic waveguide length is varied from 0 to 290 μm. As shown in Fig. 6.6.b, the signal increases with the waveguide length until 15 μm and then saturates due to the decay of the pump light. Fitting the length factor of Eq. 6.1 gives $\alpha_p = \alpha_s = 3.0 \pm 1.2$ dB/μm, where the large error bar is due to the limited number of points at short waveguide lengths. This value fits well to the α_p and α_s measured using the cut-back method i.e. 2.4 dB/μm and 2.1 dB/μm respectively (see Appendix C). This interaction length is rather long for a plasmonic structure and this obviously contributes to the high Raman conversion efficiency. It is worth mentioning that α_p depends on the final plasmonic gap (g) i.e. it increases with decreasing plasmonic gap due to higher modal interaction with gold [27]. In the second set of measurements, the effect of the access waveguide length (L_a) is investigated. As confirmed by Fig 6.6.a, the access waveguide does not contribute to the NTP spectrum. However, it does generate a broadband background that can mask the SERS signal of interest if its length is too large [28]. Therefore 8 different access waveguide lengths L_a from 10 to 410 μm with a step size of 50 μm are measured using the same experimental parameters. As shown in Fig. 6.6.c, the signal to background ratio decreases with increasing access waveguide length. As a third experiment, we explore the spatial reproducibility of the SERS spectra by measuring the relative standard deviation percentage (RSD $\%$) of the SERS signal of all the Raman modes of NTP for 24 different waveguides from three different chips (eight each). Each spectrum is measured using the same pump power, access waveguide length, CCD settings and integration time. As shown in Fig. 6.6.d, all NTP modes except 1080 and 1339 cm^{-1} shows high stability with RSD$\% < 5\%$. This variation is mainly attributed to differences in coupling efficiencies, random gold roughness and optical alignment inaccuracy. The increased variability at the 1080 and 1339 cm^{-1} modes is attributed to chemical instability of the NTP exposed to high optical fields and will be discussed hereafter. This SERS signal variation in our plasmonic slot waveguide is comparable to the state-of-the-art SERS substrates for free-space excitation at 785 nm pump wavelength [29, 30].

6.6.1 Broadband Enhancement

In Chapter. 2. we analyzed the enhanced spontaneous emission rate of a dipole sitting inside a MDM structure that showed an enhanced emission that is broadband. This is an advantage over a nanoplasmonic antenna, where the FWHM is limited ($<$ 150-200 nm) due to the resonant nature of

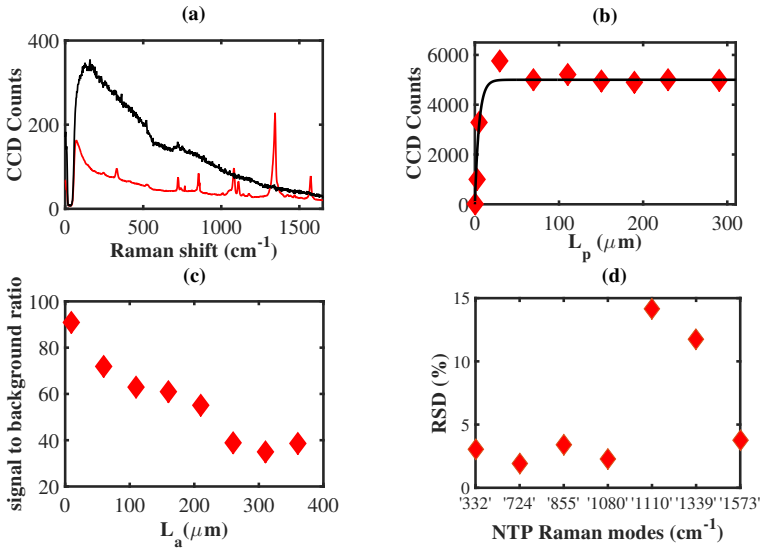

Figure 6.6: The measured back-scattered SERS signal of a plasmonic slot waveguide with $t_{Al_2O_3}$ = 58 nm and t_{gold} = 13 nm. a) Raman spectrum measured from a functionalized plasmonic waveguide (red) and reference waveguide (black). b) SERS signal at 1339 cm^{-1} NTP Raman modes vs the length of plasmonic waveguide (L_p). The black curve represents the length factor fit, from which we extract $\alpha_p = \alpha_s \approx$ 3.0 dB/μm. c) Signal-to-background ratio versus access waveguide length and d) the relative standard deviation percentage (RSD %) of SERs signal measured from 24 different waveguides on three different chips. All spectra are extracted using 1 mW pump power (before objective) and 1 sec integration time.

the localized plasmonic mode. While most plasmonic structures used for SERS rely on a localized surface plasmon resonance, our plasmonic slot waveguide uses a gap propagating surface plasmon polariton (PSPP) that offers broadband and off-resonant enhancement. As a consequence, we expect a signal enhancement that has a reduced dependence on the excitation- and emission wavelength. To demonstrate this broadband nature of the field enhancement, we have taken SERS spectra at two different excitation wavelengths. The reported spectra in Fig. 6.7.a, are recorded at identical pump power (1 mW) and integration time (1 sec) but for a pump wavelength of 632 nm and 785 nm. The spectrum at shorter wavelength is stronger as compared to the one resulting from 785 nm excitation. However, the spurious background level also increases due to the relative stronger photoluminescence of gold at shorter wavelength [31]. This result highlights the broadband enhancement of our Raman sensor and the fact that it can be used for any stokes Raman shift contrasting with the field enhancement in nanoplasmonic antenna where the resonance is limited to $\approx$ 100 nm. To the best of our knowledge, this is the first broadband SERS demonstration of an on-chip SERS Raman sensor.

6.6.2 Limitation on pump power

Another common limitation of plasmonic structures for Raman spectroscopy is the maximum optical excitation power $P_o^{\max}$ that can be used before degrading (or photo-conversion) the sample/analyte under study. Indeed, this limits the pump power that can be used and therefore the strength of the Raman signal. Due to the relatively low localization of the electric field as compared to nanoplasmonic antennas, our propagating plasmon based sensor is expected to have large $P_o^{\max}$. When exposed to too large intensity, NTP molecules start to photo-reduce in a form of dimercaotoazobenzene (DMAB). In order to find $P_o^{\max}$, a series of spectra has been recorded at different pump powers with 1 sec integration time each. The photo degradation of NTP to dimercapotoazobenzene (DMAB) can be monitored using the SERS intensity at 1339 cm^{-1} vs P_O. The power level at which I_{1339} shows non-linearity against P_O corresponds to the photoreduction of NTP into DMAB. As presented in Fig. 6.7.b, the 1339 cm^{-1} peak starts to decay after $P_o^{\max}$ = 0.8 mW pump power guided into the access waveguide, while the peaks at 1145 cm^{-1} due to β(CH), 1383 and 1443 cm^{-1} due to $\nu(\mathrm{N=N})$ increases in intensity, that shows the gradual conversion of NTP to DMAB. The Si_3N_4 background at 400 cm^{-1} also scales linearly with the pump power confirming no photo-damage to Si_3N_4 at higher powers. Figure. 6.8 shows the same NTP photo-conversion phenomenon using the

nano-triangles integrated on Si_3N_4 waveguide. In this case NTP starts to photo-reduce at 0.2-0.3 mW guided power. A similar observation has been reported before [32, 33], where NTP molecules bind to a SERS substrate were excited at the pump wavelength of 532 and 632 nm using the free space optics.

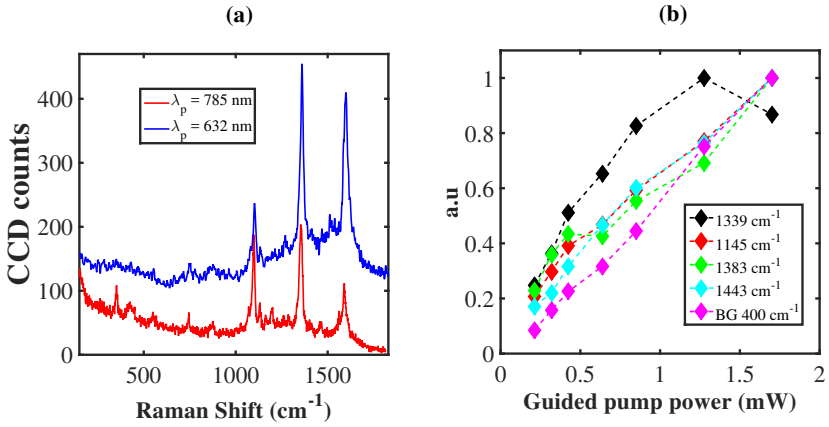

Figure 6.7: a) The back-scattered Raman spectra measured at pump wavelength of λ_p=632 nm (blue) and λ_p=785 nm (red). b) The photo induced reduction of 4-NTP into DMAB monitored using integrated counts at 1339, 1145, 1383 and 1443 cm^{-1} vs total guided power. The Si_3N_4 background (BG) is also plotted at 400 cm^{-1}.

6.6.3 Waveguide vs free space excitation

Next, we made a comparison between the Raman signal strength obtained through a metal slot waveguide excitation and collection (waveguide excited) versus the excitation and collection through a high NA conventional microscope objective (top-down free space (FS)). A 2 mW pump power before the objective (Zeiss $100 \times /0.9$ EC Epiplan NEOFLUAR: $\infty/0$) and 60 sec integration time are used for both cases. The results are shown in Fig 6.9. First, a reference spectrum is measured through top-down excitation and collection from a position on the sample containing no metal slot waveguide. No NTP peak is seen in the reference spectrum (red colour). Next, a spectrum is recorded from a metal slot waveguide (green colour). The spectrum contains the dominant modes of NTP i.e. 1110, 1339 and 1573 cm^{-1}. Also, both spectra contain the 520 cm^{-1} Raman detuning of

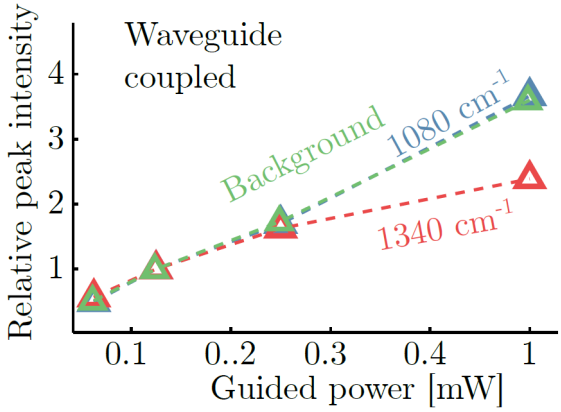

Figure 6.8: Relative peak strength for the nanotriangle pattern excited through a waveguide. The photo induced reduction of 4-NTP into DMAB monitored using integrated counts at 1339, 1080 and 2330 cm^{-1} vs total guided power. Taken from [34]

the underlying silicon substrate. Finally, the light is butt coupled to the same metal slot waveguide preceded by 100 μm reference waveguide. The collected Raman spectrum (blue colour) is shown in Fig 6.9. The waveguide excited and collected spectrum shows all Raman modes of NTP. The results show that for a fixed pump power before an objective, the Raman signal strength of a metal slot waveguide is approximately 30 times larger as compared to that using a 0.9 NA objective. This is attributed to the long interaction length of the former case . Also, the SNR (Sig/$\sqrt{BG}$) of the former case is approximately 7 times larger than that of the latter case. This comparison is based on the signal counts that corresponds to 1339 cm^{-1} NTP mode.

6.6.4 Comparison with other on-chip SERS substrates

Here, we numerically compare our hybrid plasmonic waveguide based sensor (HPW) with previously published on-chip surface enhanced Raman sensors, i.e. nanobowties (NB) [28, 35] fabricated using e-beam lithography and nanotriangles (NT) [36] fabricated using nanosphere lithography. The comparison is presented in Table 6.1 in terms of measured Raman conversion efficiency ($\zeta = P_s/P_o$), number of molecules (N_{mol}) excited, resonance behaviour and fabrication technique. The experimental value of ζ for our nanoplasmonic sensor that is extracted for the 1339 cm^{-1} mode

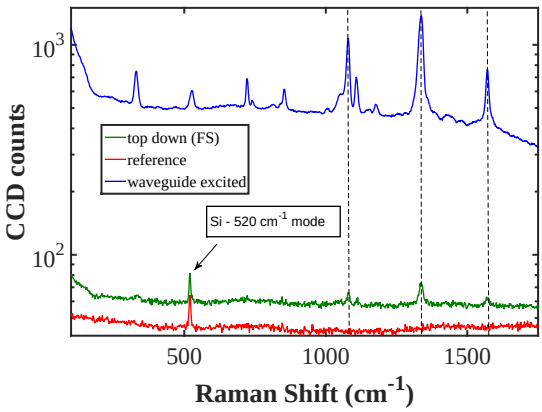

Figure 6.9: The Raman spectra measured through excitation and collection from a metal slot waveguide (blue) and conventional microscope objective (green). All spectra are extracted using same pump power (2 mW) and integration time (60 sec). The black dotted lines show the position of dominant NTP Raman modes. The Raman setup depicted before in chapter 3 (Fig. 3.9) is used for both measurements.

of NTP is (1$\pm$0.057) $\times$ 10^{-9}. This is 3 orders of magnitude higher than that of nanobowties and an order of magnitude higher than nanotriangles. The total number of molecules excited (N_{mol}) in each case is calculated using $A_g \times \rho_g$ where the A_g is the gold surface area and $\rho_g = 4.4 \times 10^6$ molecules/μm^2 [37] is the density of NTP molecules on a gold surface. Another advantage of the reported SERs substrate over others is the ease of fabrication that consists of ALD assisted DUV photolithography, this enables mass scale manufacturing. Next, the broadband nature of SERs enhancement is compared with the other two devices. NB and NT are highly resonant i.e. FWHM of resonant enhancement $\leq$ 100 nm for nanobowties and $\leq$ 250 nm for nanotriangles. Our sensor offers a non-resonant enhancement making the SERs enhancement independent of excited and scattered wavelengths.

6.6.5 Comparison with dielectric waveguide

Here, we numerically compare the signal strength offered by a hybrid plasmonic waveguide (HPW) based sensor with a standard silicon nitride strip and slot (gap= 150 nm) waveguide [9, 38] fabricated using DUV photolithography. Two different cases i.e. a monolayer of NTP and a bulk Isopropyl Alcohol (IPA) cladding are considered. The results are presented

Structures	**NB** [28, 35]	**NT** [36]	**HPW**
$\zeta = P_s/P_o$	$\approx 10^{-12}$	$\approx 10^{-10}$	$(1\pm0.057)10^{-9}$
$\mathbf{N}_{mol}$	$\approx 0.5 \times 10^7$	$\approx 1.5 \times 10^7$	$\approx 8.2 \times 10^7$
Fabrication	e-beam	Nanosphere litho	ALD + Photolitho
FWHM (nm)	≤ 100	≤ 250	non-resonant

Table 6.1: Comparison of hybrid plasmonic waveguide (HPW) sensor with existing nanophotonic SERs substrates i.e. nanobowties (NB) and nanotriangles (NT).

in Table 6.2. In the case of an NTP monolayer, for the sake of comparison, we assume the same NTP Raman cross section ($\sigma = 1.8 \times 10^{-29}$ cm^2/sr) and surface density ($\rho = 4.4 \times 10^6$ molecules/μm^2) for both sensors. However, this is rather an artificial assumption because ρ of a given molecule strongly depends on the surface of the substrate as well as the binding technique. But it serves the purpose of comparing different sensors. For an NTP monolayer, 15 μm long HPW exhibits approximately 14 and 20 times stronger signal as compared to a 4 cm long silicon nitride slot and a 5 cm long strip waveguide. Here, we have considered the coupling loss from an access waveguide to a plasmonic waveguide i.e. γ_p and γ_s are 3.95 and 5.1 dB/facet respectively. Similarly, for a bulk analyte, ζ is computed assuming a 1.5 μm thick IPA as a top cladding (n$_{IPA}$=1.37, $\lambda_p = 785$ nm, $\lambda_s = 840$ nm, $\sigma = 8.0 \times 10^{-31}$ cm^2/sr and $\rho = 7.87 \times 10^{21}$ molecules/cm^3) [9]. Inspite of the high field enhancement offered by a HPW, ζ for the silicon nitride slot waveguide is still approximately 3 times larger than that for a HPW due to the absorption intrinsic to the gold. If we compare the Raman background generated in both kind of sensors we can establish a more relevant benchmarking. In the next section, the Raman background of metal slot waveguide is compared with Si_3N_4 strip and slot waveguide.

6.7 Bulk sensing

SERS substrates are known for their high signal enhancement for the adsorbed analyte because of their huge field enhancement at the surface. In the case of metal slot waveguide, the geometry is good enough to probe volume of liquids.

To analyze the SERS performance for a bulk analyte, experiments are performed using liquid isopropyl alcohol. A pump power of 1 mW after objective and 1 sec integration time is used. The length of the plasmonic waveguide is L$_p$ = 100μm. The results are shown in Fig. 6.10. Five dif-

Structures	$\zeta = P_s/P_o$	Effective length
Metal slot	$\mathbf{1.0}\times10^{-9}$	≈ 15 μm
	1.2×10^{-10}	
Si_3N_4 slot	$\mathbf{7.0}\times10^{-11}$	≈ 4 cm
	3.4×10^{-10}	
Si_3N_4 strip	$\mathbf{5.0}\times10^{-11}$	≈ 5 cm
	1.1×10^{-10}	

Table 6.2: Comparison of a hybrid plasmonic waveguide (HPW) sensor with a Si_3N_4 strip and slot waveguide for an NTP monolayer (bold) and for a bulk Isopropyl Alcohol cladding (plain).

ferent access waveguide lengths are taken in account to analyze the background contribution from Si_3N_4 and gold. As shown in Fig. 6.10, overall Raman background does not change as the access waveguide length gets smaller than 60 μm i.e. $L_a \leq 60$ μm. That is the waveguide length when the plasmonic waveguide background becomes dominant over the Si_3N_4. In the next set of experiments, the signal and background strength of a plasmonic waveguide is compared with PECVD Si_3N_4 strip and slot waveguides. For the plasmonic waveguide, an access waveguide of 60 μm is used to avoid any extra Si_3N_4 background. For Si_3N_4 strip and slot waveguides, a 2 cm long waveguide is used. All measurements are done using 1 mW pump power after objective and 1 sec integration time. The results are shown in Fig. 6.11.a. The signal strength (Sig) is defined as the counts at 819 cm^{-1}. Similarly, the Raman background (BG) is defined as the counts at 819 cm^{-1} (where the background is flat). As shown in Fig. 6.11.b, the relative signal strength i.e $Sig_{Si_3N_4 slot}$/$Sig_{metal slot} \approx 11.5$ and $Sig_{Si_3N_4 strip}$/$Sig_{metal slot} \approx 4.2$. The ratio $Sig_{Si_3N_4 slot}$/$Sig_{metal slot}$ is approximately 3.8 times higher than what is simulated in Table 6.2. This variation might be attributed to the fact that IPA could not completely wet the narrow gap ($\approx$ 15 nm) of metal slot waveguide. Also, the hydrophobic nature of the metallic surface may inhibit full wetting. The ratio $Sig_{Si_3N_4 slot}$/$Sig_{Si_3N_4 strip}$ corresponds well to the simulated values mentioned in Table. 6.2. On the other hand, ζ_i=$Sig_i/\sqrt{BG_i}$ for the metal slot, Si_3N_4 slot and Si_3N_4 strip waveguide are approximately 5.0, 5.2 and 17.3, respectively. This shows that, in spite of bad wettability, the signal-to-noise ratio of metal slot waveguide is comparable to that of a Si_3N_4 strip waveguide and $\approx$ 3 times smaller than that for a Si_3N_4 slot waveguide. The wettability of ultra small metallic gaps can be improved by applying different wetting techniques e.g. application of O_2 plasma before immersion [39] or two components droplets technique based on solutal Marangoni effect [40].

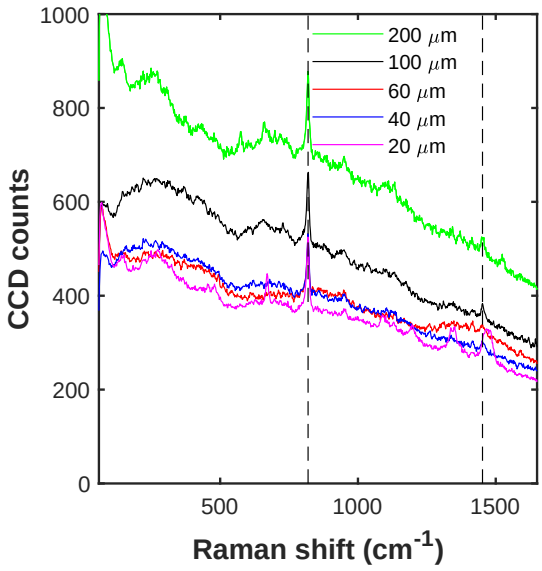

Figure 6.10: The Raman spectra of iso-propyl alcohol (IPA) measured through excitation and collection from a metal slot waveguide for various access waveguide lengths. All spectra are extracted using same pump power (1 mW) and integration time (1 sec). The black dotted lines show the position of dominant ethanol Raman modes.

It is worth mentioning that the analysis presented in this section is based on 1 mW pump power (P_p) before objective. However, unlike metal waveguide, Si_3N_4 waveguide can withstand high pump powers ($>$ 50 mW). This will further improve the signal to noise ratio as SNR $\propto \sqrt{P_p}$.

(a)

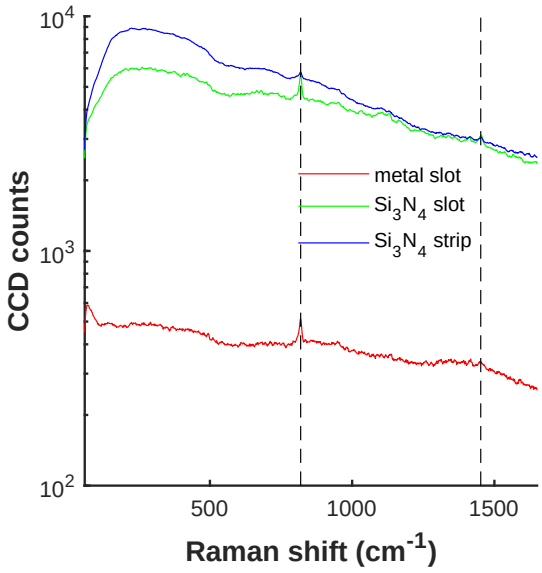

(b)

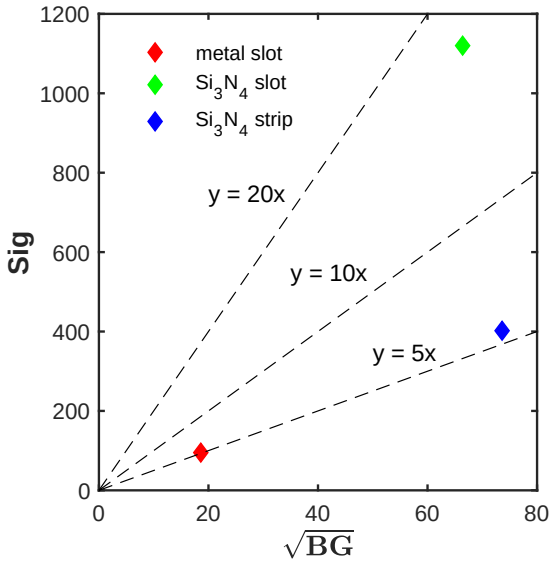

Figure 6.11: a) The Raman spectra of iso-propyl alcohol (IPA) measured through excitation and collection from a metal slot (red), Si_3N_4 slot (green) and Si_3N_4 slot waveguide. All spectra are extracted using same pump power (1 mW) and integration time (1 sec). The black dotted lines show the position of dominant ethanol Raman modes. b) The signal strength (Sig) at 819 cm^{-1} is plotted against the shot noise associated with Raman background $\sqrt{BG}$.

6.8 ALD grown nanotrenches on Si_3N_4 slot waveguide

Thus far, we presented the SERS performance of a metal waveguide that is fabricated using a continuous metal layer deposited using metal sputtering. Due to the random nature of the sputtering process, the control on the thickness of metal layer is difficult. Also, the metal layer deposited using the sputtering are not very conformal. At the CoCoon Group, Ghent University, a novel ALD process for gold deposition has been developed using Me_3AuPMe_3 and H_2 plasma (20% H_2 in Ar) as the precursor and reactant. Au is deposited with a new ALD process, using Me_3AuPMe_3 and H_2 plasma. For the complete details of the ALD Au process readers are suggested to follow [41]. The process leads to the formation of nanotrenches where the width of the nanotrenches can be tuned by controlling the growth rate. In this section, we present an on-chip Raman sensor that uses plasmonic nanotrenches directly defined on a single mode silicon nitride Si_3N_4 slot waveguide using atomic layer deposition. Highly conformal ALD of Al_2O_3 and Au allows defining the nanotrenches in a more controlled and uniform fashion all along the waveguide width and length. The SERS performance of the resulting sensor is characterized using a monolayer of 4-nitrothiophenol.

6.8.1 Fabrication

The sensor is fabricated in three steps. In the first step, Si_3N_4 slot waveguides are fabricated using 193 nm optical lithography and subsequently etched by fluorine based inductive coupled plasma-reactive ion-etch process [22] to get the final structure as depicted in Fig. 6.4. Then a layer of Al_2O_3 is deposited using ALD. Finally, a 100 μm window is defined in AZ 5214 photo-resist using DUV lithography followed by an ALD deposition of gold layer. A home built ALD reactor with a base pressure of 2×10^{-6} mbar is used to deposit the Al_2O_3 and Au layers [23]. Both layers are deposited at a substrate temperature of 100°C. The Al_2O_3 layer is deposited using TMA and H_2O as the precursor and reactant, respectively. The used pressure for both gases is $6x10^{-3}$ mbar. Au is deposited with a new ALD process, using Me_3AuPMe_3 and H_2 plasma (20% H_2 in Ar) as the precursor and reactant. A pressure of 1 mbar is used for the Au reactant and $6x10^{-3}$ mbar for the hydrogen gas.

(a)

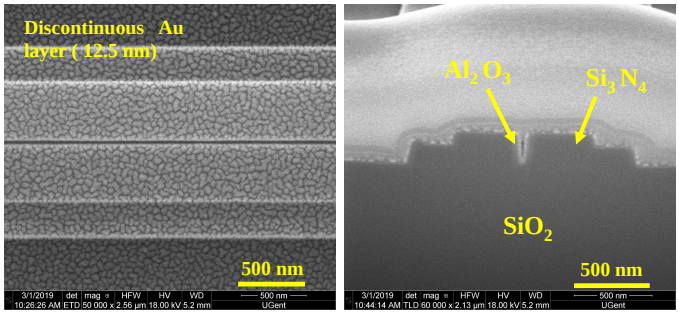

(b)

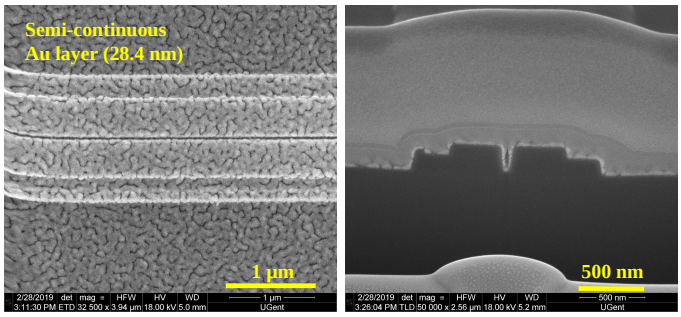

(c)

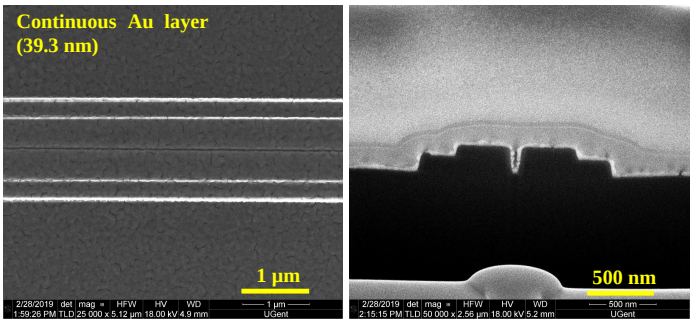

Figure 6.12: The SEM images of the fabricated on-chip SERS device using ALD gold. a) for 12.5 nm gold, b) for 28.4 nm gold and for 39.3 nm gold.

After the patterning, the chip was thoroughly cleaned with Acetone/I-PA/DI water and dried with N_2 gun. For the monolayer coating, the chip was immersed in 1 mM solution of 4-Nitrophenol (pNTP) in ethanol. Finally chips are cleaved such that the access waveguide length is $\leq 60\ \mu m$. Three different thicknesses of the gold (t_{gold}) are considered i.e. the average thickness 12.5$\pm$2.4 nm (where the gold layer is discontinuous), 28.4$\pm$4.5 nm (where the gold layer is semi-continuous) and 39.3$\pm$5.8 nm (continuous layer). The sem images are shown in Fig. 6.12. Also in order to keep a same slot width, three different Al_2O_3 layer thicknesses ($t_{Al_2O_3}$) are considered. For example 39 nm, 49 nm and 59 nm ALD Al_2O_3 layer thicknesses are used for 12.5, 28.4 and 39.3 nm thick gold layers.

6.8.2 Experimental results

Raman measurements are done using the same setup as mentioned in chapter 3 (Fig. 3.9). A pump power of 1 mW and 1 sec integration time is used. NTP spectra measured from three different metal waveguides are shown in Fig. 6.13. The measured spectrum contains all the pNTP Raman modes. Two waveguides on the same chip are measured. NTP spectra with dashed lines represent the identical waveguide on same chip. The plasmonic waveguide for the thinner gold layer i.e. t_{gold} = 12.5 nm shows remarkably high SERS signal strength. For the integrated counts at 1339 cm^{-1} (dominant NTP mode), the signal strength for t_{gold} = 12.5 nm is approximately 1.8 and 15 times stronger as compared to the metal waveguide with 28.4 and 39.3 nm thick gold layer, respectively.

In order to investigate this large variation, SEM images were taken close to the metal layer. As shown in Fig. 6.14.a, the 12.5 nm thick gold layer shows a continuous array of 10 nm wide nanotrenches all along the waveguide cross section. These nanotrenches induce closely packed and highly localized hot spots all along the length of the waveguide. These localized hot spots lead to the resonance dependent high field enhancement that eventually boosts the SERS signal. On the other hand, the thicker ALD gold layer (t_{gold} = 39.3 nm) shows rather continuous gold layer that is comparable to the one deposited using the sputtering. In order to verify the presence of hotspots, we tried to observe the resonant enhancement. Transmission measurements are done to extract the extinction spectrum. The measurements are done using a broadband light source. A 10 μm long plasmonic waveguide is integrated with a 5 mm long access waveguide. As defined before in Eq. 5.6, the normalized extinction (e_λ) is defined as

$$e_\lambda[dB] = T_{ref}(\lambda)[dB] - T_{gold}(\lambda)[dB] \tag{6.2}$$

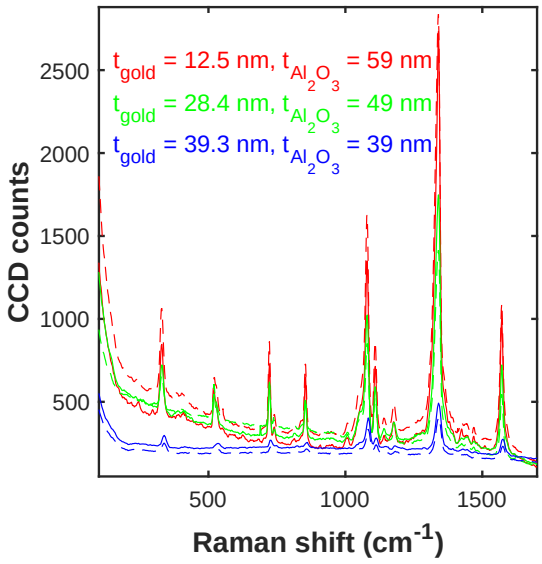

Figure 6.13: The back-scattered SERS signal of NTP measured from plasmonic slot waveguide of $t_{Al_2O_3}$ = 59 nm/t_{gold} = 12.5 nm (red), $t_{Al_2O_3}$ = 48 nm / t_{gold} = 28.4 nm (green) and $t_{Al_2O_3}$ = 39 nm / t_{gold} = 39.3 nm (blue) . All spectra are extracted using same pump power (1 mW) and integration time (1 sec). The dotted lines shows a back-scattered SERS signal of NTP measured from another waveguide on the same chip.

where T_{ref} and T_{gold} are the transmission in a reference (no gold) and a functionalized waveguide (with ALD gold). The measured (e_λ)[dB] is shown in Fig. 6.14.b. The black and green dotted lines represent the position of the pump and Stokes wavelength i.e. λ_p = 785 nm and λ_S = 877 nm. The extinction spectrum recorded from the metal waveguide with t_{gold}=12.5 nm shows the resonance where the resonance wavelength (λ_{res}) is around 950 nm. On the other hand, extinction spectrum recorded from metal waveguide with t_{gold}=39.5 nm is relatively flat. This resonance enhancement is seen before in the case of nanobowties and arch dipole antennas where extinction spectrum shows a peak at λ_{res}. This corresponds to the localized surface plasmon mode of nanoantennas. Here, the localized mode of plasmonic nanotrenches exhibits the resonance enhancement.

(a)

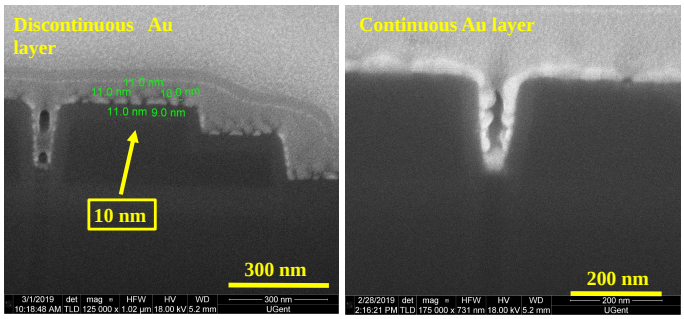

(b)

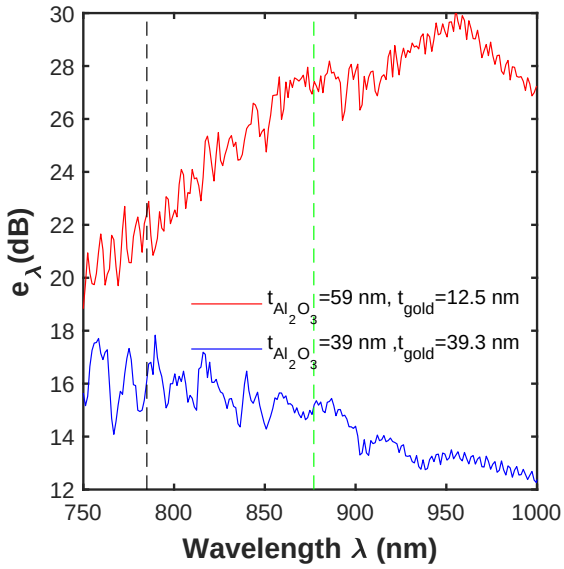

Figure 6.14: a) The SEM images of the fabricated on-chip SERS device using ALD gold (for 12.5 nm gold and 39.3 nm gold thickness). 12.5 nm thick ALD gold layer shows the formation of 10 nm wide nanotrenches along the waveguide. b) The extinction spectra measured from ALD gold coated waveguides. The extinction spectrum measured from plasmonic waveguide with an ALD gold thickness of 12.5 nm(red) shows the resonance behaviour i.e. $\lambda_{res} \approx 950$ nm. Black and green dotted lines shows the position of pump and Stokes wavelength i.e. λ_p=785 nm and λ_S=877 nm.

Next, we extract the Stokes to pump conversion efficiency ζ=P_s/P_p. ζ is extracted using 1 mW pump power, 1 sec integration time and experimental factor C_{ext} introduced before in Chapter 5 i.e. $\zeta_{12.5nmgold}$ = (2.3 $\pm$ 0.96) $\times$ 10^{-8}, $\zeta_{28.4nmgold}$ = (1.03 $\pm$ 0.63) $\times$ 10^{-8} and $\zeta_{39.3nmgold}$ = (0.95 $\pm$ 0.3) $\times$ 10^{-9}. Note that, when the ALD gold layer is thicker then it becomes uniform, therefore, ζ converges to the value obtained before using a uniform layer of gold via sputtering i.e. ζ = (1.0 $\pm$ 0.057) $\times$ 10^{-9}.

These preliminary results show that 10 nm wide nanotrenches are deposited on the Si_3N_4 slot waveguide without any patterning technique. Also, the overall SERS signal strength is at least 15 times larger than in the case of a plasmonic waveguide fabricated using conventional sputtered gold. However, as shown in Fig. 6.14.b, the localized plasmon resonance λ_{res} is not optimized for 785 nm pump and 877 nm Stokes wavelength. Ideally, λ_{res} should reside between 785 nm and 877 nm for high field enhancement. Therefore, further experimental investigation is needed to analyze the full potential of these fabrication-less plasmonic nanotrenches directly grown on Si_3N_4 slot waveguide. Also, the power handling capability of the sensor needs to be investigated. Similarly, reproducibility of SERS signal also needs to be analyzed from chip to chip as well from run to run.

In this work, we have not done any analytical estimation of ζ=P_s/P_p. Because of a random distribution of ALD gold patches, it is challenging to define an identical gold layer in the simulation software e.g. in Lumerical FDTD. One way is to do the image processing of SEM image and make a distribution of gold patches size. And then assume a continuous layer of the average patch size in Lumerical. This will give a good estimation of ζ=P_s/P_p.

6.9 Comparison with the free space excited SERS substrate

In chapter 4, we discussed different free space excited SERS substrates that offer high SERS enhancement, hence provide high sensitivity. Comparing the electric field enhancement of SERS substrate is always challenging as it depends on many factors i.e. the definition of figure of merit or enhancement factor, material, analyte, number of molecules, excitation wavelength and optics used in the setup etc [42]. Two commonly used enhancement factors are single molecule enhancement factor (SMEF) also know as localized enhancement factor and SERS substrate enhancement factor (SSEF) also known as average enhancement factor [43]. SMEF is calculated at maximum electric field position that varies from structure to structure. On

the other hand, SSEF considers an average SERS enhancement. A complete guide about how to measure SSEF can be read from [43, 44]. There always exist discrepancies when it comes to the SERS substrate's comparison. Most of the time SERS comparison is benchmarked against Klarite (commercial SERS substrate). However, there are multiple SSEF values of Klarite reported in literature i.e 1.5×10^4 [45] to 3.5×10^6 [46]. Therefore, great care needs to be taken while comparing SERS substrates.

Unlike free space SERS substrates, on-chip SERS substrates lack a reference spontaneous Raman signal that can be used to normalized on-chip Raman signal. Therefore, it is difficult to define a common figure of merit e.g. SSEF. Nevertheless, here we compare different on-chip SERS substrates with the free space SERS substrate in terms of Stokes to pump conversion efficiency. Previously, in Table. 6.1, we compared the pump to Stokes conversion efficiency of on-chip SERS substrates for the 1339 cm^{-1} NTP mode. We compare these on-chip SERS substrates with free space excited gold nanodomes fabricated using nanosphere lithography [7]. Gold nanodome platform was chosen based on its high SSEF = 9.8×10^6 [20] that is comparable to other states of the art reproducible and scalable SERS platforms [47]. To make a fair comparison, the same gold deposition (sputtering) and analyte (NTP monolayer) is used. Also, to minimize the Raman background contribution of Si_3N_4 access waveguide, the waveguide length is limited to 100 μm. Results are shown in Fig. 6.15. The vertical and horizontal axis represents normalized Stokes and Raman background signal strength, respectively. For the waveguide excited plasmonic structures, P_p represents the pump power guided into the access waveguide. For free space excited nanodomes, P_p represents the pump power after the microscope objective. Clearly, for gold nanodomes (gap = 12 nm) normalized Stokes power is about 2 orders of magnitude stronger than a metal slot waveguide (gap = 15 nm). Also, gold nanodomes exhibit a much stronger Raman background ($\approx \times$ 20) as compared to the metal slot waveguide. Among all on-chip SERS sensors, ALD gold slot waveguide gives the highest pump to Stokes conversion efficiency. That is still off by a factor of 4-5 as compared to free space excited nanodomes.

In the end, it is worth mentioning that there also exist other free space SERS substrates that offer even higher SERS enhancement. Therefore, the results presented in this section cannot be generalized to all SERS substrates. To have an overview about other efficient SERS substrates, readers are directed to [48].

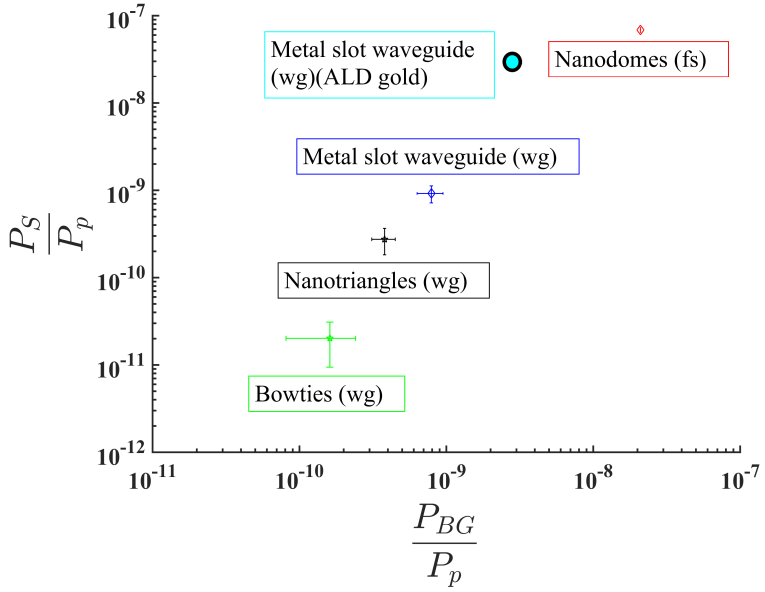

Figure 6.15: Comparison of SERS background power P_{BG} (x-axis) and SERS Stokes power P_S (y-axis) of different SERS platforms. Both parameters are normalized on the input power and the integration time. For the waveguide excited plasmonic structures P_P represents the pump power guided into the access waveguide. For free space excited nanodomes, P_p represents the pump power after the microscope objective. "fs" indicates free-space and "wg" is the waveguide-based excitation and collection of the SERS signal. The figure is adapted from [49]. Blue circle represents the SERS signal and Raman background of an ALD gold slot waveguide.

6.10 Conclusion

In conclusion, we have reported a SERS sensor suitable for on-chip integrated Raman spectroscopy, fabricated using ALD assisted DUV lithography and therefore compatible with back-end CMOS fabrication. We have reported both experimental and numerical characterization of our sensor demonstrating capabilities that have so far been difficult to combine in a single sensor: 1) a large Raman conversion efficiency ($\approx 1\times10^{-9}$) thanks to simultaneous long interaction length, high confinement and plasmonic enhancement (SMEF = 1.5×10^7), 2) a low background due to the reduced overlap of the field with the core of the waveguide 3) a good reproducibility of the Raman spectra (RSD $< 5\%$) across different chips thanks to the

nanometer fabrication accuracy provided by atomic layer deposition, 4) a good tolerance to rather large input power due to a moderate local field enhancement and 5) a broadband enhancement thanks to the use of propagating plasmons rather than localized plasmon (nanoantennae). All these features make this kind of sensor ideal for the future integration with lasers, spectrometers, spectral filters and detectors that will constitute a fully integrated Raman spectrometer chip. Given the compactness of our plasmonic sensor and the other elements, it is easy to foresee a chip capable of containing dozens or hundreds of sensors for performing multiplexed Raman sensing. Furthermore, we have also reported a SERS sensor for an on-chip Raman spectroscopy using a novel ALD process of gold. Me_3AuPMe_3 and H_2 plasma are used as the precursor and reactant, respectively. The formation of 10 nm wide nanotrenches along the width and length of the Si_3N_4 slot waveguide leads to a large pump to Stokes conversion efficiency of (2.3 $\pm$ 0.96) $\times$ 10^{-8}. This is the highest on-chip pump to Stokes conversion efficiency known to the date. However, further experimental investigation is needed to analyze the full potential of these fabrication-less plasmonic nanotrenches directly grown on Si_3N_4 slot waveguide. Similarly, reproducibility of SERS signal is also needed to be characterized at chip to chip as well run to run level.

References

[1] Yun-Feng Xiao, Yong-Chun Liu, Bei-Bei Li, You-Ling Chen, Yan Li, and Qihuang Gong. *Strongly enhanced light-matter interaction in a hybrid photonic-plasmonic resonator*. Phys. Rev. A, 85:031805, Mar 2012.

[2] Parinda Vasa and Christoph Lienau. *Strong LightMatter Interaction in Quantum Emitter/Metal Hybrid Nanostructures*. ACS Photonics, 5(1):2–23, 2018.

[3] Jon A. Schuller, Edward S. Barnard, Wenshan Cai, Young Chul Jun, Justin S. White, and Mark L. Brongersma. *Plasmonics for extreme light concentration and manipulation*. Nature Materials, 9(22):193–204, Feb 2010.

[4] Swati Tanwar, Krishna Kanta Haldar, and Tapasi Sen. *DNA Origami Directed Au Nanostar Dimers for Single-Molecule Surface-Enhanced Raman Scattering*. Journal of the American Chemical Society, 139(48):17639–17648, 2017. PMID: 29129049.

[5] Alan X. Wang and Xianming Kong. *Review of Recent Progress of Plasmonic Materials and Nano-Structures for Surface-Enhanced Raman Scattering*. Materials, 8(6):3024–3052, 2015.

[6] Bi-Shen Lee, Ding-Zheng Lin, and Ta-Jen Yen. *A Low-cost, Highly-stable Surface Enhanced Raman Scattering Substrate by Si Nanowire Arrays Decorated with Au Nanoparticles and Au Backplate*. Scientific Reports, 7(1):4604, 2017.

[7] Pieter C Wuytens, Ananth Z Subramanian, Winnok H De Vos, Andre G Skirtach, and Roel Baets. *Gold nanodome-patterned microchips for intracellular surface-enhanced Raman spectroscopy*. Analyst, 140(24):8080–8087, 2015.

[8] Y. C. Jun, R. D. Kekatpure, J. S. White, and M. L. Brongersma. *Nonresonant enhancement of spontaneous emission in metal-dielectric-metal plasmon waveguide structures*. Phys. Rev. B, 78:153111, Oct 2008.

[9] Ashim Dhakal, Ali Raza, Frédéric Peyskens, Ananth Z. Subramanian, Stéphane Clemmen, Nicolas Le Thomas, and Roel Baets. *Efficiency of evanescent excitation and collection of spontaneous Raman scattering near high index contrast channel waveguides*. Opt. Express, 23(21):27391–27404, Oct 2015.

[10] Herman MK Wong, Mohsen Kamandar Dezfouli, Lu Sun, Stephen Hughes, and Amr S Helmy. *Nanoscale plasmonic slot waveguides for enhanced Raman spectroscopy*. Physical Review B, 98(8):085124, 2018.

[11] G. Veronis and S. Fan. *Modes of Subwavelength Plasmonic Slot Waveguides*. Journal of Lightwave Technology, 25(9):2511–2521, Sep. 2007.

[12] A. Melikyan, L. Alloatti, A. Muslija, D. Hillerkuss, P. C. Schindler, J. Li, R. Palmer, D. Korn, S. Muehlbrandt, D. Van Thourhout, B. Chen, R. Dinu, M. Sommer, C. Koos, M. Kohl, W. Freude, and J. Leuthold. *High-speed plasmonic phase modulators*. Nature Photonics, 8(8):229–233, 2014.

[13] Yin Huang, Changjun Min, Pouya Dastmalchi, and Georgios Veronis. *Slow-light enhanced subwavelength plasmonic waveguide refractive index sensors*. Optics Express, 23(11):14922–14936, 2015.

[14] Long Chen, Jagat Shakya, and Michal Lipson. *Subwavelength confinement in an integrated metal slot waveguide on silicon*. Optics letters, 31(14):2133–2135, 2006.

[15] Bing Qing Zhu and Hon Ki Tsang. *High coupling efficiency silicon waveguide to metal–insulator–metal waveguide mode converter*. Journal of Lightwave Technology, 34(10):2467–2472, 2016.

[16] Ruoxi Yang, Rami A. Wahsheh, Zhaolin Lu, and Mustafa A. G. Abushagur. *Efficient light coupling between dielectric slot waveguide and plasmonic slot waveguide*. Opt. Lett., 35(5):649–651, Mar 2010.

[17] Deqing Kong and Makoto Tsubokawa. *Evaluation of slot-to-slot coupling between dielectric slot waveguides and metal-insulator-metal slot waveguides*. Optics express, 23(15):19082–19091, 2015.

[18] A. Jakubowicz, H. Jia, R. M. Wallace, and B. E. Gnade. *Adsorption Kinetics of p-Nitrobenzenethiol Self-Assembled Monolayers on a Gold Surface*. Langmuir, 21(3):950–955, 2005. PMID: 15667173.

[19] Fl J García-Vidal and JB Pendry. *Collective theory for surface enhanced Raman scattering*. Physical Review Letters, 77(6):1163, 1996.

[20] Pieter C Wuytens, Hans Demol, Nina Turk, Kris Gevaert, Andre G Skirtach, Mohamed Lamkanfi, and Roel Baets. *Gold nanodome SERS platform for label-free detection of protease activity*. Faraday discussions, 205:345–361, 2017.

[21] Ashim Dhakal, Ali Raza, Frédéric Peyskens, Ananth Z. Subramanian, Stéphane Clemmen, Nicolas Le Thomas, and Roel Baets. *Efficiency of evanescent excitation and collection of spontaneous Raman scattering near high index contrast channel waveguides*. Opt. Express, 23(21):27391–27404, Oct 2015.

[22] A. Z. Subramanian, P. Neutens, A. Dhakal, R. Jansen, T. Claes, X. Rottenberg, F. Peyskens, S. Selvaraja, P. Helin, B. Du Bois, K. Leyssens, S. Severi, P. Deshpande, R. Baets, and P. Van Dorpe. *Low-Loss Singlemode PECVD Silicon Nitride Photonic Wire Waveguides for 532 x2013;900 nm Wavelength Window Fabricated Within a CMOS Pilot Line*. IEEE Photonics Journal, 5(6):2202809–2202809, Dec 2013.

[23] Elisabeth Levrau, Kevin Van de Kerckhove, Kilian Devloo-Casier, Sreeprasanth Pulinthanathu Sree, Johan A Martens, Christophe Detavernier, and Jolien Dendooven. *In Situ IR Spectroscopic Investigation of Alumina ALD on Porous Silica Films: Thermal versus Plasma-Enhanced ALD*. The Journal of Physical Chemistry C, 118(51):29854–29859, 2014.

[24] Robert B Gennis. *Biomembranes: molecular structure and function*. Springer Science & Business Media, 2013.

[25] Edwin Southern, Kalim Mir, and Mikhail Shchepinov. *Molecular interactions on microarrays*. Nature genetics, 21(1s):5, 1999.

[26] Bin Lu, Malcolm R Smyth, and Richard O'Kennedy. *Tutorial review. Oriented immobilization of antibodies and its applications in immunoassays and immunosensors*. Analyst, 121(3):29R–32R, 1996.

[27] Long Chen, Jagat Shakya, and Michal Lipson. *Subwavelength confinement in an integrated metal slot waveguide on silicon*. Opt. Lett., 31(14):2133–2135, Jul 2006.

[28] Frédéric Peyskens, Pieter Wuytens, Ali Raza, Pol Van Dorpe, and Roel Baets. *Waveguide excitation and collection of surface-enhanced Raman scattering from a single plasmonic antenna*. Nanophotonics, 2018.

[29] Jiaqi Li, Chang Chen, Hilde Jans, Xiumei Xu, Niels Verellen, Ingrid Vos, Yasuaki Okumura, Victor V. Moshchalkov, Liesbet Lagae, and Pol Van Dorpe. *300 mm Wafer-level, ultra-dense arrays of Au-capped nanopillars with sub-10 nm gaps as reliable SERS substrates*. Nanoscale, 6:12391–12396, 2014.

[30] Hsin-Yu Wu, Charles J Choi, and Brian T Cunningham. *Plasmonic nanogap-enhanced Raman scattering using a resonant nanodome array*. Small, 8(18):2878–2885, 2012.

[31] Chang Chen, James Andell Hutchison, Pol Van Dorpe, Ronald Kox, Iwijn De Vlaminck, Hiroshi Uji−i, Johan Hofkens, Liesbet Lagae, Guido Maes, and Gustaaf Borghs. *Focusing Plasmons in Nanoslits for SurfaceEnhanced Raman Scattering*. Small, 5(24):2876–2882, 2009.

[32] Mohammadali Tabatabaei, Alexandre Sangar, Nastaran Kazemi−Zanjani, Philippe Torchio, Alexandre Merlen, and Franois

Lagugne−Labarthet. *Optical Properties of Silver and Gold Tetrahedral Nanopyramid Arrays Prepared by Nanosphere Lithography*. The Journal of Physical Chemistry C, 117(28):14778–14786, 2013.

[33] Leilei Kang, Ping Xu, Bin Zhang, Hsinhan Tsai, Xijiang Han, and Hsing-Lin Wang. *Laser wavelength- and power-dependent plasmon-driven chemical reactions monitored using single particle surface enhanced Raman spectroscopy*. Chem. Commun., 49:3389–3391, 2013.

[34] Pieter Wuytens. *Surface-enhanced Raman Spectroscopy for Intracellular Sensing and Protease Activity Detection: from Chip Technology to Applications*. PhD Thesis, Ghent University, 2018.

[35] Frederic Peyskens, Ashim Dhakal, Pol Van Dorpe, Nicolas Le Thomas, and Roel Baets. *Surface Enhanced Raman Spectroscopy Using a Single Mode Nanophotonic-Plasmonic Platform*. ACS Photonics, 3(1):102–108, 2016.

[36] Pieter C. Wuytens, Andre G. Skirtach, and Roel Baets. *On-chip surface-enhanced Raman spectroscopy using nanosphere-lithography patterned antennas on silicon nitride waveguides*. Opt. Express, 25(11):12926–12934, May 2017.

[37] L. Baia, M. Baia, J. Popp, and S. Astilean. *Gold Films Deposited over Regular Arrays of Polystyrene Nanospheres as Highly Effective SERS Substrates from Visible to NIR*. The Journal of Physical Chemistry B, 110(47):23982–23986, 2006. PMID: 17125367.

[38] Ashim Dhakal, Pieter C. Wuytens, Frdric Peyskens, Karolien Jans, Nicolas Le Thomas, and Roel Baets. *Nanophotonic Waveguide Enhanced Raman Spectroscopy of Biological Submonolayers*. ACS Photonics, 3(11):2141–2149, 2016.

[39] DF O'kane and KL Mittal. *Plasma cleaning of metal surfaces*. Journal of Vacuum Science and Technology, 11(3):567–569, 1974.

[40] Chang Chen, XiuMei Xu, Yi Li, Hilde Jans, Pieter Neutens, Sarp Kerman, Guy Vereecke, Frank Holsteyns, Guido Maes, Liesbet Lagae, Tim Stakenborg, and Pol van Dorpe. *Full wetting of plasmonic nanopores through two-component droplets*. Chem. Sci., 6:6564–6571, 2015.

[41] M. V. Daele, M. Griffiths, A. Raza, M. Minjauw, E. Solano, J.-Y. Feng, R. K. Ramachandran, S. Clemmen R. Baets, S. Barry, C. De-

tavernier, and J. Dendooven. *Plasma-enhanced atomic layer deposition of nanostructured gold near room temperature*. ACS Applied Materials Interfaces, 2019.

[42] Roberto Pilot, Raffaella Signorini, Christian Durante, Laura Orian, Manjari Bhamidipati, and Laura Fabris. *A review on surface-enhanced Raman scattering*. Biosensors, 9(2):57, 2019.

[43] Eric Le Ru and Pablo Etchegoin. *Principles of Surface-Enhanced Raman Spectroscopy: and related plasmonic effects*. Elsevier, 2008.

[44] R Pilot and R Bozio. *Validation of SERS enhancement factor measurements*. Journal of Raman Spectroscopy, 49(3):462–471, 2018.

[45] Jiaqi Li, Chang Chen, Hilde Jans, Xiumei Xu, Niels Verellen, Ingrid Vos, Yasuaki Okumura, Victor V Moshchalkov, Liesbet Lagae, and Pol Van Dorpe. *300 mm Wafer-level, ultra-dense arrays of Au-capped nanopillars with sub-10 nm gaps as reliable SERS substrates*. Nanoscale, 6(21):12391–12396, 2014.

[46] Jing Jiang, Zhida Xu, Abid Ameen, Fei Ding, Guohong Lin, and Gang Logan Liu. *Large-area, lithography-free, low-cost SERS sensor with good flexibility and high performance*. Nanotechnology, 27(38):385205, 2016.

[47] Pieter. c. Wuytens. *PhD Thesis: Surface-Enhanced Raman Spectroscopy for Intracellular Sensing and Protease Activity Detection: From Chip Technology to Applications*. Ghent University, October 2017.

[48] Zheng Zeng, Yiyang Liu, and Jianjun Wei. *Recent advances in surface-enhanced raman spectroscopy (SERS): Finite-difference time-domain (FDTD) method for SERS and sensing applications*. TrAC Trends in Analytical Chemistry, 75:162–173, 2016.

[49] Nina Turk, Ali Raza, Pieter Wuytens, Hans Demol, Michiel Van Daele, Christophe Detavernier, Andre Skirtach, Kris Gevaert, and Roel Baets. *Comparison of Free-Space and Waveguide-Based SERS Platforms*. Nanomaterials, 9(10):1401, 2019.

7 Conclusion and future outlook

7.1 Conclusion

In this thesis work, we investigated different modalities of on-chip Raman spectroscopy. Firstly, we presented the bench-marking of four different photonic platforms i.e. Al_2O_3, Si_3N_4, Ta_2O_5 and TiO_2 as potential on-chip Raman spectroscopy platforms. The performance is compared in terms of pump to Stokes conversion efficiency and Raman background generated from the waveguide material. A first comparison is made accounting for the current technological fabrication capability and resulting propagation loss. A more general comparison is made that factors out the loss therefore looking forward at technological improvements. The analysis shows that TiO_2 waveguides exhibit the highest Raman conversion efficiency due to its highest index contrast. However, the signal-to-background ratio is relatively poor due to the high Raman background. On the other hand, Al_2O_3 waveguides exhibit weak Raman background, but the signal collection efficiency suffers due to the low index contrast. Si_3N_4 and Ta_2O_5 strip waveguides seem to be nearly equally good platforms for Raman spectroscopy as their Raman background is rather low but their capability to collect the Raman signal from the analyte is strong. In practice, the loss in Si_3N_4 waveguides being lower than in Ta_2O_5 waveguides, it is presently more advantageous to use Si_3N_4. With the progress in making low loss waveguides, any of the investigated photonic platform could become the best one as long as the

waveguide loss is primarily due to the waveguide itself. In case the loss is dominated by the analyte, the figure of merit given in Table. 3.2 gives a definite answer on what technology is ideal.

In the quest for dielectric waveguides better suited for higher Raman signal collection, we have also studied numerically ALD layer coated PECVD Si_3N_4 slot waveguides. The simulation results for the Stokes to pump conversion efficiency of a 70 nm thick high refractive ALD layer coated Si_3N_4 slot waveguide shows 7.5 times improvement over an uncoated Si_3N_4 slot waveguide. In the end, we briefly compared Raman background of four possible ALD coatings i.e. Al_2O_3, HfO_2, TiO_2 and VO_2, that can be used to coat Si_3N_4 for an efficient NWERS. The Raman background of ALD VO_2 is comparable to TiO_2 that is about 8 times stronger than PECVD Si_3N_4. On the other hand, ALD HfO_2 exhibits moderate Raman background that is comparable with PECVD Si_3N_4.

After the benchmarking study of different photonic platforms for NWERS, we analyzed surface enhanced Raman spectroscopy (SERS) using a nanoplasmonic antenna integrated on a dielectric waveguide. In a first phase, the SERS performance of an integrated arch dipole antenna geometry is analytically compared with the previously reported bowtie antenna. We have shown that the proposed antenna geometry provides at least one order of magnitude higher pump to Stokes conversion efficiency as compared to the previous realization. In the second phase, the effect of PECVD Si_3N_4 Raman background on the SERS signal is analyzed. Using the back-reflection configuration and small PECVD Si_3N_4 access waveguide length, SERS using a single integrated plasmonic antenna is presented. In the end, we demonstrate the SERS using an antenna embedded into the subwavelength gap of a waveguide. The result shows that SERS signal with this antenna configuration is atleast three times stronger than the evanescently excited and collected SERS (an antenna sitting on top of a waveguide).

Then, we introduced an efficient on-chip Raman sensor, in which plasmonic antennas are replaced by metal slot waveguides. Raman spectroscopy using metal waveguide gains both from a strong field enhancement due to the highly confined propagating plasmon polariton gap mode and a limited spurious background, thanks to the limited field overlap with the dielectric material. Moreover, the fabrication avoids any use of electron beam lithography and rather relies on the atomic layer deposition (ALD) to create the nanometer scale gaps required for a large plasmonic enhancement. Unlike plasmonic nanoantenna, this plasmonic slot waveguide offers few micrometers long interaction length and an off-resonant enhancement hence a broadband Raman conversion efficiency. We have reported both experimental and numerical characterization of our sensor demonstrating capa-

bilities that have so far been difficult to combine in a single sensor: 1) a large Raman conversion efficiency ($\approx 1\times10^{-9}$) thanks to simultaneous long interaction length, high confinement and plasmonic enhancement, 2) a low Raman background due to the reduced overlap of the field with the core of the waveguide 3) a good reproducibility of the Raman spectra (RSD $< 5\%$) across different chips thanks to the nanometer fabrication accuracy provided by atomic layer deposition, 4) a good tolerance to rather large input power due to a moderate local field enhancement and 5) a broadband enhancement thanks to the use of propagating plasmons rather than localized plasmon (nanoantennae). All these features make this kind of sensor ideal for the future integration with lasers, spectrometers, spectral filters and detectors that will constitute a fully integrated Raman spectrometer chip. Given the compactness of our plasmonic sensor and the other elements, it is easy to foresee a chip capable of containing dozens or hundreds of sensors for performing multiplexed Raman sensing.

Furthermore, we have also reported a SERS sensor for on-chip Raman spectroscopy using a novel ALD process of gold. Me_3AuPMe_3 and H_2 plasma are used as the precursor and reactant, respectively. The formation of 10 nm wide nanotrenches along the width and length of the Si_3N_4 slot waveguide leads to a large pump to Stokes conversion efficiency of (2.3 $\pm$ 0.96) $\times$ 10^{-8}. This is the highest on-chip pump to Stokes conversion efficiency known to the date. However, this work is preliminary and further investigation is needed to verify other features of an on-chip Raman sensor e.g. reproducibilty of SERS signal.

7.2 Future outlook

In this section, different future directions that came out of this work are highlighted.

7.2.1 SERS Signal enhancement

7.2.1.1 Optimization of ALD gold nanotrenches directly grown on Si_3N_4 slot waveguide

The preliminary result of ALD nanotrenches directly grown on Si_3N_4 slot waveguide shows huge impact in terms of pump to Stokes conversion efficiency (P_s/P_p). These results also show that sub-10 nm wide nanotrenches can be grown in a narrow Si_3N_4 slot waveguide without using any lithography technique. However, further experimental investigation is needed to analyze the full potential of these fabrication-less ALD grown nanotrenches. Similarly, reproducibility of SERS signal is also needed to be characterized at chip to chip as well run to run level.

Also, in this work, we have not done any analytical estimation of P_s/P_p. Because of a random distribution of ALD gold patches, it is challenging to define an identical gold layer in the simulation software e.g. in Lumerical FDTD. One way is to do an image processing of SEM image and make a distribution of the gold patch size. And then assume a continuous layer of the average patch size in Lumerical. This will give a good estimation of P_s/P_p.

7.2.2 Background mitigation techniques

7.2.2.1 Top down excitation technique

The Raman background generated from access Si_3N_4 waveguide can also be mitigated by exciting a plasmonic resonant mode in a metal slot waveguide using a top down pump injection technique, whereby, the access waveguide is only used to collect the Stokes signal. The fundamental longitudinal mode in a metal slot structure can be excited by adjusting the height and gap of the slot. Also, this technique offers a high extinction of the pump light thus relaxes the stringent requirement on an on-chip rejection filter. This route is the subject of another ongoing PhD project.

7.2.2.2 MMI based Raman background mitigation technique

In this thesis, the back reflection configuration is used to collect the back-scattered SERS signal. However, the integration with other photonic func-

tionalities demands a separate path for the pump power (input) and Stokes signal (output). A device based on multi-mode interference (MMI) can be employed in this regard. An MMI device is a waveguide designed to support multiple modes [1]. Based on the interference of these guided modes, a N $\times$ M power splitter can be designed where N and M are the number of ports at input and output facet, respectively. The schematic of a 2 $\times$ 2 MMI device is depicted in Fig. 7.1. Using this scheme, the path of input pump power (and the Raman background associated to the input waveguide) and back scattered Stokes signal can be decoupled and output port can be connected to other photonic functionalities e.g. a rejection filter to remove the Rayleigh line. This configuration may also lead to high SNR as the port 2 (output port) will only receive a weak pump power that is equal to $P_p(R_{S1}T_{13}T_{32}+R_{S2}T_{14}T_{42}+BG_f)$ in the MMI slab region where T_{ab} is the transmission from a to b port. R_{S1} and R_{S2} are the reflection of pump light from sensor 1 and 2, respectively. And BG_f is the Raman background generated in slab region due to the forward propagating pump light. By reducing the reflection R_S, the total background collected in the output port can be minimized.

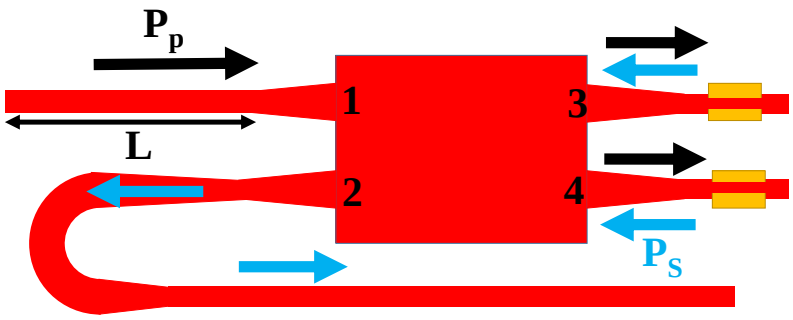

Figure 7.1: 2 $\times$ 2 MMI based on-chip configuration to collect the back scattered SERS signal. Port 1 is used for input pump light. Port 3 and 4 are connected to metal slot waveguides (SERS sensor). And port 2 is the output port and can be connected to other photonic components.

7.2.3 Biological applications: on chip enzymatic study of peptides

All experiments done in this work were based on 4-nitrothiophenol(NTP) monolayer that selectively binds to the gold surface using gold-thiol bond. NTP is an organic molecule that has a high Raman cross-section and was used to characterize the SERS sensor. However, the pump to Stokes conversion efficiency acquired using metal slot waveguide is large enough to also detect biomolecules that typically have Raman cross-sections at least two orders of magnitude lower than NTP. Therefore, it is wise to explore other, biologically relevant analytes. One of the key applications in this regard is the on-chip SERS analysis of proteases. Proteases are enzymes that catalyse the hydrolysis of peptide bonds and which, amongst others, play important roles in various human diseases [2, 3]. Turk et al, recently demonstrated that the SERS signal of the aromatic amino acids in peptides can be detected using the proposed metal slot waveguide [4]. Similarly, other biologically relevant processes i.e. Tyrosine phosphorylation [5] and multiplexed protease activity [6] analysis can also be studied on a chip using proposed SERS sensors.

References

[1] Lucas B Soldano and Erik CM Pennings. *Optical multi-mode interference devices based on self-imaging: principles and applications*. Journal of lightwave technology, 13(4):615–627, 1995.

[2] Marcin Drag and Guy S Salvesen. *Emerging principles in protease-based drug discovery*. Nature reviews Drug discovery, 9(9):690, 2010.

[3] Pieter C Wuytens, Ananth Z Subramanian, Winnok H De Vos, Andre G Skirtach, and Roel Baets. *Gold nanodome-patterned microchips for intracellular surface-enhanced Raman spectroscopy*. Analyst, 140(24):8080–8087, 2015.

[4] Nina Turk, Ali Raza, Pieter Wuytens, Hans Demol, Andre Skirtach, Kris Gevaert, and Roel Baets. *Towards SERS-based on-chip detection of protease activity using nanoplasmonic slot waveguides*. In 23rd Annual symposium of the IEEE Photonics Benelux Chapter, 2018.

[5] Wei-Qing Wang, Jin-Peng Sun, and Zhong-Yin Zhang. *An overview of the protein tyrosine phosphatase superfamily*. Current topics in medicinal chemistry, 3(7):739–748, 2003.

[6] Urja S Lathia, Olga Ornatsky, Vladimir Baranov, and Mark Nitz. *Multiplexed protease assays using element-tagged substrates*. Analytical biochemistry, 408(1):157–159, 2011.

A

Raman background of two differently processed TiO_2 waveguides

To validate the huge Raman background generated from the titania waveguides, Raman background from two differently processed TiO_2 chips i.e. sample 1 and sample 2 are measured and compared. Sample 1 (same as used in chapter 3) is fabricated at University of Cornell, USA (Group of Prof. Jin Suntivich). And sample 2 is fabricated at University of Twente, The Netherlands (Group of Dr. Sonia Blanco). Fabrication details and results are mentioned below.

A.1 Fabrication details

To fabricate sample 1, TiO_2 film is deposited on a thermal oxidized silicon wafer by reactive sputtering. Next, a bilayer stack of anti-reflective coating and UV$-$210 photoresist were applied on the wafer. Then, the patterns are defined by a deep-ultraviolet stepper (λ =248 nm) and transferred under C_4F_6 plasma etching with He cooling. The final waveguide has a cross section (w $\times$ height) of 380 $\times$ 180 nm^2.

The second TiO_2 chip (Sample 2) is fabricated with the different process parameters. A 100 nm thick TiO_2 layer is deposited using RF sputtering with the following parameters: 20 °C temperature, 6 $\times$ 10^{-3} mbar process pressure, 34 sccm Ar flow, 7.5 sccm O_2 flow and 500 W source power.

After an e-beam exposure and resist development, the TiO_2 is etched using the reactive ion etching in an Oxford PlasmaPro 100 Cobra. The final waveguide has a cross section (w $\times$ height) of 1000×100 nm^2.

A.2 Results and discussion

Due to different waveguide cross sections of sample 1 and sample 2, a fair comparison of Raman background demands the normalization with background conversion efficiency (η_{BG}) and coupling efficiency. As defined before in chapter 3 (Eq. 3.4), η_{BG} is given as

$$\eta(\mathrm{w},\mathrm{h},\lambda_p,\lambda_s) = \frac{n_g^2\lambda_s^2}{n}\iint \frac{\epsilon|\mathbf{E}(\mathbf{r},\lambda_\mathbf{p})|^\mathbf{2}}{\iint \epsilon|\mathbf{E}(\mathbf{r},\lambda_\mathbf{p})|^\mathbf{2}\mathrm{d}\mathbf{r}}\frac{1}{\mathbf{A_{eff}}(\mathbf{r},\lambda_\mathbf{s})}\mathrm{d}\mathbf{r} \qquad \text{(A.1)}$$

where unlike analyte signal conversion efficiency η_A, the outer integral in Eq. A.1 runs over the waveguide cross section to estimate η_{BG}. Figure. A.1.a shows η_{BG} for sample 1 and sample 2 in the Raman shift span of $0-1600$ cm^{-1}. Figure. A.1.b shows the normalized Raman spectra of sample 1 and sample 2. Both spectra were acquired with 0.25 sec integration time and 10 mW pump power at 785 nm wavelength. As shown in Fig. A.1. b, for the same input pump power, both spectra are remarkably aligned well with each other in terms of the spectral features. This result shows that two differently processed TiO_2 chips lead to the same Raman background. Note that the processing temperature in both TiO_2 chips is kept less than TiO_2 crystallization temperature. A high$-$temperature growth of TiO_2 layers leads to the crystallization [1] that eventually changes the Raman background.

References

[1] Qi Xie, Jan Musschoot, Davy Deduytsche, Roland L Van Meirhaeghe, Christophe Detavernier, Sven Van den Berghe, Yu-Long Jiang, Guo-Ping Ru, Bing-Zong Li, and Xin-Ping Qu. *Growth kinetics and crystallization behavior of TiO_2 films prepared by plasma enhanced atomic layer deposition*. Journal of The Electrochemical Society, 155(9):H688–H692, 2008.

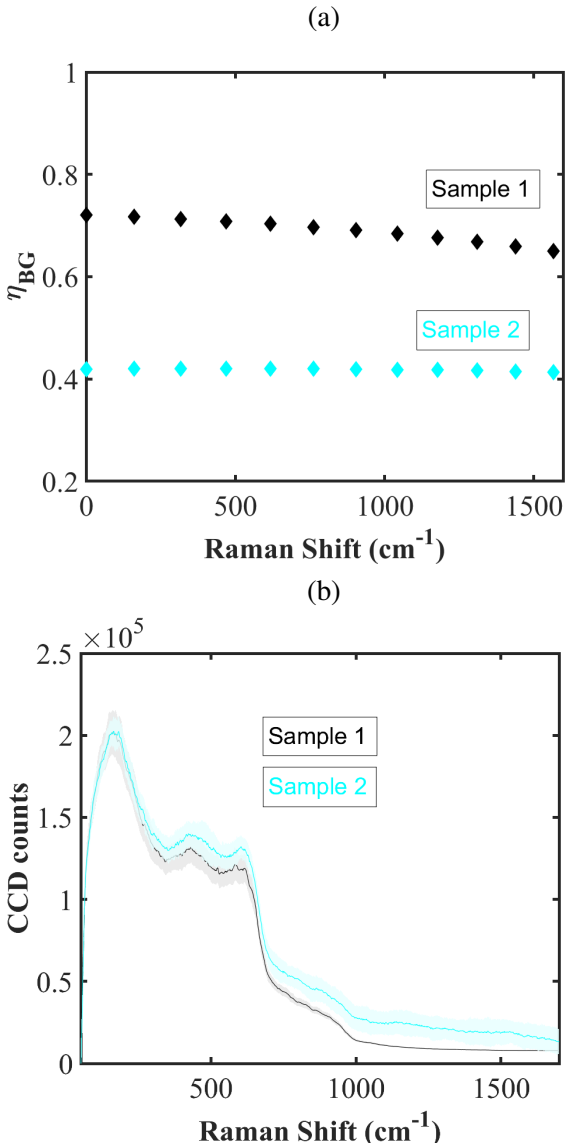

Figure A.1: a) The η_{BG} calculated using Eq. A.1. A 785 nm pump wavelength is assumed. b) The Raman background comparison of two differently processed TiO_2 waveguides. For the same input pump power (10 mW) and integration time (t=0.25 sec), both spectra are remarkably aligned well with each other in terms of the spectral features

B

CCD Counts to Stokes power conversion

In order to correlate the Stokes power at the input facet (in a back-reflection configuration) of the chip and the actual detected signal in counts per unit time (C/sec), we need to take into account all optical losses in our setup. The Stokes power reaching the detector surface is given by

$$P_{DS} = \gamma_{in} \times \gamma_{out} \times T_{MO} \times T_{spec} \times FOM \times P_o \tag{B.1}$$

where T_{MO} and T_{spec} are transmissions through microscope optics (filter, dischoric mirror etc.) and spectrometer (transmission through diffraction grating and input slit), respectively. Transmission values are T_{MO} = 0.65 and T_{spec} = 0.6 (based on the data provide by supplier).γ_{in} and γ_{out} are coupling efficiencies from microscope objective to the waveguide. where FOM is same as defined in Eq. 3.6):

$$FOM = \frac{P_s}{P_o} = \frac{1}{2} \times \rho \times \sigma \times \eta_A(\mathrm{w}, \mathrm{h}, \lambda_p, \lambda_s) \times \left(\frac{1 - e^{-(\alpha_p + \alpha_s)L}}{\alpha_\mathrm{p} + \alpha_\mathrm{s}} \right) \tag{B.2}$$

We can also define P_{DS} in terms of the quantum efficiency of the detector QE (number of electrons/photon) and CCD sensitivity Ψ (no of electrons/count) and CCD counts per second (C_s/T):

$$P_{DS} = \frac{C_s}{T} \times \frac{hc}{\lambda_S} \times \frac{\Psi}{QE(\lambda_S)} \tag{B.3}$$

Using Eq. (B.1) and (B.3), one gets

$$\begin{aligned} \frac{C_s}{T} &= FOM \times P_o \times \frac{\lambda_S}{hc} \times \frac{QE(\lambda_S)}{\Psi} \times \gamma_{in} \times \gamma_{out} \times T_{MO} \times T_{spec} \\ &= FOM \times C_{ext} \end{aligned} \tag{B.4}$$

For an input pump power of P_o= 0.5 mW, the coupling efficiency γ_{in} = γ_{out} = 0.351, microscope transmission and T_{OM} = 0.65, if we consider e.g. the 1340 cm^{-1} (4-nitrothiophenol dominant mode) line then QE(λ_S)/Ψ = 0.35 counts/photon and T_{spec} = 0.6 (using data supplied by the manufacturer) then C_{exp}= 3.33 $\times 10^{13}$ counts/sec. This factor can be used to convert experimental data to the simulated one (FOM). The quantum efficiency of the CCD using in this thesis is shown in Fig. B.1.

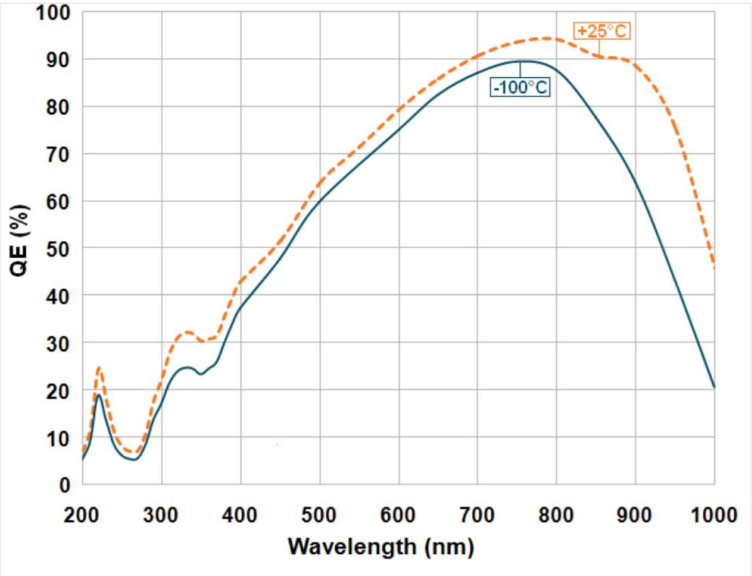

Figure B.1: The Quantum efficiency (QE) of the CCD camera installed on the confocal Raman system used in this work.(Copied from Andor documentation)

Also, for the sake of information to readers, the dark counts of the CCD are also shown in Fig. B.2.

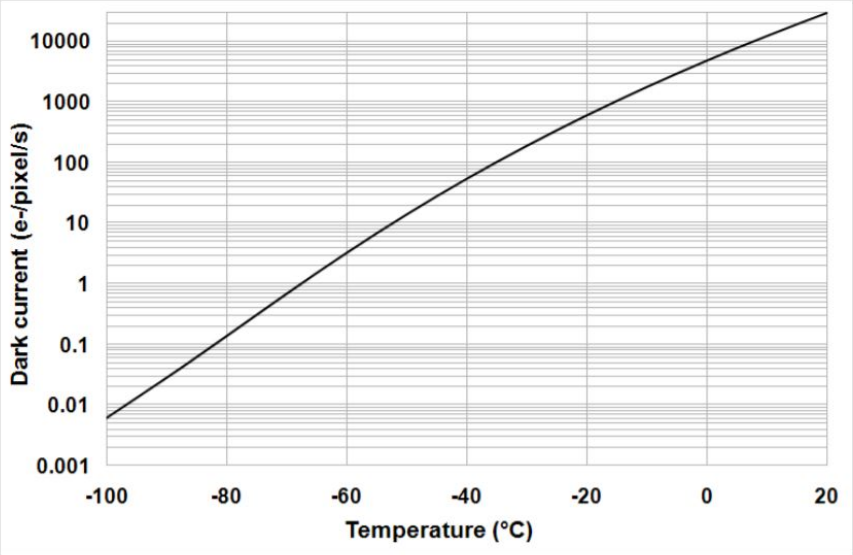

Figure B.2: The dark counts of CCD as the function of temperature.(Copied from Andor documentation)

C

Characterization of plasmonic waveguide loss

C.1 Plasmonic waveguide loss

The waveguide loss is measured using the cutback method. The cutback method is often used for measuring the total attenuation of optical waveguides. The cutback method involves comparing the optical power transmitted through the waveguide of different lengths.

To measure the waveguide loss of plasmonic waveguide, a chip containing different plasmonic waveguide lengths is fabricated. And power transmission through the plasmonic waveguide of three different lengths i.e. 3, 12.5 and 25 μm is measured using the setup presented in Fig. C.1. A tunable Ti-Sapphire laser is used. An objective (40X/0.6NA) is used to couple the light into the waveguide. The polarization is set such that only the TE mode is excited. The power from the output facet is collected using a lens fiber that is further connected to a power meter.

The transmitted power at pump (λ_p = 785 nm) and Stokes (λ_s = 877 nm) wavelength is shown in Fig. C.2. The plasmonic waveguide loss (for Al_2O_3 thickness $\approx$ 58 nm and gold $\approx$ thickness 14 nm) at λ_p = 785 nm and λ_s = 877 nm is $\alpha_p = 2.4 \pm 0.5$ dB/μm and $\alpha_s = 2.1 \pm 0.5$ dB/μm. Further more, the photonic to plasmonic mode coupling extracted from Fig. C.2 is $\gamma_p = 3.97 \pm 0.35$ dB/facet and $\gamma_s = 5.1 \pm 0.38$ dB/facet.

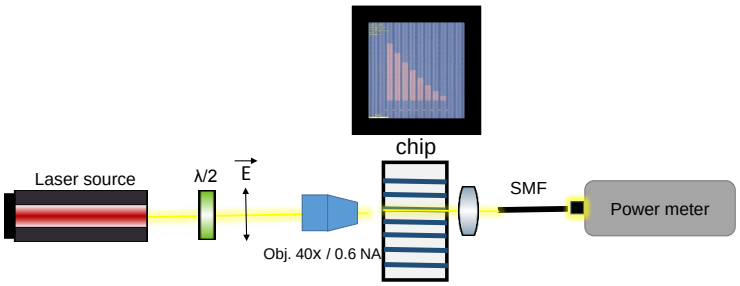

Figure C.1: The schematic of the optical setup used to measure the waveguide losses. Top inset shows the top view of the chip.

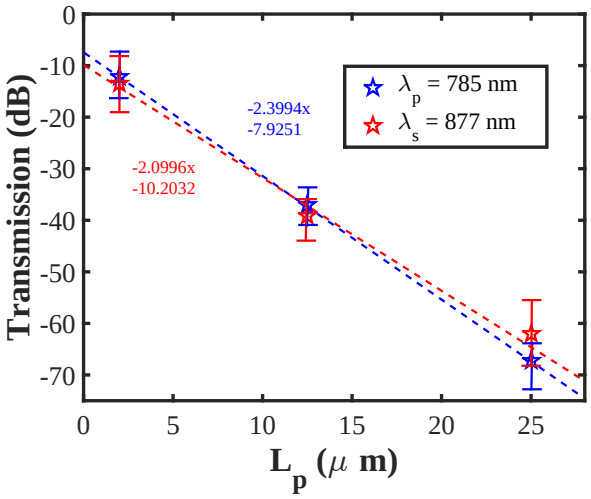

Figure C.2: The transmission measurements for three different lengths of plasmonic waveguide (L_p) at the pump wavelength(λ_p = 785 nm) and the Stokes wavelength (λ_s = 877 nm).

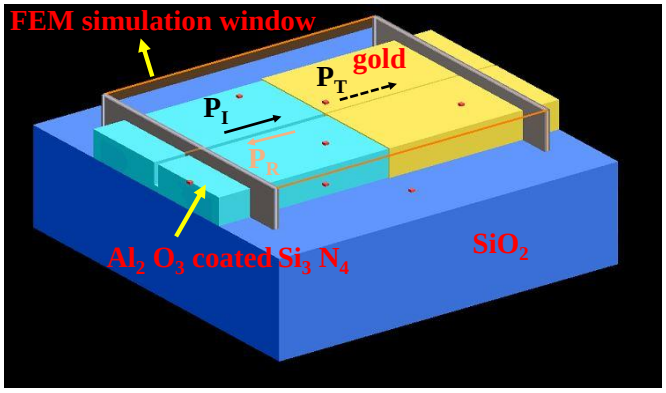

Figure C.3: A 3-D description of a gold slot waveguide connected with ALD Al_2O_3 - PECVD Si_3N_4 slot waveguide. The image is extracted directly from Lumerical EME perspective window.

C.2 Dielectric to metal slot waveguide coupling efficiency

In this section, we analyze the light coupling efficiency from ALD Al_2O_3 coated Si_3N_4 slot waveguide to a gold slot waveguide. Lumerical EME solver is used to calculate the transmission and reflection at the dielectric-metal interface. The schematic of the device is shown in Fig. C.3 (image is extracted directly from the perspective window of Lumerical EME).

For the realization of experimental conditions, we used a refractive index value of 1.9 for the PECVD Si_3N_4 (width = 700 nm and height h = 220 nm), 1.45 for the SiO_2 under cladding and 1 for the top cladding (air). Similarly, the refractive index of 1.6 is assumed for ALD Al_2O_3 Built-in refractive index models for Au (Johnson and Christy29) is used. We used ultra-refined mesh (2 nm). The reflection and transmission are calculated for two different combinations of ALD Al_2O_3 and gold thicknesses in the wavelength range from 700 to 900 nm. For example in one case a thick gold layer (58 nm) and a thin ALD Al_2O_3 layer (12 nm) is assumed. Similarly, in another case a thin gold layer (12 nm) and a thick ALD Al_2O_3 layer (58 nm) is considered. A fundamental TE mode of an arbitrary power P_I is injected into the waveguide from port 1. The transmitted power P_T is then calculated at port 2. Similarly, the reflected power P_R coupled back to the waveguide mode is recorded at port 1. A fixed distance of 900 nm ($\approx$ 1 λ) is considered from the metal-dielectric transition to port 1 and port 2.

For the plasmonic waveguide loss α, the light transmission from dielec-

tric waveguide to metal slot waveguide is calculated using

$$Transmission = 10 \times log_{10}\left(\frac{P_T}{P_I} \times \frac{1}{e^{-\alpha L}}\right) \tag{C.1}$$

Similarly, the reflection is calculated using

$$Reflection = 10 \times log_{10}\left(\frac{P_R}{P_I}\right) \tag{C.2}$$

As shown in Fig. C.4, the device exhibits broadband transmission and reflection. In the case of a thin gold layer (12 nm) and a thick ALD Al_2O_3 layer (58 nm), the transmission reaches to -2.11 dB and -2.49 dB at the pump (785 nm) and Stokes wavelength (877 nm), respectively. The reflection in this case is minimal i.e -38.69 and -38.78 dB at 785 and 877 nm, respectively. On the other hand for the thicker gold layer (58 nm) and thinner ALD Al_2O_3 layer (12 nm). The transmission drops to -12.5 dB and -12.31 dB at 785 and 877 nm, respectively. Also, there is a considerable gain in the reflection i.e. -22.7 dB and -22.61 dB at 785 and 877 nm, respectively.

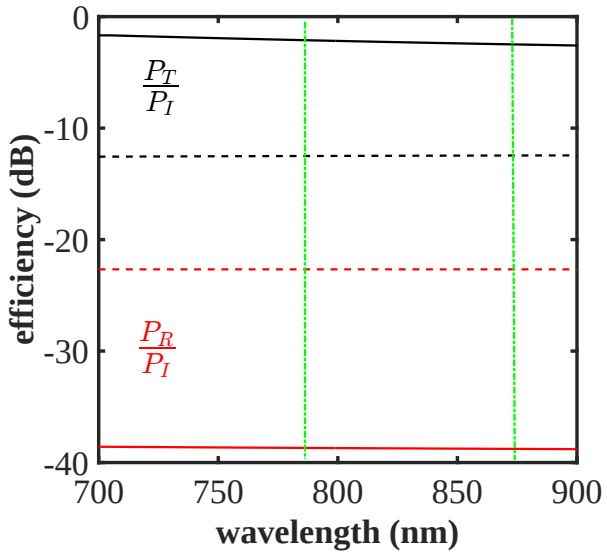

Figure C.4: Transmission (black) and reflection efficiency (red) of an ALD Al_2O_3 coated PECVD Si_3N_4 slot waveguide to a gold waveguide. Transmission and reflection are defined in Eq. (C.1) and (C.2), respectively. The continuous line corresponds to a thin gold layer (12 nm) and a thick ALD Al_2O_3 layer (58 nm). The vertical dashed line corresponds to a thicker gold layer (58 nm) and a thinner ALD Al_2O_3 layer (58 nm). Two vertical dashed lines (green) correspond to pump (785 nm) and Stokes wavelength (877 nm) used in our Raman measurements.